博士論文

High-order semi-Lagrangian type Vlasov solver for ion flow simulation in Hall thrusters

(ホールスラスタにおけるイオン流れの計算のための高次精度セミラグランジュ型ブラソフ解法)

王 哲旭

東京大学大学院工学系研究科

航空宇宙工学専攻

Acknowledgements

I want to express my sincere gratitude to my academic advisor and mentor, Prof. Kimiya Komurasaki, for his guidance in my academic life and kindly support of my life in Japan. Komurasaki sensei has a wide range of knowledge and never hesitate to share his wisdom idea with me. Without his guidance, I can not finish the work successfully.

I would also like to thank Prof. Hiroyuki Koizumi for his valuable suggestions in the Lab seminar. I also want to show my gratitude to assistant Professor Rei Kawashima for his significant advice on numerical simulation.

I want to special thank Prof. Feng Xiao in the Tokyo Institute of Technology for his support during our discussion.

Thank you to my lab members, Sainadh, Florian, Hamada, Bak, and Ito, for the daily talk and suggestions, especially Sainadh shares many ideas that inspired me a lot. Thanks to all the members of the Komurasaki Koizumi laboratory. I really enjoyed a pleasant life in the past five years.

Most importantly, I want to thank my parents for their unconditional reinforcement. Thanks to my girlfriend, Shao, you raise me whenever I fall into a valley during the five years. Previously, I cannot promise anything since I am abroad, but now I will come back, wait for me.

For those who stay with me but leave, thank you for all these years of friendship. *Perhaps we will meet again. Once you have the courage to fly.*

Finally, I want to show my special thanks to the Chinese Scholarship Council. Without financial support from CSC, I cannot finish my dissertation work.

TABLE OF CONTENTS

List of Tables

List of Figures

NOMENCLATURE

B	Magnetic flux density, T
c_s	Ion sound speed, ms^{-1}
f	Plasma distribution function, sm^{-4}
$\tilde{f}$	Non-dimensional valuable
f_i	Ion distribution function, sm^{-4}
f_n	Neutral distribution function, sm^{-4}
g	Gravitational constant, ms^{-2}
$I_{\mathrm{d,i}}$	Time-varying discharge current, A
$\overline{I_\mathrm{d}}$	Time-averaged discharge current, A
I_sp	Specific impulse, s
k_ano	Anomalous transport coefficient
k_B	Boltzmann constant, JK^{-1}
k_ion	Reaction rate coefficient
L	Characteristic scale of acceleration
$\dot{m}$	Anode mass flow rate, kgs^{-1}
n	Number density, m^{-3}
n_e	Electron number density, m^{-3}
n_i	Ion number density, m^{-3}
n_n	Neutral number density, m^{-3}
S_ion	Ionization source term, m^{-4}
T	Thrust, N
T_e	Electron temperature, eV
u	Mean velocity, ms^{-1}
V_d	Discharge Voltage, V
v_de	Azimuthal electron drift velocity, ms^{-1}
ε	Mean energy, J
$D_\perp$	Electron diffusion coefficient, $\mathrm{m}^2\mathrm{V}^{-1}\mathrm{s}^{-1}$
$D_{\perp,\mathrm{cla}}$	Classical diffusion coefficient, $\mathrm{m}^2\mathrm{V}^{-1}\mathrm{s}^{-1}$
$D_{\perp,\mathrm{ano}}$	Anomalous diffusion coefficient, $\mathrm{m}^2\mathrm{V}^{-1}\mathrm{s}^{-1}$
ϕ	Space potential, V
Δ	Oscillation amplitude

η_t	Thruster efficiency
λ_D	Debye length, m

Subscripts

ano	Anomalous electron transport
B	Boltzmann constant
cla	Classical electron transport
d	Discharge
D	Debye length
De	Azimuthal electron drift
e	Electrons
i	Ions
ion	Ionization

LIST OF ABBREVIATIONS

CIP	Constrained interpolation profile
CSL	Conservative semi-Lagrangian
CFL	Courant-Freidrich-Lewy
DG	Discontinuous galerkin
DK	Direct kinetic
EDI	Electron drift instability
FDM	Finite difference method
FFT	Fast Fourier transform
FVM	Finite volume method
HTs	Hall thrusters
MFAM	Magnetic-field-aligned mesh
MUSCL	Monotonic upwind scheme for conservation laws
PDE	Partial differential equation
PIC	Particle-in-cell
PPU	Power processing units
PV	Point value
SL	Semi-Lagrangian
SPT	Stationary plasma thruster
TAL	Thruster with anode layer
TEC	Time-evolution converting
TVD	Total variation diminishing
VIA	Volume integrated average
VP	Vlasov-Poisson
WENO	Weighted essentially non-oscillatory

Chapter 1 Introduction

This dissertation developed a high order Vlasov equation solver and investigated the discharge current oscillation of a thruster with anode layer (TAL). In this chapter, the model of plasma simulation is discussed, following an introduction of the Hall thruster concepts. Then the oscillations in the Hall thruster are discussed. Finally, the objective and outlines of this dissertation are introduced.

1

1.1 General approaches of plasma simulation

During the past decades, researchers developed numerous simulation models to investigate the characteristics of plasma flow. However, since plasma flow is strongly coupled with ions, neutrals, electrons, and electromagnetic fields, it is a challenge for researchers to come up with a well-defined simulation method that may hold a balance between the computational cost and the resolution of the physical phenomenon.

One of the critical parameters in plasma flow is the Knudsen number, which represents the collisions between the particles:

$$Kn = \frac{\lambda}{L}, \tag{1.1}$$

where λ is the mean free path and L is the characteristic physical length of the research object.

To investigate a certain physical problem of plasma mechanics or gas dynamics, the Knudsen number can provide a guidance that whether the kinetic assumption or the continuum fluid assumption should be employed. If $Kn \geq 1$, the particle's mean free path is at the same order as the object's characteristic physical length, the continuum

fluid approach cannot predict the physical phenomenon correctly. In such cases, the kinetic model is more appropriate to the problem compared with fluid description[1].

1.1.1 Kinetic description

The elementary explanation of the plasma mechanics is the kinetic description, a 6-dimensional (3 in space and 3 in velocity) velocity distribution function $f(\mathbf{x}, \mathbf{v}, t)$ is employed to represent the time evolution of each species in plasma.

A kinetic description can be achieved by solving the Boltzmann equation:

$$\frac{\partial f}{\partial t} + \mathbf{v}\frac{\partial f}{\partial \mathbf{x}} + \mathbf{a}\frac{\partial f}{\partial \mathbf{v}} = \left(\frac{\partial f}{\partial t}\right)_{\text{coll}}, \tag{1.2}$$

where f represents the velocity distribution function, $\boldsymbol{v}$ stands the velocity, $\boldsymbol{a}$ is the acceleration of the particles and right hand side $\left(\frac{\partial f}{\partial t}\right)_{\text{coll}}$ demonstrates the collision term. If the species in the plasma can be treated as collisionless, where only the long-range aggregated interactions is considered (right hand side $\left(\frac{\partial f}{\partial t}\right)_{\text{coll}} = 0$), Equation (1.2) becomes the Vlasov equation.

1.1.2 Fluid description

To simplify the description for the plasma flow, the fluid model characterizes the physical phenomenon based on macroscopic quantities including density, velocity, and energy, by taking the velocity moments of the velocity distribution function, the macroscopic quantities can be expressed as:

$$n(\mathbf{x}, t) = \int_{-\infty}^{+\infty} f(\mathbf{x}, \mathbf{v}, t)\, d\mathbf{v}, \tag{1.3}$$

$$u(\mathbf{x},t) = n^{-1}\int_{-\infty}^{+\infty}\mathbf{v}f(\mathbf{x},\mathbf{v},t)\,d\mathbf{v}\,, \tag{1.4}$$

$$\varepsilon(\mathbf{x},t) = n^{-1}\int_{-\infty}^{+\infty}\frac{1}{2}m\mathbf{v}^{\mathbf{2}}f(\mathbf{x},\mathbf{v},t)\,d\mathbf{v}\,, \tag{1.5}$$

where n is the number density, u is the mean velocity and ε is the mean energy.

Integrating the moments of velocity of Vlasov equation and assuming the Maxwellian distribution for plasma distribution function, the conservation equations for the macroscopic quantities are:

Mass conservation:

$$\frac{\partial n}{\partial t} + \boldsymbol{\nabla}(n\mathbf{u}) = 0, \tag{1.6}$$

Moment conservation:

$$mn\left[\frac{\partial \mathbf{u}}{\partial t} + (\mathbf{u}\cdot\boldsymbol{\nabla})\mathbf{u}\right] + \boldsymbol{\nabla}p - qn(\mathbf{E}+\mathbf{u}\times\mathbf{B}) = 0, \tag{1.7}$$

Energy conservation:

$$\frac{\partial}{\partial t}\left(\frac{3}{2}p\right) + \boldsymbol{\nabla}\cdot\left(\frac{3}{2}p\mathbf{u}+\mathbf{q}\right) + p\boldsymbol{\nabla}\cdot\mathbf{u} = 0, \tag{1.8}$$

where p is the pressure term and $\mathbf{q}$ is the heat flux.

1.1.3 Hybrid description

The hybrid description employs both fluid and kinetic models based on their physical characteristics. Some components of the system can be treated as fluid ($Kn \ll 1$) and others kinetically.

1.2 Hall thruster concepts

Hall thrusters (HTs) are the electric propulsion device characterized by an annular acceleration channel with a radial magnetic field. The radial magnetic field captures the electrons at a desired location (perk magnetic flux density location), generating the Hall drift in the azimuthal ($\mathbf{E} \times \mathbf{B}$) direction and leading to a concentrated ionization zone[2]. Propellants (Xenon or Krypton) are jet into the channel through the holes on the anode and ionized in the ionization region.

Generally, HTs operates in the low electron temperature regime of $O(10)$ eV, which refer to the partially ionized plasmas. With the increase of discharge voltage, the electron temperature may reach to 60 eV[3]. And of HTs' plasma density ranges from $10^{16} - 10^{18}$ m^{-3}, referring to an approximate Knudsen number from 0.1 to 10. In that case, the plasma inside the HTs may not be treated as full continuous fluid. Figure 1.1 gives the HTs' plasma parameters' range.

HTs can be classified into two kinds, the stationary plasma thruster (SPT[4]) employs a relatively longer channel and has ceramic channel walls, meanwhile the thruster with anode layer (TAL[5]) claims for a shorter channel with metallic walls. In HTs, the energy loss is mainly caused by the plasma-wall interaction. Owning to the metallic channel walls, the electron energy loss to the wall inside TAL can be minimized, and with a shorter channel length, the energy loss caused by the ions-wall interaction can also be reduced because of the short acceleration region. The total energy losses are very small inside the TAL[7], which lead to a higher efficiency than SPT. Figure 1.2 shows the schematic of SPT (left) and TAL (right).

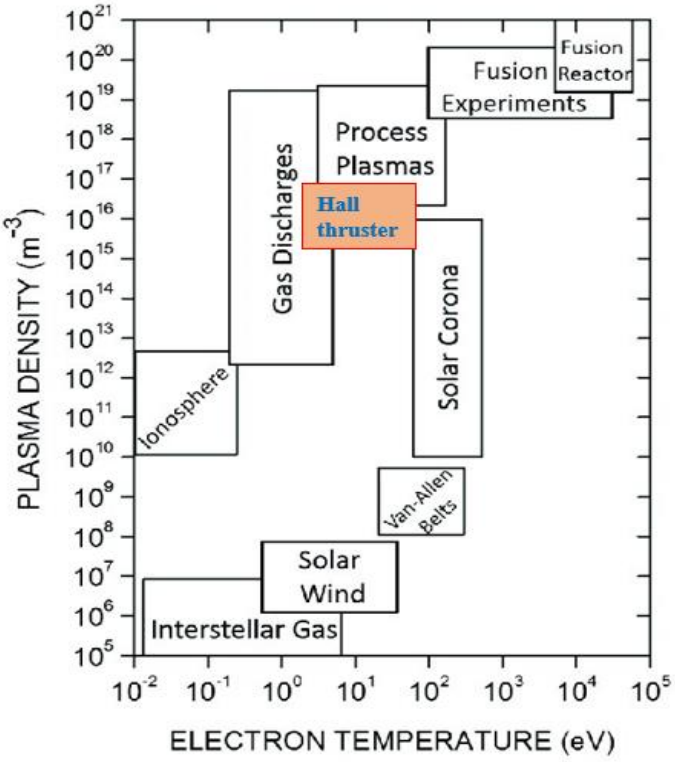

Figure 1.1 Hall thrusters' plasma parameter range.

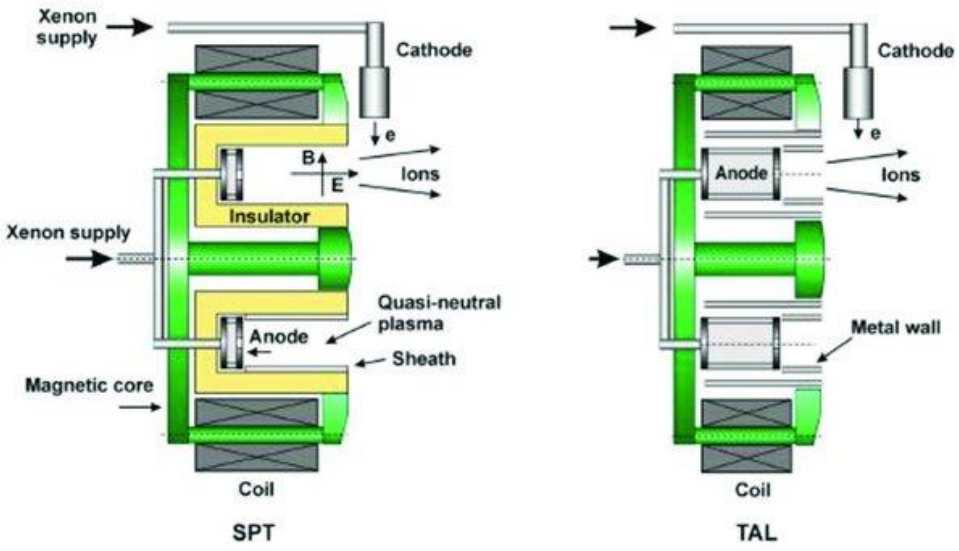

Figure 1.2 Schematic of SPT (left) and TAL (right)[6].

1.3 Oscillations in Hall thruster's plasma

Although HTs operate in the low plasma temperature regime, the ion and electron currents oscillate in a very broad frequency spectrum range from 10 kHz to 1 GHz spontaneously. Figure 1.3 shows the magnitude ordering of relevant frequencies[8].

The ionization oscillations (also being called the breathing mode) are always observed in the frequency band of 10 kHz. Such low frequency oscillations lead to a big fluctuation in discharge current, which yields the largest oscillation amplitude among oscillations occurred in HTs[9][10]. The trend of discharge current amplitude will affect the weight of power processing units (PPU). The azimuthal rotating spoke holds the same frequency with the ionization oscillation[11][12], which has an impact on electron transportation.

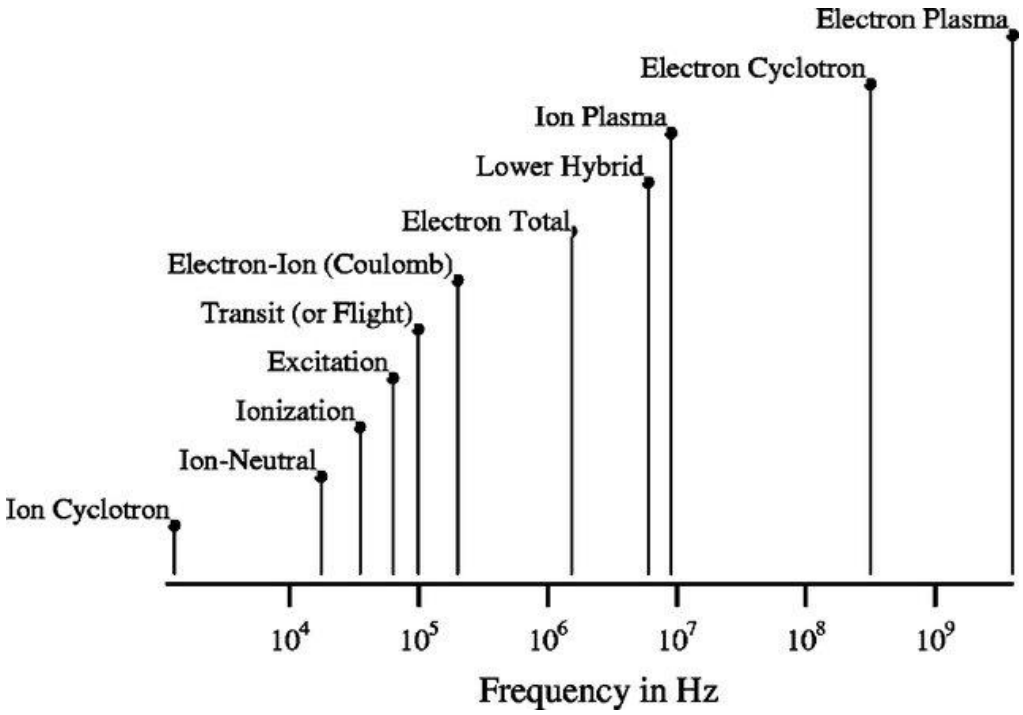

Figure 1.3 Spectra bands of relevant frequencies[8].

The transient-time oscillations are in the frequency band of $70 - 500$ kHz, which was first presented by Esipchuck[13]. This oscillation yields a frequency that compare to the scale of u_i/L, where L is the characteristic scale of acceleration. Here the transient-time oscillations have a great effect on the plasma turbulent conductivity inside HTs[14].

The oscillation band of $2-5$ MHz is related to the electron oscillation scale. These types of oscillations were called the low-frequency electron drift instability (EDI), which were generated in the $\mathbf{E}\times\mathbf{B}$ direction. One mode of the oscillations has been first presented theoretically[15] before the observation by experiment.

The high frequency EDI ($10-100$ MHz), were drawing significant attention in the recent research of HTs[16][17], it had a strong evidence that the EDI has an influence on the anomalous electron transport. Several electron anomalous collision frequencies associated to each of the different mechanisms are shown in Table 1.1.

Table 1.1 Mechanisms for electron anomalous collision frequencies.

Mechanisms	$\nu_{\mathrm{e,ano}}$	Reference
Near wall conductivity	$\beta_{\mathrm{w}}c_{\mathrm{s}}$	Barral[18]
Bohm diffusion	$k_{\mathrm{ano}}\omega_{\mathrm{e}}$	Fife[19]
Shear-turbulence interaction	$k_{\mathrm{ano}}\omega_{\mathrm{e}}\dfrac{1}{1+(A\nabla v_{\mathrm{de}})^{B}}$	Scharfe[20]
Microscales of turbulence	$k_{\mathrm{ano}}\omega_{\mathrm{e}}\left(\dfrac{v_{\mathrm{de}}}{c_{\mathrm{s}}}\right)^{2}$	Cappelli[21]
Turbulence-wave interaction	$k_{\mathrm{ano}}\dfrac{\lvert\nabla\cdot(\mathbf{u}_{\mathrm{i}}n_{\mathrm{e}}T_{\mathrm{e}})\rvert}{m_{\mathrm{e}}n_{\mathrm{e}}c_{\mathrm{s}}v_{\mathrm{de}}}$	Lafleur[22][23][24]

1.4 Numerical methods proposed for Hall thruster simulation

To study the Plasma characteristics of HTs, it claims a high-resolution computational model that may predict the real physic in a broad frequency spectrum. There are three models which have been employed by the researchers: full kinetic, full fluid and hybrid models.

A continuum fluid model cannot describe the correct physical phenomenon for the

species with high Knudsen number ($Kn > 1$) inside the plasma. However, fluid models can still yield useful numerical results if there are enough collisions between the particles ($Kn \ll 1$). Solving ions' plasma behaviors are the most critical goal in HTs simulation since the heavy ions provides most of the thrust[25]. Among the majority simulation cases of HTs, the ion and neutral with large Knudsen number are calculated kinetically, and the magnetized electrons with small Knudsen number is treated as fluid, which lead to a hybrid model that will be explained in the later of this section.

1.4.1 Particle-in-cell (PIC) method

PIC methods are commonly used numerical simulation tools for kinetic plasma modelling. It employs the macroparticle to represent several amount of real particles, tracing each macroparticle under the Lagrangian framework. The equations of macroparticle motion follow Newton's second law:

$$\frac{d\mathbf{x}_\alpha}{dt} = \mathbf{v}, \frac{d\mathbf{v}_\alpha}{dt} = \mathbf{a}_\alpha, \tag{1.9}$$

where α is the species of tracing macroparticle, **v** is the macroparticle's speed and **a** is the acceleration of the macroparticle. A second-order leap-frog method has been commonly used for numerically integration, and a piecewise linear function is used for weighting between the particle positions and grid points.

1.4.1.1 Statistical noise in PIC method

In plasma simulation, the full PIC method traces all the species (including ions, electrons, and neutrals) as macroparticles. It can predict most of the physical phenomena. One of the demerits of this approach is the enormous computational cost due to the macroparticles need to be propagated in the electron motion time scale. Another disadvantage is the statistic noise (also called the discreate particle noise) caused by the finite number of macroparticles.

In one timestep, the PIC method can be divided into two simulation procedures: first, calculate the fields base on the simulated plasma velocity distribution function; second, update each macroparticle's trajectory in the fields. The noise is generated in the first calculation procedure when the plasma velocity distribution function is solved with a small number of macroparticles (In an electron temperature gradient simulation, $N\sim10^8$ vs $N\sim10^{20}$ in experiment). Figure 1.4 shows the convergence study of electron thermal diffusivity in electron temperature gradient simulation[26], the statical noise cause the physical distortion in the simulation results. Since each macroparticle contains the information of plasma velocity distribution function, finding the moments of the distribution function becomes equivalent with finding the solution of integrals in a large phase using the Monte-Carlo techniques[27].

The statistical noise exist in the PIC simulation leads to a difficulty in distinguishing the physical oscillations and numerical noises. Since the PIC method needs to maintain a minimum number of macroparticles inside one cell for the computation, it cannot resolute the correct distribution function when the number density becomes extremely small in some cells. The particle splitting method[28][29][30], which control the number of local macroparticles may keep the PIC simulation running with correct physical description, but this technique also increase the computational cost and the complexity of algorithms.

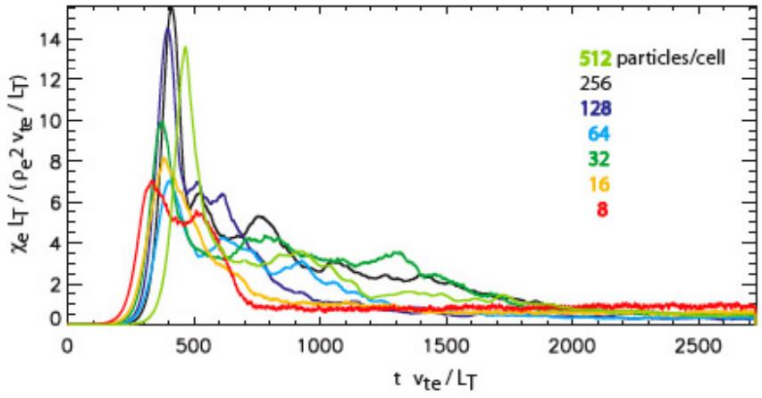

Figure 1.4 Convergence study of electron thermal diffusivity in electron temperature gradient simulation, full PIC method[26].

1.4.1.2 Pioneer works of HTs simulation by using full PIC method

Contemporary works of HTs employing the full PIC method are conducted by many researchers. Szabo[31] developed a two-dimensional full PIC model to analysis a TAL thruster, since all the species needs to calculate on the electron motion time scale, Szabo increased the electron-ion mass ratio and the permittivity in space to accelerate the computational speed. The latter research which had been conducted by Blateau[32] and Irishkov[33] using the same approach to investigate the internal physical effects of SPTs. Cho[34] employed the semi-implicit method together with the artificial mass ratio model to investigate the discharge oscillation and wall erosion effect of UT-SPT-62. Lafleur[22][23] calculated the EDI by using a 1D-azimuthal PIC model and analyzed the electron anomalous collision frequency.

1.4.2 Eulerian framework Vlasov equation solver for kinetic problem

The grid-based Eulerian framework Vlasov equation (Equation 1.2 without source term) solver can be an alternative way to solve the kinetic plasma problem rather than the PIC method. Since the Vlasov equation solver calculates plasma velocity distribution function on the grid, the statistical noise caused by the PIC method can be eliminated through the interpolation procedure. As a result, the design order of accuracy can be achieved globally on all the grid point. However, the Vlasov equation solver requires a large storage of the multi-dimension problems (3D in space and 3D in velocities), and the numerical diffusion exists during the simulation procedure.

1.4.3 Hybrid model

Most of the numerical studies of HTs simulate the SPT type configuration. The plasma behaviors indicate that the electrons can be described as the continuum fluid, meanwhile ions and neutrals are calculated kinetically.

One of the pioneering works conducted by Komurasaki[36] employed the flux tube ion model and electron fluid model in two dimensions. The thrust performance and ion loss to the wall were investigated. A self-consistent PIC model for ions and quasi one-dimensional electron fluid model were used by Fife[19] to describe the plasma-wall interaction. Kawashima[37][38] developed the hyperbolic equation system for the electron fluid model by adding the pseudo-time term to the elliptical equation set. The hybrid PIC method with hyperbolic electron fluid solver successfully predicted the rotating spoke in HTs.

Boeuf[39] investigated the ionization oscillation by using a 1D quasi-neutral hybrid Vlasov-fluid model. The ions were simulated through the Vlasov equation and neutrals were solved through a continuity equation with constant flow speed. The Vlasov equation was solved by a second-order upwind scheme, and he insisted that ' the ion distribution in velocity space shows some obvious numerical diffusion effects when the upwind scheme is used. ' Morozov[40] developed another 1D hybrid Vlasov fluid code for transient 1D analysis, the ionization oscillation and ion’s distribution function were studied. Hara[41] reproduced the ionization oscillation and transient-time oscillation by developed the hybrid direct kinetic (DK) method, the Vlasov equation for ions and neutrals are solved through a finite volume method (FVM) with Monotonic Upwind Scheme for Conservation Laws (MUSCL) scheme[42].

1.4.4 Full Fluid model

In the plasma simulation, if the Knudsen number is small enough or the kinetic effect is not the main reason of the interested physical phenomenon, the full fluid model can be applied to simulate ions, neutrals, and electrons. The fundamental equation set contains several partial differential equations (PDEs) which describe the conservation of mass (Equation 1.6), momentum (Equation 1.7) and energy (Equation 1.8) with some additional equations to make the whole set self-consistent.

A two-dimensional full fluid simulation model (Hall2De) for HTs has been developed by Mikellides[43][44], it employed a two-dimensional magnetic-field-aligned mesh (MFAM) to get rid of unexpected sharp gradients that may not align with the calculation grid. Hall2De holds several merits over the hybrid-PIC method. It can extend the calculation domain widely in the plume region outside the thruster channel, and a noiseless result can be achieved compared with the statistical fluctuations inherent in PIC simulation.

1.5 Comparison with previous work

Table 1.2 Comparison with Direct Kinetic model[41].

	DK model	SL model
Numerical scheme	Second-order FVM	Fourth order SL method
Specification	Eulerian	Eulerian-Lagrangian
Reconstruction method	Arora-Roe scheme	Fourth-order WENO scheme
Stability	Conditionally stable	Unconditionally stable
Conservative	Mass conservative	Mass conservative

Table 1.2 shows the previous work conducted by Dr. Hara[41] which employed the same approach of Vlasov equation solver to solve the ion flow in HTs. The DK model was developed by FVM and the second-order Arora-Roe scheme was used for the flux

reconstruction. The Vlasov equation solver employed in this work was developed by the SL method with fourth-order WENO scheme. The SL method shows less dispersion error than the FVM, according to the stability analysis[45], SL method is unconditionally stable and FVM is conditionally stable.

Figure 1.5 gives the results of strong nonlinear Landau damping generated by the second-order DK model and fourth-order SL model, as shown in the figure, the fourth-order SL model captured the small energy tail better than the second-order DK model, and fourth-order SL model successfully captured the damping and growth rate of the electron energy, on the other hand it's hard to justify the growth rate from the results generated by second-order DK model. The fourth-order SL model shows a higher resolution than the second-order DK model.

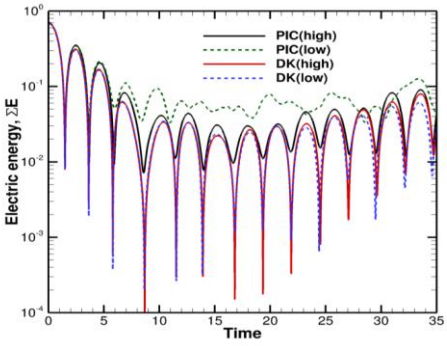

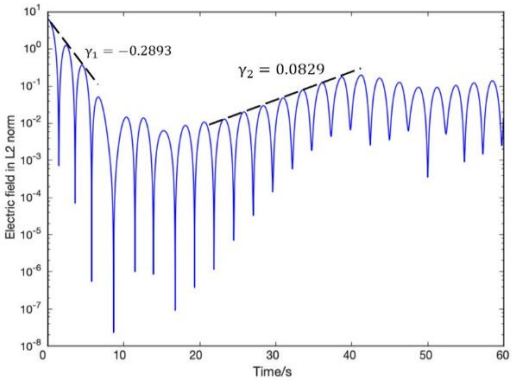

Second-order FVM[41] Fourth-order SL method

Figure 1.5 The simulation results of strong nonlinear Landau damping.

1.6 Objective and outlines of this dissertation

The objective of this dissertation is to develop a high resolution Vlasov equation solver that may replace the PIC method in the hybrid code. The following improvements are challenged:

1. **High spatial Accuracy**: Fourth-order accuracy in space is achieved by employing the fourth-order Vlasov equation solver.
2. **Free from statistical noise**: The Vlasov equation solver yields a smooth result which is free from statistical noise, and the numerical diffusion is small compared

with low order solver.

3. **Applicability to high dynamic density variation**: The Vlasov equation solver shows the applicability to the kinetic problems especially in the low number density regime.

Following the improvements, a constrained interpolation profile conservative semi-Lagrangian (CIPCSL3) scheme is applied to solve the Vlasov equation. To keep the high spatial accuracy, a fourth order weighted essentially non-oscillatory (WENO) limiter has been employed.

This dissertation contains five chapters. In chapter 2 the pioneer work of Vlasov solver and the numerical methods employed in this study are introduced.

In chapter 3, the verification of CIPCSL3 method and the applications to the Vlasov-Poisson equation system are presented. The numerical features of fourth-order WENO limiter and second-order TVDCW limiter are investigated through all the test cases. Finally, the numerical results of two stream instability calculated by fourth-order CIPCSL3 Vlasov solver and full PIC solver are compared.

In chapter 4, the one-dimensional hybrid ion-Vlasov and electron-fluid model of ionization oscillation simulation in Hall thruster is presented., the hybrid PIC solver solves the same case as a reference. The numerical results are compared between the two solvers.

Finally in chapter 5, the conclusions of this dissertation are summarized. The future improvements for this study are presented as the future work.

Chapter 2 Implementations of the high-resolution Vlasov equation solver

In this chapter, the pioneer works and the numerical methods of Vlasov equation solver are introduced and the originality of this work is shown at the end.

2.1 Upwind scheme

The upwind scheme is a numerical method which design to solve the hyperbolic PDEs, to introduce the scheme, following one-dimensional linear advection equation is investigated:

$$\frac{\partial f}{\partial t} + u\frac{\partial f}{\partial x} = 0, \tag{2.1}$$

where u is the velocity and $f(x,t)$ is the physical valuable. A straightforward first upwind discretization of Equation (2.1) reads:

$$\begin{aligned} &\frac{f_i^{n+1} - f_i^n}{\Delta t} + u\frac{f_i^n - f_{i-1}^n}{\Delta t} = 0 \quad if\ u > 0 \\ &\frac{f_i^{n+1} - f_i^n}{\Delta t} + u\frac{f_{i+1}^n - f_i^n}{\Delta t} = 0 \quad if\ u < 0, \end{aligned} \tag{2.2}$$

the upwind scheme discretizes PDEs with more points in the upwind side (based on the velocity direction). A series of numerical methods [46][47][48] have been developed under the upwind framework to solve hyperbolic PDEs problems.

2.2 Pioneer works of semi Lagrangian Vlasov equation solver

The semi-Lagrangian (SL) method is a numerical solution technique for solving the linear PDE (Equation 2.1) that represents the advection process. it was first presented by Wiin-Nielsen[49], this upwind method solves the Lagrangian parcels under a Eulerian

framework. It keeps the advantage of stability and avoids the disadvantage of statistical noise caused by the Lagrangian type numerical method. The scheme is also unconditionally stable and reveals little numerical dispersion.

In 1976, Cheng[50] first applied SL method to solve the Vlasov-Poisson (VP) equation system by using cubic-splines and time vector splitting. Sonnendrücker[51] developed the SL method with cubic-splines and without time splitting for VP system. Nakamura[52] replace the polynomial with Hermite interpolation and transport the gradients information of the distribution function to keep the high-resolution feature. To maintain the mass conservation in SL method, Qiu presented the conservative WENO[53] reconstruction. In the recently year, many high order SL schemes, based on finite difference method (FDM), finite volume method (FVM) and discontinuous Galerkin method (DG), have been developed to simulate the Vlasov equation[55][56][57].

Notwithstanding that several schemes with high spatial accuracy have been successfully developed for the VP system, no such research had been done for the HTs simulation by using a high-order Vlasov equation solver with electron fluid model. One of the challenges is that the ghost cell boundary condition for high order scheme is difficult to implement to keep the high-order feature near the boundary. The number of the ghost cells needs to satisfy the order of the scheme, and it needs to avoid the unphysical numerical oscillation enter the simulation domain. For a smooth wave form, the Lagrange polynomial can be used to extrapolate the values in the ghost cells, otherwise, numerical techniques (such as buffer zone boundary condition, WENO extrapolation or perfectly matched layer boundary condition) need to be applied to the ghost cell to eliminate the numerical oscillations outside the calculation domain.

2.3Semi-Lagrangian method of linear advection equation

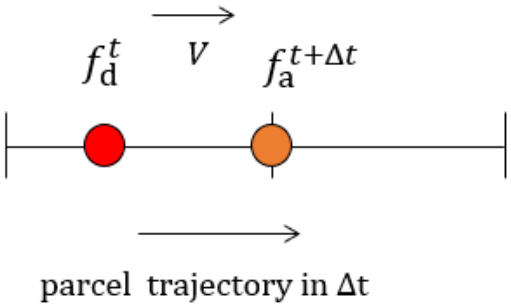

Figure 2.1 Schematic of the backward semi-Lagrangian procedure.

Considering the linear PDE as Equation (2.1), The SL method usually employs the Lagrangian invariant at time t:

$$f(x,t) = f(\hat{x}, t-\Delta t), \tag{2.3}$$

where $\hat{x}$ is the departure point of the physical valuable $f(x,t)$ at the time level of $t-\Delta t$. The invariant valuable arrives at x after Δt. Figure 2.1 shows the schematic of SL procedure, the subscripts d stands for departure point and a stands for the arrival point. Since the departure point $\hat{x}$ is not on the grid, two steps need to be done for the SL method to find the solution[54]:

1. Calculate the trajectory of all the parcels on the grid.
2. Construct an interpolation polynomial for $f(\hat{x}, t-\Delta t)$ that contains the departure point of the trajectory.

2.3.1 Conservative numerical schemes for SL method

The semi Lagrangian method solving the Lagrangian parcel under Eulerian framework, it shows less dissipation and unconditional stable with large calculation time step. Since the SL method is developed to solve the pure linear advection equation, it does not guarantee the mass conservation law[59], this will affect the long-term

simulation's results. Several numerical schemes [50] [58][60] developed for SL method in the early year still show the demerit of mass nonconservative.

Recently, many researchers present the conservative form SL method by following the conservation law. Qiu[55] solved the conservation form equations by FDM with several high order WENO interpolations; Bonaventura[59] developed a conservative flux form SL method for the diffusion equations; Heath[56] demonstrated a DG method with upwinding for solving the VP equation system and Xiao[54] presented a compact CIP scheme with conservative relation to maintain the mass conservation.

2.3.2 CIP method Families

The Cubic-Interpolated Propagation (CIP) method was first presented by Yabe for solving hyperbolic equations[60][61], the CIP scheme propagated both point value and first derivative to maintain the correct waveform inside one cell Figure 2.2 compared the phase error of several schemes and demonstrated that 'the CIP method reproduce the correct phase speed even up to $k\Delta x = \pi$, which means that it can reproduce the wavelength by three points.'[62] Owing to the compact feature of this method, it can keep the high order accuracy by only employing one ghost cell at the boundary. Nakamura[52] developed the existed scheme to solve the multi-dimensional VP system, an exactly conservative SL framework multi-dimensional hyperbolic equations solver had also been developed with the same author[63]. A series of CIP schemes had been modified to make nonconservative semi-Lagrangian schemes be exactly conservative and change the name of the schemes to Constrained Interpolation Profiles (CIP) method[65]. Xiao[54] developed the Constrained Interpolation Profiles Conservative Semi-Lagrangian method with a third-order reconstruction polynomial inside the cell (CIPCSL3), and applied it to solve several physical problems[66][67]. Based on Xiao's work, Sun[68] presented a fourth-order scheme which employed the fourth-order WENO limiter under the multi-moment FVM framework.

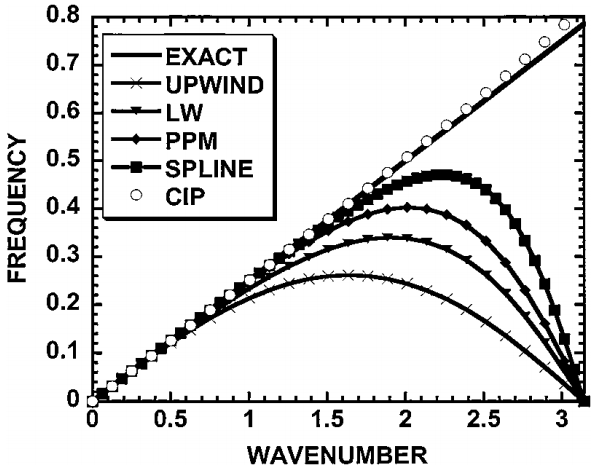

Figure 2.2 Phase error of various schemes[62].

2.3.3 High order CIPCSL3 approach

2.3.3.1CIPCSL3 framework

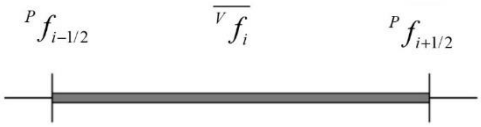

Figure 2.3 Schematic of Point Value (PV) and Volume Integrated Average (VIA) value.

To construct the interpolation polynomial inside the cell, a third-order Hermite interpolation function reads:

$$f(x) = f\left(x_{i-1/2}\right) + c_{1i}\left(x - x_{i-1/2}\right) + c_{2i}\left(x - x_{i-1/2}\right)^2 + c_{3i}\left(x - x_{i-1/2}\right)^3. \quad (2.4)$$

Figure 2.3 gives the schematic of each valuable inside a single one-dimensional cell. The point value (PV) is defined at the cell boundary and the Volume Integrated Average (VIA) value is determined at the cell center. At two boundaries of the cell, we have:

$$f\left(x_{i-1/2}\right) = {}^{P}f_{i-1/2} \quad , \tag{2.5}$$

and

$$f\left(x_{i+1/2}\right) = f\left(x_{i-1/2}\right) + c_{1i}\Delta x + c_{2i}\Delta x^2 + c_{3i}\Delta x^3 = {}^{P}f_{i+1/2} \quad , \tag{2.6}$$

the VIA in the middle of the cell is imposed as:

$$\frac{1}{\Delta x}\int_{i-1/2}^{i+1/2} f(x)\,dx = f\left(x_{i-1/2}\right) + \left(\frac{1}{2}\right)c_{1i}\Delta x + \left(\frac{1}{3}\right)c_{2i}\Delta x^2 + \left(\frac{1}{4}\right)c_{3i}\Delta x^3 = \overline{{}^{V}f_i}, \tag{2.7}$$

finally, the first derivative defined in the middle point of the cell reads:

$$\left.\frac{df(x)}{dx}\right|_{x=x_i} = c_{1i} + c_{2i}\Delta x + \frac{3}{4}c_{3i}\Delta x^2 = d_i. \tag{2.8}$$

Each coefficient of Equation (2.6) can be expressed by the point value ${}^{P}f$ defined at each boundary, VIA $\overline{{}^{V}f_{\mathrm{i}}}$ described at cell center and first derivative d_i specified at cell center. By employing the upwind-bias at the boundary, the coefficients read:

if $u \geq 0$,

$$\begin{cases} c_{1i}^{L} = -\dfrac{6}{\Delta x^3}\overline{{}^{\mathrm{V}}f_{i-1}^{n}} + \dfrac{6}{\Delta x}{}^{\mathrm{P}}f_{i-1/2}^{n} - 2d_{i-1}^{n} \\ c_{2i}^{L} = -\dfrac{6}{\Delta x^4}\overline{{}^{\mathrm{V}}f_{i-1}^{n}} + \dfrac{3}{\Delta x^2}({}^{3\mathrm{P}}f_{i-1/2}^{n} - {}^{\mathrm{P}}f_{i-3/2}^{n}) - \dfrac{6}{\Delta x}d_{i-1}^{n} \\ c_{3i}^{L} = \dfrac{4}{\Delta x^3}({}^{\mathrm{P}}f_{i-1/2}^{n} - {}^{\mathrm{P}}f_{i-3/2}^{n}) - \dfrac{4}{\Delta x^2}d_{i-1}^{n} \end{cases} , \tag{2.9}$$

if $u < 0$,

$$\begin{cases} c_{1i}^{R} = \dfrac{6}{\Delta x^{3}} \overline{{}^{\mathrm{V}} f_{i}^{n}} - \dfrac{6}{\Delta x} {}^{\mathrm{P}} f_{i-1/2}^{n} - 2d_{i+1}^{n} \\ c_{2i}^{R} = -\dfrac{6}{\Delta x^{4}} \overline{{}^{\mathrm{V}} f_{i}^{n}} + \dfrac{3}{\Delta x^{2}} (3\,{}^{\mathrm{P}} f_{i-1/2}^{n} - {}^{\mathrm{P}} f_{i+1/2}^{n}) + \dfrac{6}{\Delta x} d_{i+1}^{n} \\ c_{3i}^{R} = -\dfrac{4}{\Delta x^{3}} ({}^{\mathrm{P}} f_{i-1/2}^{n} - {}^{\mathrm{P}} f_{i+1/2}^{n}) - \dfrac{4}{\Delta x^{2}} d_{i+1}^{n} \end{cases}, \tag{2.10}$$

once all the coefficients are determined, the solution of the physical valuable f at time level t^{n+1} can be obtained through:

$$f^{n+1} = \begin{cases} f^{L}(x - u\Delta t) & \text{if } u \geq 0 \\ f^{R}(x - u\Delta t) & \text{if } u < 0 \end{cases}. \tag{2.11}$$

Here the superscripts L and R represent the coefficients (Equations 2.9, 2.10) depending on the velocity direction.

To keep the mass conservation, the VIA should be advanced by the conservative relation[64][65]:

$$\overline{{}^{V} f}^{\mathrm{n+1}} = \overline{{}^{V} f}^{\mathrm{n}} - (g_{i+1/2} - g_{i-1/2}), \tag{2.12}$$

where $\mathrm{g}_{i+1/2}$ is the flux of physical valuable that get through the boundary $x = x_{i+1/2}$ during Δt, and it can be estimated by:

$$\begin{aligned} g_{i+1/2} = \int_{t^{n}}^{t^{n+1}} [&\min(0, u)\, f_{i+1/2}^{R}\left(x_{i+1/2} - u(t - t^{n})\right) + \\ &\max(0, u) f_{i+1/2}^{L}\left(x_{i+1/2} - u(t - t^{n})\right)]dt\,, \end{aligned} \tag{2.13}$$

and the velocity u keeps constant during the time interval Δt leads to:

$$\begin{aligned} g_{i+1/2} = &-\min(0, \xi)\left(f_{i+1/2}^{n} + \frac{1}{2} c_{1i}^{R}\xi + \frac{1}{3} c_{2i}^{R}\xi^{2} + \frac{1}{4} c_{3i}^{R}\xi^{3}\right) \\ &-\max(0, \xi)\left(f_{i+\frac{1}{2}}^{n} + \frac{1}{2} c_{1i}^{R}\xi + \frac{1}{3} c_{2i}^{R}\xi^{2} + \frac{1}{4} c_{3i}^{R}\xi^{3}\right), \end{aligned} \tag{2.14}$$

where $\xi = -u\Delta t$.

The first derivative defined at the cell center d_i^n is a free parameter that can be modified to maintain the interpolation polynomial, in order to make the numerical simulation reach some designed properties. In this dissertation, the first derivative has been interpolated by a fourth-order WENO limiter, a second-order TVDCW limiter is also being taken into consideration as a reference.

Full computational procedures within one CIPCSL3 step:

- Construct the interpolation formula
  1. Compute the first derivative d_i^n by any numerical approximation.
  2. Calculate the coefficients of cubic polynomial by Equations (2.9, 2.10).

- Advance the valuable
  1. Compute the SL solution by Equation (2.11).
  2. Update the VIA through Equation (2.12).

Here the calculation procedure in one dimension can be expressed as:

$$\mathrm{CIPCSL1D}\left(\tilde{u}_{ij}, {}^{V}\overline{f}, {}^{V}\overline{f}^{\mathrm{new}}, {}^{P}f, {}^{P}f^{new}\right), \tag{2.15}$$

where ${}^{V}\overline{f}$ and ${}^{P}f$ are the old valuables of VIA and PV in 1D, ${}^{V}\overline{f}^{\mathrm{new}}$ and ${}^{P}f^{new}$ are the updated valuables after the CIPCSL3 procedure.

2.3.3.2 Fourth order WENO limiter

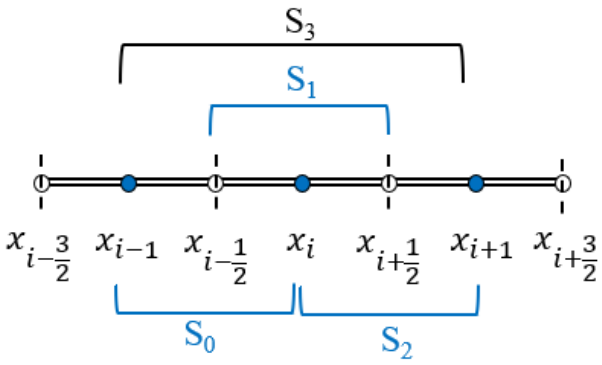

Figure 2.4 Stencils of WENO limiter.

The fourth order WENO limiter[68] is built with the PV and VIA locally getting from the CIPCSL3 scheme.

Here, the PV at cell center can be calculated through:

$$ {}^{P}f_i = \frac{3}{2}\overline{{}^{V}f_i} - \frac{1}{4}\left({}^{P}f_{i-1/2} + {}^{P}f_{i+1/2}\right). \tag{2.16} $$

By employing the PV at the cell center, WENO interpolation sub stencils can be settled as

Figure 2.4. The first derivative can be calculated on each stencil and weighted by the second-order polynomials:

$$ \begin{aligned} q_0^{[1]}(x_i) &= \frac{3\,{}^{P}f_i + {}^{P}f_{i-1} - 4\,{}^{P}f_{i-1/2}}{\Delta x} \\ q_1^{[1]}(x_i) &= \frac{{}^{P}f_{i+1/2} - 4\,{}^{P}f_{i-1/2}}{\Delta x} \\ q_2^{[1]}(x_i) &= \frac{3\,{}^{P}f_i + {}^{P}f_{i+1} - 4\,{}^{P}f_{i+1/2}}{\Delta x}. \end{aligned} \tag{2.17} $$

A fourth-order polynomial inside sub stencil S_3 can be derived to approximate the first derivative with fourth-order spatial accuracy:

$$ Q_i^{[1]}(x_i) = \frac{8\,{}^{P}f_{i+1/2} + {}^{P}f_{i-1} - 8\,{}^{P}f_{i-1/2} - {}^{P}f_{i+1}}{6\Delta x}. \tag{2.18} $$

Equation (2.17) can be reconstructed through the linear combination of second-order

polynomials (Equation 2.16):

$$Q_i^{[1]}(x_i) = \sum_{j=0}^{2} \gamma_j \, q_2^{[1]}(x_i), \tag{2.19}$$

where the linear weights are: $\gamma_0 = \frac{1}{6}, \gamma_1 = \frac{2}{3}, \gamma_2 = \frac{1}{6}$.

The WENO reconstruction substitute the linear weights γ_j with nonlinear weights ω_j, here the smoothness indicator is designed as:

$$\beta_j = \sum_{l=1}^{2} \int_{x_{i-1/8}}^{x_{i+1/8}} \Delta x_i^{2l-1} \left(\frac{\partial q_j(x)}{\partial x^l}\right)^2 dx, \quad j = 0,1,2 \tag{2.20}$$

.

For the computing of WENO nonlinear weights, many researchers followed the classical WENO-JS scheme which presented by Jiang and Shu[70]. By comparing series algorithms of WENO nonlinear weights such as WENO-Z[71] and WENO-M[72] *et al*. Shen[73] analyzed the accuracy loses near the contact discontinuity regime of each scheme. The results proved that WENO-Z provided a reasonable balance between the order of accuracy in space and the algorithmic complexity.

Here, the WENO-Z scheme is applied to the reconstruction of the first derivative by calculating the nonlinear weights with:

$$\omega_j = \frac{\alpha_j}{\sum_{k=0}^{2} \alpha_k}, \quad \alpha_j = \gamma_j \left(1 + \left(\frac{\tau}{\beta_j + \varepsilon}\right)^p\right), \quad j = 0,1,2 \tag{2.21}$$

,

where $\varepsilon = 10^{-40}$ and $\tau = |\beta_2 - \beta_0|$. p controls the weights of the stencils which contain discontinuity, increasing this value will make the solution in smooth region close to the central scheme, but will generate large numerical dissipation near the discontinuities. For the work in this dissertation, $p = 1$ is employed.

The WENO scheme reconstructed the first derivative by:

$$Q_i^{[1]}(x_i) = \sum_{j=0}^{2} \omega_j q_j^{[1]}(x_i) \quad , \tag{2.22}$$

where $\widetilde{Q_i^{[1]}}(x_i)$ is corresponding to d_i^n which has been treated as a free parameter in CIPCSL3 method above Equations (2.9, 2.10).

Although this WENO limiter provides a good spatial accuracy during the simulation, it is not following the rule of positive-persevering. During the simulation of VP equation system which will be introduced in the next chapter, a very small undershooting (negative value of distribution function) with the order of $O(10^{-4})$ in strong nonlinear Landau damping and $O(10^{-10})$ in two stream instability are observed.

2.3.3.3 The TVDCW limiter

To compare with the low order scheme, a second-order limiter which has the same form as Collela and Woodward[74] is employed.

Recalling the PV defined at cell center (Equation 2.15), the first derivative can be calculated through:

$$d_i = \begin{cases} \dfrac{\min\left(\left|{}^{P}f_{i+1} - {}^{P}f_{i-1}\right|, 2\left|{}^{P}f_{i+1} - {}^{P}f_{i}\right|, 2\left|{}^{P}f_{i} - {}^{P}f_{i-1}\right|\right)}{\Delta x} & \text{if } ({}^{P}f_{i+1} - {}^{P}f_{i})({}^{P}f_{i} - {}^{P}f_{i-1}) > 0 \\ 0 & \text{otherwise} \end{cases} . \tag{2.23}$$

This CW reconstruction claims a second-order accuracy in smoothness region, but it creates a plateau in the area where the first derivative changes the sign[54].

2.4 Time discretization for Vlasov equation

The collisionless Boltzmann equation, also known as Vlasov equation reads:

$$\frac{\partial f}{\partial t}+\mathbf{v}\frac{\partial f}{\partial \mathbf{x}}+\mathbf{a}\frac{\partial f}{\partial \mathbf{v}}=0 \quad , \tag{2.24}$$

the nonlinear Vlasov equation can be discretized into several linear advection PDEs by using the second-order Strang time splitting[75] and solving by the CIPCSL3 method:

$$\begin{cases}\dfrac{\partial f}{\partial t}+\mathbf{v}\dfrac{\partial f}{\partial \mathbf{x}}=0\\ \dfrac{\partial f}{\partial t}+\mathbf{a}\dfrac{\partial f}{\partial \mathbf{v}}=0\end{cases} . \tag{2.25}$$

Figure 2.5 gives the schematic of PV VIA and SIA in two-dimensional case. The calculation procedures read:

$$\begin{aligned}&\tilde{u}_{ij}=\left(u_{i-1/2j-1/2}+u_{i-1/2j+1/2}\right)/2\\ \text{Procudure 1:}\quad &CIPCSL1D\left(\tilde{u}_{ij},\ \overline{{}^{V}f},\ \overline{{}^{V}f}^{p1},\ \overline{{}^{S}f}_{Y},\ \overline{{}^{S}f}_{Y}^{p1}\right)\\ &CIPCSL1D\left(u_{i-1/2j-1/2},\ \overline{{}^{S}f}_{X},\ \overline{{}^{S}f}_{X}^{p1},\ {}^{p}f,\ {}^{p}f^{p1}\right)\end{aligned} \tag{2.26}$$

$$\begin{aligned}&\tilde{v}_{ij}=\left(v_{i-1/2j-1/2}+v_{i-1/2j+1/2}\right)/2\\ \text{Procudure 2:}\quad &\mathrm{CIPCSL1D}\left(\tilde{v}_{ij},\ \overline{{}^{V}f}^{p1},\ \overline{{}^{V}f}^{\mathrm{p2}},\ \overline{{}^{S}f}_{X}^{p1},\ \overline{{}^{S}f}_{X}^{\mathrm{p2}}\right)\\ &\mathrm{CIPCSL1D}\left(v_{i-1/2j-1/2},\ \overline{{}^{S}f}_{Y}^{p1},\ \overline{{}^{S}f}_{Y}^{\mathrm{p2}},\ {}^{p}f^{p1},\ {}^{p}f^{\mathrm{p2}}\right),\end{aligned} \tag{2.27}$$

where $\tilde{u}_{ij},\tilde{v}_{ij}$ are the averaged velocity in each direction, $u_{i-1/2j-1/2},v_{i-1/2j-1/2}$ are the velocity in each direction defined at cell boundary, $\overline{{}^{V}f}$ is the VIA defined at cell center, $\overline{{}^{S}f}$ is the SIA defined at the center of each boundary and ${}^{P}f$ is the PV defined at the boundary, the superscript $p1$ and $p2$ stand for the new valuables which are updated during produce 1 and produce 2, the subscript X and Y represent the valuables in x direction and y direction.

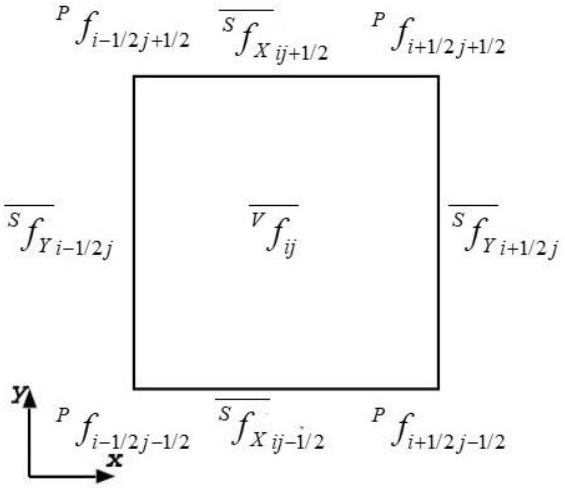

Figure 2.5 The schematic of Point Value (PV) defined at boundary, Surface Integrated Average (SIA)defined at surface and Volume Integrated Average (VIA) in two-dimensional case.

For the VP equation system, the velocity space becomes y direction, and the velocity in y direction stands for the acceleration. the calculation following:

Step1: Doing procedure 1 in x direction for $1/2\Delta t$.

Step 2: Update electric field E.

Step 3: Doing procedure 2 in velocity direction (y direction) for Δt.

Step 4: Repeat step 1.

Since the departure point problem of the SL method can be solved through an ordinary differential equation:

$$\begin{cases} \dfrac{dX}{dt} = -a(X,t) \\ X(t_0 = t^n) = X_0 = x_{i+1/2} \end{cases}, \tag{2.28}$$

a third-order Runge-Kutta method is employed for each CIPCSL3 procedure:

$$\begin{cases} X_0 = x_{i+1/2} \\ X_1 = X_0 - u(X_0, t_0)\Delta t \\ X_2 = \frac{3}{4}X_0 + \frac{1}{4}X_1 - \frac{1}{4}u(X_1, t_1)\Delta t \\ X_3 = \frac{1}{3}X_0 + \frac{2}{3}X_2 - \frac{2}{3}u(X_2, t_2)\Delta t \end{cases}. \quad (2.29)$$

2.5 Summary of this chapter

This chapter introduces the pioneer work of the Vlasov equation solver and the CIP methods family. The Vlasov equation solver developed in this dissertation is based on the CIPCSL3 method, by applying the fourth-order WENO limiter to the first derivative, the important findings are:

1. The CIPCSL3 framework shows a high-resolution feature on the coarse mesh due to the characteristic of compact scheme. It maintains the mass conservation by employing a flux type conservation equation (Equation 2.12). The first derivative is a free parameter which can be modified to design the ideal computational method.

2. By applying the fourth-order WENO limiter to the CIPCSL3 reconstruction procedure, the stability and accuracy can be guaranteed, the WENO limiter also generate in a compact form which employs the PV defined at cell center.

3. For CIPCSL3 method, more storages are needed because it propagates the VIA together with PV, which is a demerit when calculating the multi-dimension problem.

The originality of this dissertation is to develop a high resolution noiseless Vlasov equation solver for the HTs simulation, the CIPCSL3 method with fourth-order WENO limiter is employed to solve the Vlasov equation. Compared with previous works of SL

method Vlasov equation solver, the CIPCSL3 method keeps the conservation in mass by propagating the VIA through a flux type conservative relation Equation (2.12).

For the boundary condition implementation, only one ghost cell needs to be applied to one side of the boundary because of the compact feature of CIPCSL3 method.

The pioneer works of HTs simulation with hybrid Vlasov-fluid model employed second-order schemes [39][41] to solve the Vlasov equation, which yield large numerical diffusion on a coarse mesh. The Vlasov equation solver developed in this dissertation achieved low numerical diffusion results on a coarse mesh, this feature will significantly reduce the storage of the calculation domain in multi-dimension simulation. The verifications of the method will be shown in the next chapter.

Chapter 3 Verification of CIPCSL3 method and Vlasov solver

A high resolution noiseless Vlasov equation solver is successfully developed under the CIPCSL3 framework. In this chapter, the CIPCSL3 method is verified through several test problems. The order of accuracy with fourth-order WENO limiter and second-order TVDCW limiter is checked through sinusoidal wave propagating problems. The ability to capture the discontinuities is tested by the one-dimensional square wave propulsion and two-dimensional rigid body test cases, and the applicability to solve the Vlasov equation is confirmed by solving the Vlasov-Poisson equation system. Linear Landau damping, nonlinear Landau damping and two-stream instability are discussed.

3.1 The Courant-Freidrich-Lewy condition

Considering the simply linear advection equation (Equation 2.10), the Courant-Freidrich-Lewy (CFL) condition[69] is defined as:

$$CFL = u\frac{\Delta t}{\Delta x}, \tag{3.1}$$

where Δt is the timestep for one loop in the simulation and Δx is the size of grid. The CFL condition represents the physical information propagate during one timestep inside the grid must be smaller than the grid size, which is $CFL < 1$.

For the numerical simulation, the CFL number or the timestep can be fixed to satisfy the stability condition. The test cases in this chapter employ the fixed CFL number, and the timestep is calculated by $\Delta t = CFL * \Delta x/u$. For the Vlasov equation solver, the CFL condition needs to be satisfied in each direction (x in space and v in velocity), the timestep for Vlasov equation solver reads:

$$\Delta t = CFL * \min\left(\frac{\Delta x}{u}, \frac{\Delta v}{a}\right), \tag{3.2}$$

where a is the acceleration of the physical valuable and Δv is the grid size in velocity space.

For the spatial accuracy and discontinuities test cases, $CFL = 0.4$ is used. For the Vlasov equation solver, the CFL number is set based on the problem requirement.

3.2 Outline of the code verification

Confirmation of the spatial accuracy

- Scalar sinusoidal wave propagation with periodic boundary condition in one dimension and two dimensions.

Confirmation of the ability to capture discontinuities

- One-dimensional square wave propagation, Jiang Shu's problem.
- Two-dimensional rigid body rotation.

Applicability of CIPCSL3 method to solve the 1D1V Vlasov-Poisson system

- Landau damping
  - Weak linear Landau damping
  - Strong nonlinear Landau damping

- Two stream instability
  - Confirmation of spatial accuracy in VP system
  - Comparison between fourth-order CIPCSL3 method and fully PIC method

3.3Confirmation of the spatial accuracy

In this subsection, the numerical test advected with the smooth distribution in one-dimension and two-dimension.

Case 3.1 One-dimensional sinusoidal wave advection

This test advects the non-dimensional profile with the linear advection equation:

$$\frac{\partial \tilde{f}}{\partial \tilde{t}} + \frac{\partial \tilde{f}}{\partial \tilde{x}} = 0, \tag{3.3}$$

where the initial condition reads:

$$\tilde{f}(\tilde{x}, 0) = \sin(2\pi\tilde{x}), \qquad \tilde{x} \in [0,1], \tag{3.4}$$

the periodic boundary condition is employed in x direction and the L_2 error is calculated by:

$$L_2 = \left(\frac{\sum(\tilde{f}^n - \tilde{f}_{ext})^2}{N} \right)^{\frac{1}{2}}, \tag{3.5}$$

where N is the number of grids. All the solution plots and L_2 errors are estimated at $t = 2.0$ (after two periods).

Figure 3.1 Shows the solution plots of each limiter with grid number $N_x = 50$, the WENO scheme achieved a good agreement with the exact solution, on the other hand, the TVDCW scheme created a plateau near the peak values, Figure 3.2 demonstrates the convergence speed of L_2 errors, Table 3.1 shows the L_2 errors with order of accuracy in space, each limiter achieved the design order of accuracy in 1D respectively.

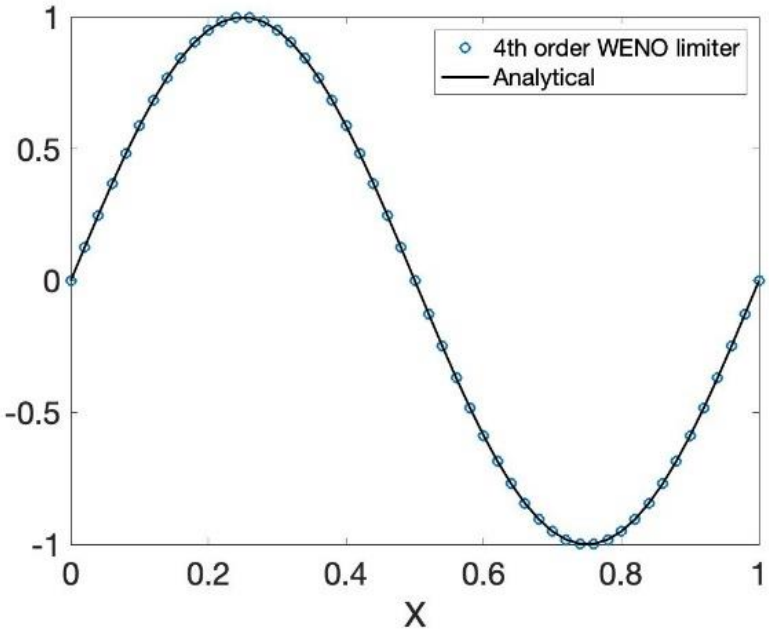

a) Fourth-order WENO limiter

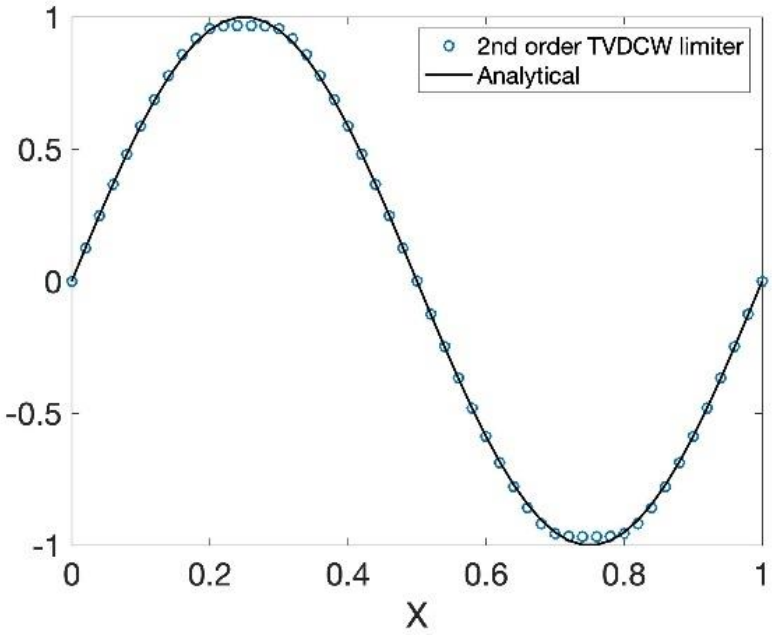

b) Second-order TVDCW limiter

Figure 3.1 Numerical solution of one-dimensional sinusoidal wave advection, $N_x = 50, \tilde{t} = 2.0$.

Table 3.1 L_2 errors and order of accuracy for one-dimensional test case, $\tilde{t} = 2.0$.

N_x	4th order WENO		2nd order TVDCW	
	L_2 error	order	L_2 error	order
50	2.85E-07		1.14E-02	
100	1.09E-08	4.74E+00	3.01E-03	1.92E+00
200	4.59E-10	4.56E+00	7.68E-04	1.97E+00
400	2.18E-11	4.39E+00	1.92E-04	2.00E+00
800	1.20E-12	4.19E+00	4.75E-05	2.02E+00

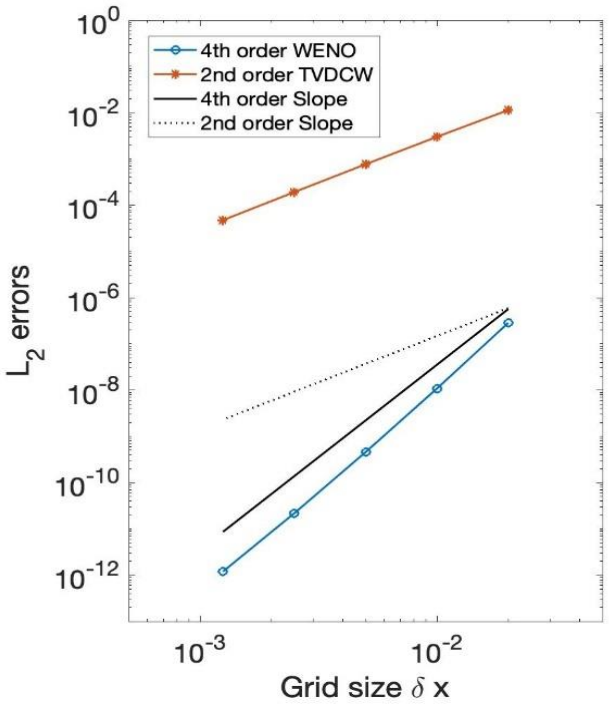

Figure 3.2 L_2 errors of one-dimensional test case.

Case 3.2 **Two-dimensional sinusoidal wave advection**

The two-dimensional sinusoidal wave is proposed by:

$$\frac{\partial \tilde{f}}{\partial \tilde{t}} + \frac{\partial \tilde{f}}{\partial \tilde{x}} + \frac{\partial \tilde{f}}{\partial \tilde{y}} = 0, \tag{3.6}$$

the non-dimensional initial condition follows:

$$\tilde{f}(\tilde{x}, \tilde{y}, 0) = \sin\big(2\pi(\tilde{x} + \tilde{y})\big), \quad \tilde{x} \in [0,1], \tilde{y} \in [0,1]. \tag{3.7}$$

the periodic boundary conditions are applied to both x and y directions. the simulation stops at $\tilde{t} = 2.0$.

Figure 3.3 gives the analytical solution contour plot at $\tilde{t} = 2.0$. Figure 3.4 plots the cross-section at $x = 0.5$ for each limiter with grid number of $N_x * N_y = 100 * 100$, the plateau created by the TVDCW scheme is confirmed in two-dimensional test case. Table 3.2 shows the L_2 error and the order of accuracy of each limiter in two-dimensional sinusoidal wave advection problem, the convergence speed is shown in Figure 3.5. Both limiters achieve the design spatial accuracy in 2D respectively.

Table 3.2 L_2 errors and order of accuracy for two-dimensional test case, $\tilde{t} = 2.0$.

$N_x * N_y$	4th order WENO		2nd order TVDCW	
	L_2 error	order	L_2 error	order
50*50	4.00E-07		8.03E-03	
100*100	2.37E-08	4.08E+00	2.09E-03	1.94E+00
200*200	1.45E-09	4.03E+00	5.35E-04	1.97E+00
400*400	8.18E-11	4.14E+00	1.35E-04	1.99E+00
800*800	5.20E-12	3.98E+00	3.30E-05	2.03E+00

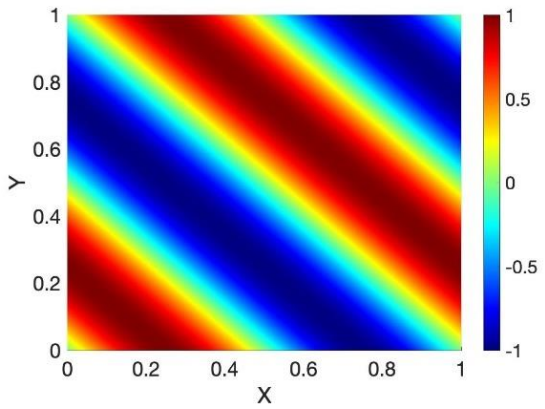

Figure 3.3 The analytical contour plot of two-dimensional sinusoidal wave advection.

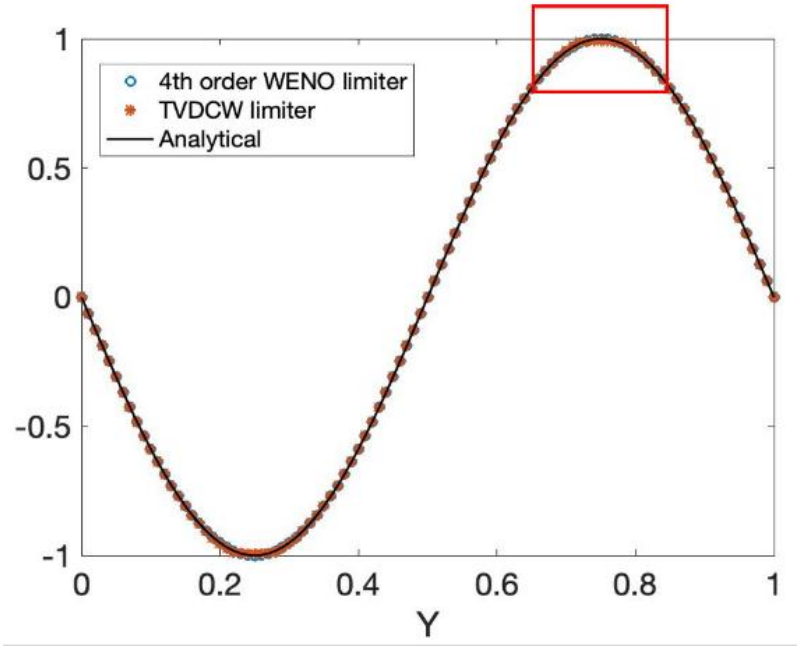

Cross-section plot

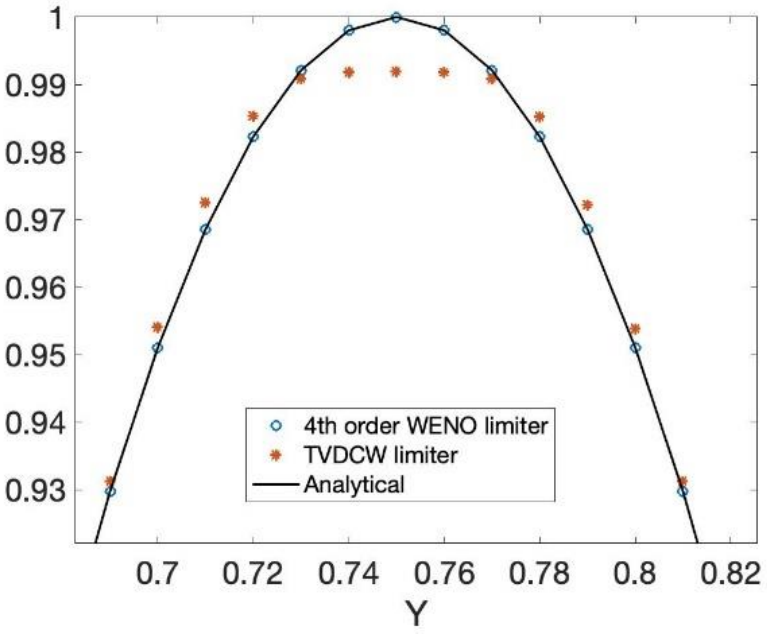

Local zoom-in view

Figure 3.4 Cross-section plots and the zoom-in view of two-dimensional sinusoidal wave advection at $x = 0.5$, $N_x * N_y = 100 * 100, \tilde{t} = 2.0$.

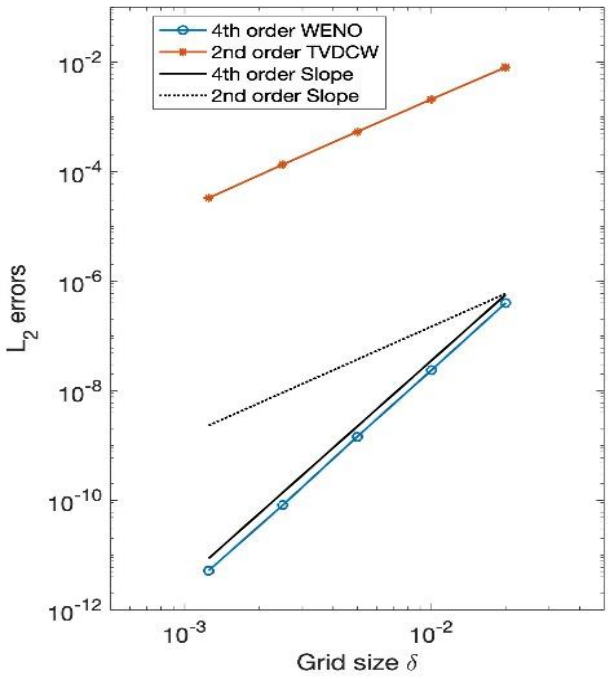

Figure 3.5 L_2 errors of two-dimensional test case.

3.4Confirmation of the ability to capture discontinuities

In this subsection, the ability to capture the jump discontinuities is investigated through the one-dimensional square wave transportation problem, Jiang Shu problem and two-dimensional rigid body rotation problem.

Case 3.3 One dimensional square wave transportation

Recalling the calculation condition in *Case 3.1*, the non-dimensional initial condition of square wave profile reads:

$$\tilde{f}(\tilde{x},0)=\begin{cases}1 & \text{if } 0.35\le\tilde{x}\le 0.65\\ 0 & \text{otherwise}\end{cases}, \tag{3.8}$$

the simulation runs with grid number of $N_x=100$ and stops at $t=2$ (two periods), Figure 3.6 shows the solutions of the two limters. Both algothams capture the jump

discontinuities without generate significant oscillations, the WENO limiter captures the sharp gradients of the wave within 5 grid points, meanwhile the TVDCW limiter captures it with 12 points.

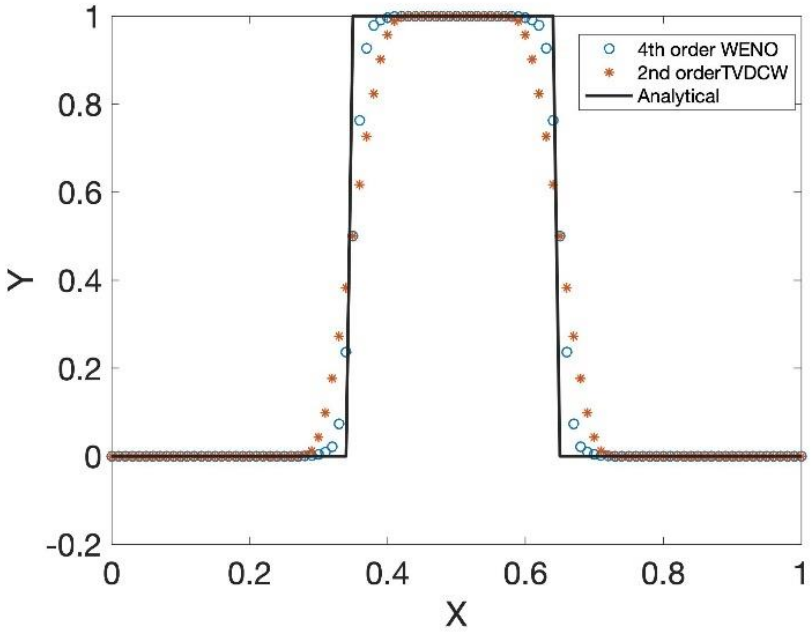

Figure 3.6 Numerical results of one-dimensional square wave transportation.$N_x = 100, \tilde{t} = 2.0$.

Case 3.4 **Jiang and Shu's linear advection test case**

This test was proposed by Jiang and Shu[70], here the initial condition follows the equation set (3.43) and the calculation domain is $\tilde{x} \in [-1,1]$ with periodic boundary condition, the calculation condition employed the grid number of $N_x = 200$. The functions inside the non-dimensional initial condition read:

$$G(\tilde{x},\beta,z) = \exp(-\beta(\tilde{x}-z)^2), F(\tilde{x},\alpha,a) = \sqrt{\max(1-\alpha^2(\tilde{x}-a)^2,0)}, \quad (3.9)$$

the coefficients are given by:

$$a = 0.5, z = -0.7, \alpha = 10, \delta = 0.005 \; and \; \beta = \frac{\log 2}{36\delta^2}, \tag{3.10}$$

and the initial condition follows:

$$f(x,0) = \begin{cases} \frac{1}{6}(G(x,\beta,z-\delta) + G(x,\beta,z+\delta) + 4G(x,\beta,z)), & -0.8 \le x \le -0.6 \\ 1, & -0.4 \le x \le -0.2 \\ 1 - \left|10(x-0.1)\right|, & 0 \le \widetilde{x \le 0.2} \\ \frac{1}{6}(F(\widetilde{x,\alpha},a-\delta) + G(\widetilde{x,\alpha},a+\delta) + 4G(\widetilde{x,\alpha},a)), & 0.4 \le \widetilde{x \le 0.6} \\ 0, & \text{otherwise} \end{cases}. \tag{3.11}$$

Jiang and Shu's problem evaluated the scheme's ability of capturing both discontinuities and smoothness profiles, Figure 3.7 shows the numerical results at $\tilde{t} = 2.0$, WENO scheme successfully obtains the correct waveforms, on the other hand, the CW limiter failed to predict the waveforms with sharp gradients. Figure 3.8 shows the long-time calculation features where $\tilde{t} = 200.0$ (100 periods). Compared with the TVDCW scheme, WENO shows the characteristics of high spatial resolution all the time.

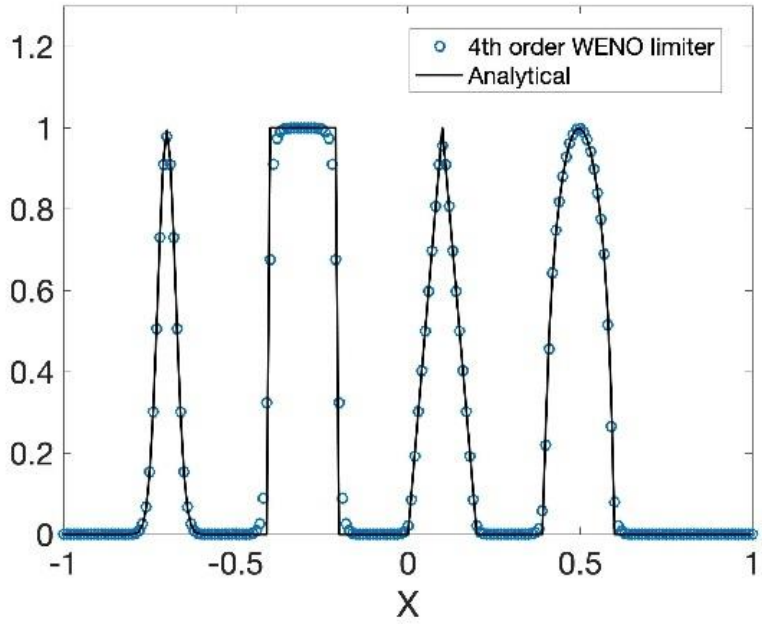

a) Fourth-order WENO limiter

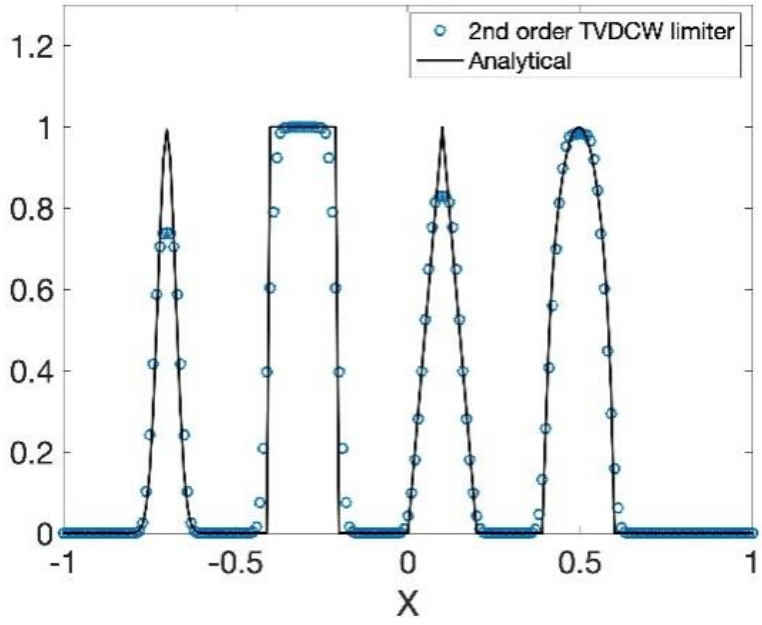

b) Second-order TVDCW limiter

Figure 3.7 Numerical results of Jiang and Shu's test case, $N_x = 200, \tilde{t} = 2.0$.

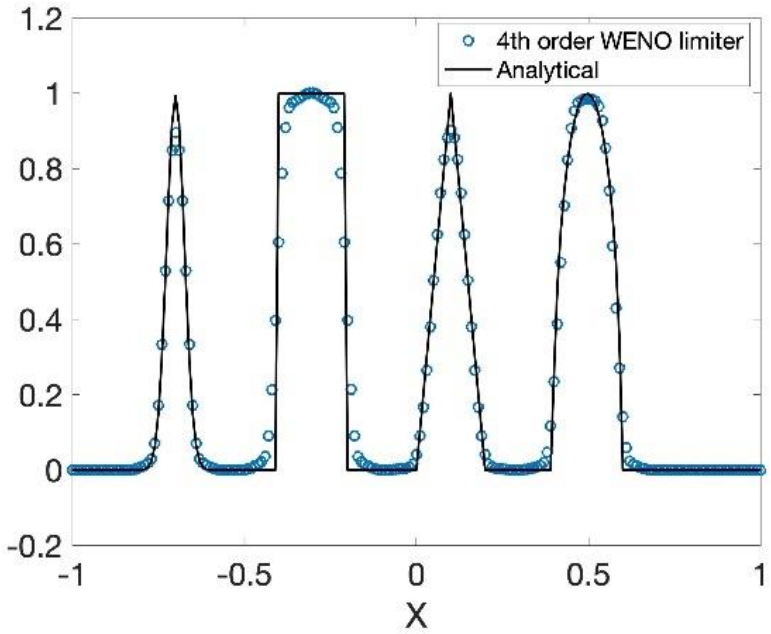

a) Fourth-order WENO limiter

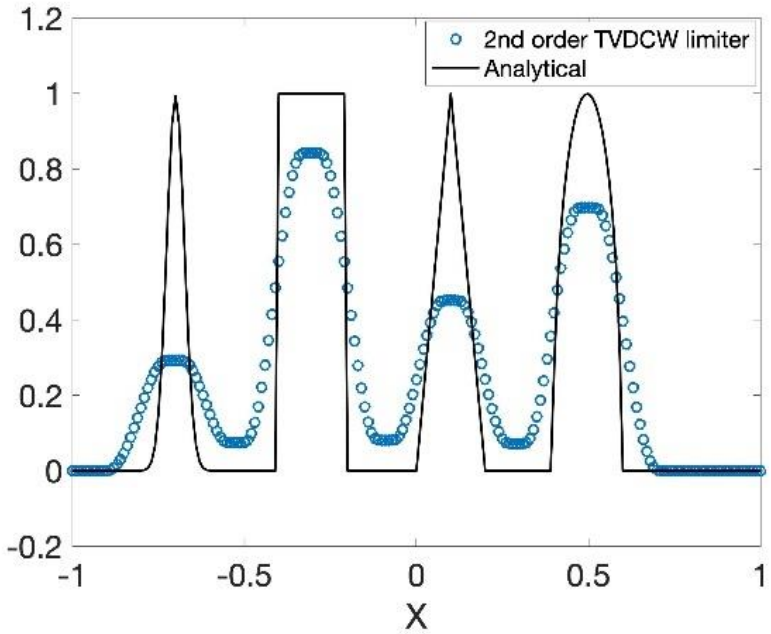

b) Second-order TVDCW limiter

Figure 3.8 Numerical results of Jiang and Shu's test case, $N_x = 200, \tilde{t} = 200.0$.

Case 3.5 **Two-dimensional rigid body rotation problem**

Considering the non-dimensional rigid body rotation problem:

$$\frac{\partial \tilde{f}}{\partial \tilde{t}} - (\tilde{y} - \frac{1}{2})\frac{\partial \tilde{f}}{\partial \tilde{x}} + (\tilde{x} - \frac{1}{2})\frac{\partial \tilde{f}}{\partial \tilde{y}} = 0, \tag{3.12}$$

the initial condition employed the smooth hump which follows:

$$\tilde{f}(\tilde{x}, \tilde{y}, 0) = \frac{1}{4}(1 + \cos(\pi r(\tilde{x}, \tilde{y}))), \tilde{x} \in [0,1], \tilde{y} \in [0,1], \tag{3.13}$$

where:

$$r(\tilde{x}, \tilde{y}) = \frac{\min\left(\sqrt{(\tilde{x} - x_0)^2 + (\tilde{y} - y_0)^2}, r_0\right)}{r_0}, \tag{3.14}$$

with $x_0 = 0.25, y_0 = 0.5\ and\ r_0 = 0.15$. A cone and a disk with radius of 0.15 and are centered at $(0.5,0.25)$ and $(0.5,0.75)$ are also concerned[76][77].

Figure 3.9 gives the initial condition for the three-rigid body. Periodic boundary conditions are employed, and the calculation conditions are: $N_x * N_y = 100 * 100, \tilde{t} = 12\pi$ (Six periods).Figure 3.10 shows the contours plot after 6 periods, the discontinues has been captured successfully without oscillations by WENO scheme, on the other hand, the TVDCW scheme flats the maximum value of the cone and smooth hump, and it generates small oscillations inside the domain.

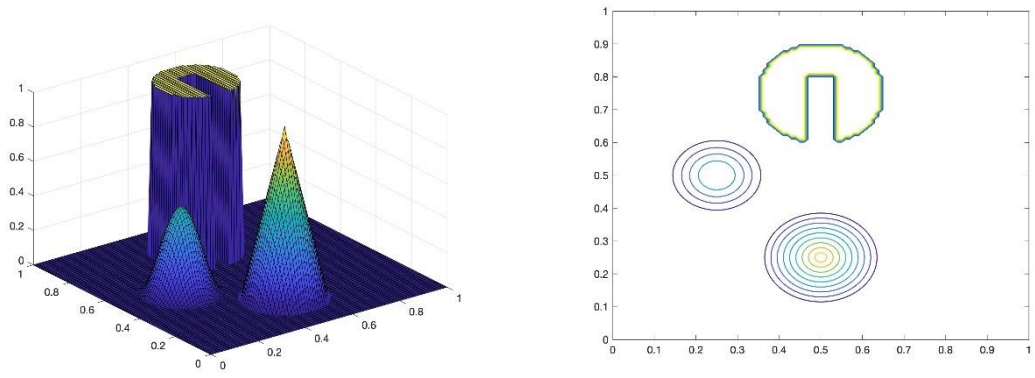

Initial profile　　Initial countor

Figure 3.9 Initial condition of rigid body rotation problem, $N_x * N_y = 100 * 100$.

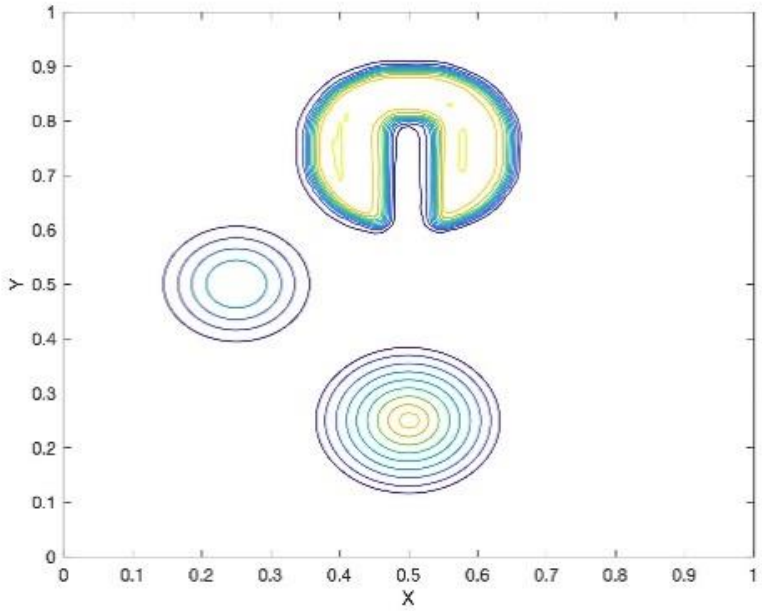

a) Fourth-order WENO limiter

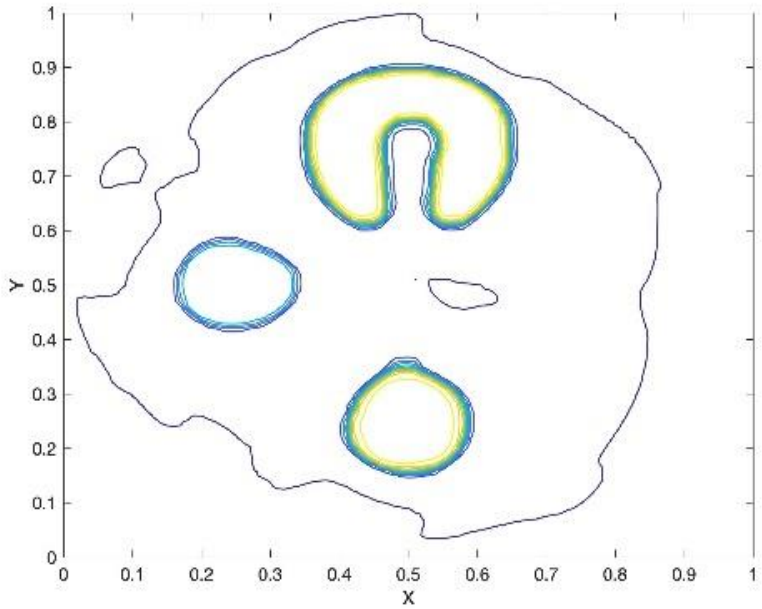

b) Second-order TVDCW limiter

Figure 3.10 Contours of rigid body rotation, $N_x * N_y = 100 * 100, \tilde{t} = 12\pi$.

Figure 3.11, Figure 3.12 give several cross-sections along x and y axial, the TVDCW scheme creates a plateau near the maximum values of each wave, leading to a distortion in waveform.

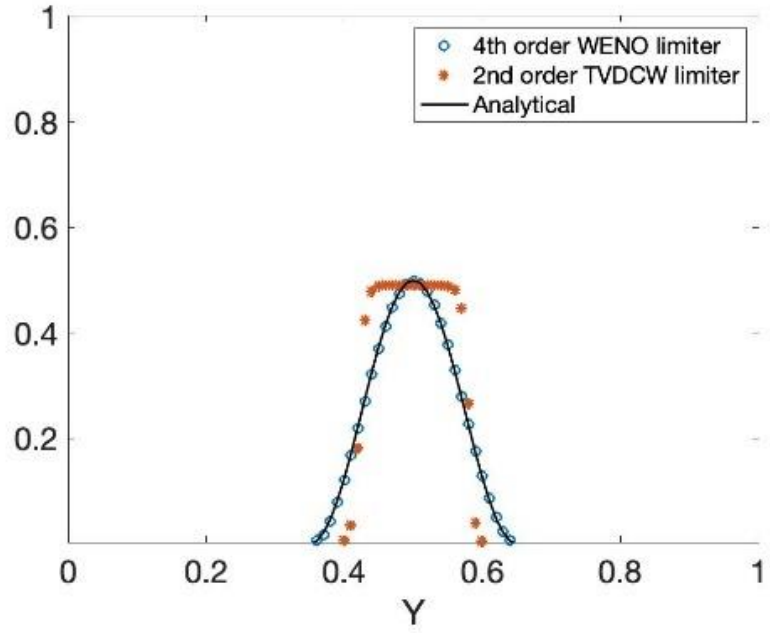

$x = 0.25$

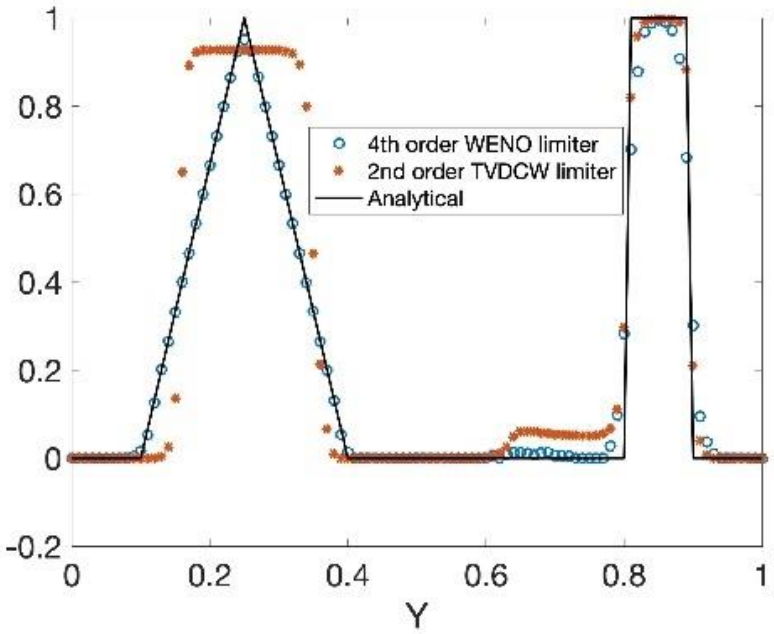

$x = 0.5$

Figure 3.11 Numerical results of rigid body rotation, cross-sections at $x = 0.25$ and $x = 0.5$.

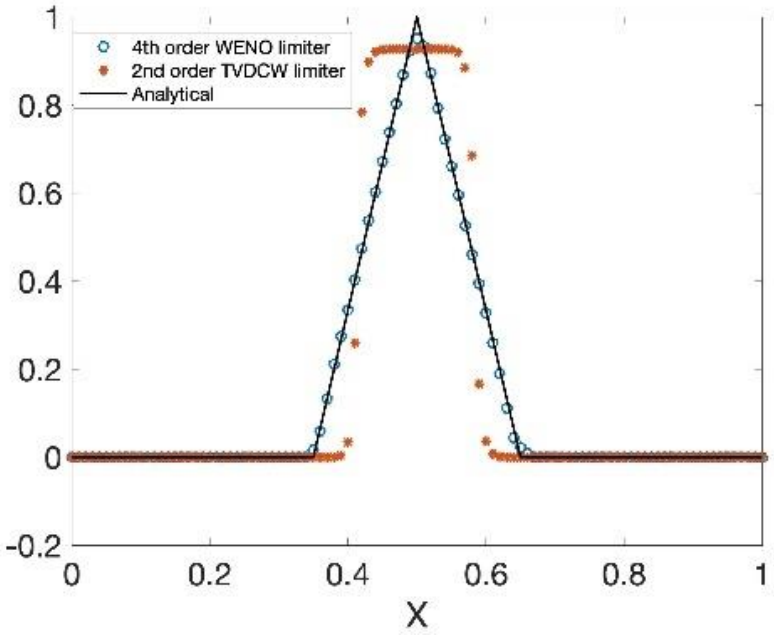

$y = 0.25$

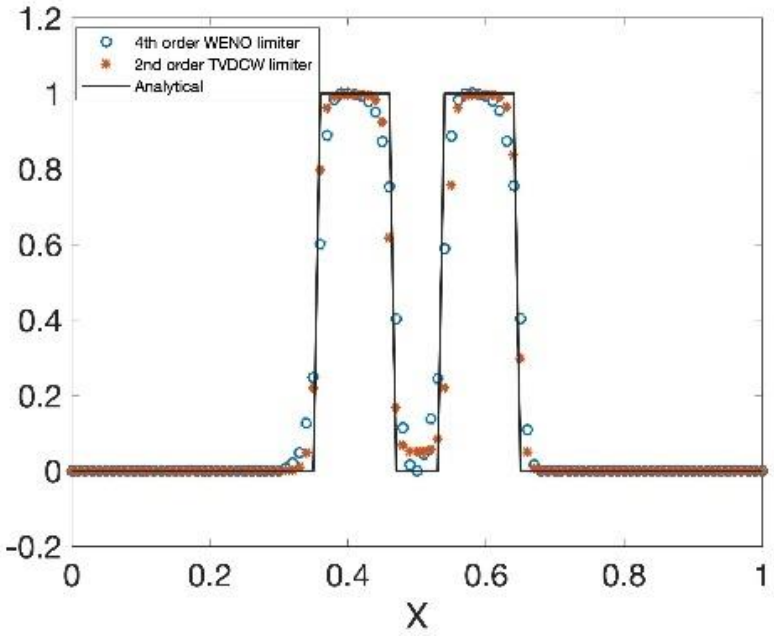

$y = 0.75$

Figure 3.12 Numerical results of rigid body rotation, cross-sections at y= 0.25 and $y = 0.75$.

3.5 Applicability of CIPCSL3 method to solve the 1D1V Vlasov-Poisson system

This subsection shows the verification of CIPCSL3 Vlasov equation solver by solving the test problems of Landau damping and two stream instability based on the 1D1V VP system. Following physical quantities can be checked numerically to investigate the quality of the numerical scheme:

L_p norm:

$$L_p = \iint |f(x,v,t)|^p dxdv\,, \tag{3.15}$$

Kinetic energy:

$$\text{Energy} = \iint f(x,v,t)v^2 dxdv + \int E(x)^2 dx\,. \tag{3.16}$$

3.5.1 Governing equations for Vlasov-Poisson equation system

The VP equation system in 1D1V phase (one dimension in space and one dimension in velocity) reads:

$$\begin{aligned} &\frac{\partial f}{\partial t} + v\frac{\partial f}{\partial x} + E(x,t)\frac{\partial f}{\partial v} = 0 \\ &\frac{\partial E}{\partial x} = \int_{-\infty}^{+\infty} f(x,v,t)dv - 1 \end{aligned}\,. \tag{3.17}$$

Here, the ion distribution function is assumed to be uniform and unchanged as the background charge. Only electron distribution function is handled during the simulation. The Vlasov equation can be solved through the CIPCSL3 method with Strang splitting and the electric field can be simulated through the direct integral method of Poisson's equation, or, if the boundary condition of Poisson's equation is periodic, the pseudo

spectral method can be applied[78].

By employing the second-order Strang splitting, the calculation procedures in one time step for the VP system can be expressed as:

Step 1: Advect the electron distribution function f_e in x direction for half time step $\Delta t/2$.

Step 2: Generate the electric field through Poisson's equation solver. (By FFT, tridiagonal method or hyperbolic approach[87]).

Step 3: Advect electron distribution function f_e in v direction for fully time step Δt.

Step 4: Repeat step 1.

Figure 3.13 shows the flow chat of the Vlasov equation solver for VP system.

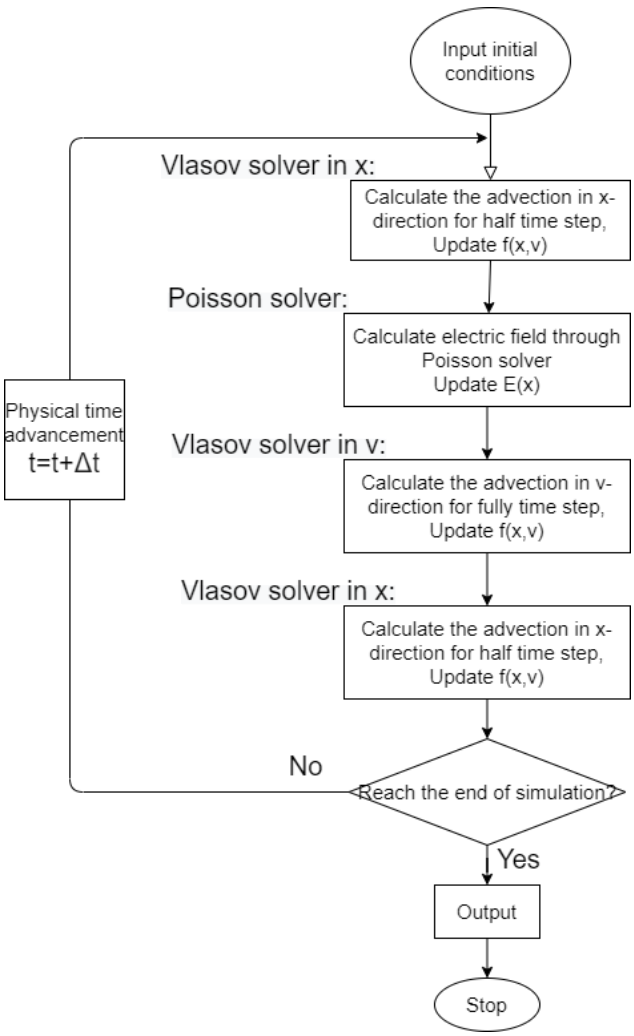

Figure 3.13 Flowchart of the Vlasov equation solver for VP system.

3.5.2 Boundary conditions

Boundary conditions need to be implemented for 1D1V Vlasov equation in two directions, the test cases below all employ the periodic boundary conditions in the x direction and zero boundary conditions in the v direction.

For the inlet and outlet boundary condition, the particles that flow into the calculation domain with $u > 0$ at $x = 0$ and $u < 0$ at $x = L$, where $x = 0$ is the left-end and $x = L$ is right-end of the calculation domain. If the shape of the distribution function is smooth, simply Lagrange polynomial with the same order of the scheme can be used for the extrapolation to keep the same resolution at the boundary[79][80], if the distribution function flows in with a sharp gradient, the WENO extrapolation[81] can be applied to keep the simulation stable at each boundary. Since CIPCSL3 method is a compact method, only one ghost cell needs to be applied at each boundary, which simplify the boundary condition implementation significantly.

The boundary condition in v direction is simply to implement if the upper boundary and lower boundary are large enough. The distribution function at the boundary will become zero since there are no particles near each velocity boundary. The Dirichlet boundary condition can be set as zero in the ghost cell and Neumann condition can also be set as the gradient equal to zero.

3.5.3 Frequency resolution of Poisson's equation solver

In the last part of this chapter, the applicability of CIPCSL3 method to 1D1V Vlasov-Poisson equation system is investigated through the Landau damping and two stream instability problems. Since the periodic boundary conditions are employed in space for both cases, the pseudo spectral method[88] can be applied to solve the

Poisson's equation[89].

The sampling frequency will affect the frequency resolution of the pseudo spectral method. For a problem that defined on $x \in [0, L]$ with grid number of N, the sampling frequency is the same with N. Sonnendrücker[90] presented that the pseudo spectral solver showed a very quickly convergence speed with different grid size $h = L/N$ compared with second-order and fourth-order finite differences methods (Figure 3.14). It proves that the pseudo spectral solver for Poisson's equation will not affect the order of accuracy in space due to the fast convergence speed related to the mesh size.

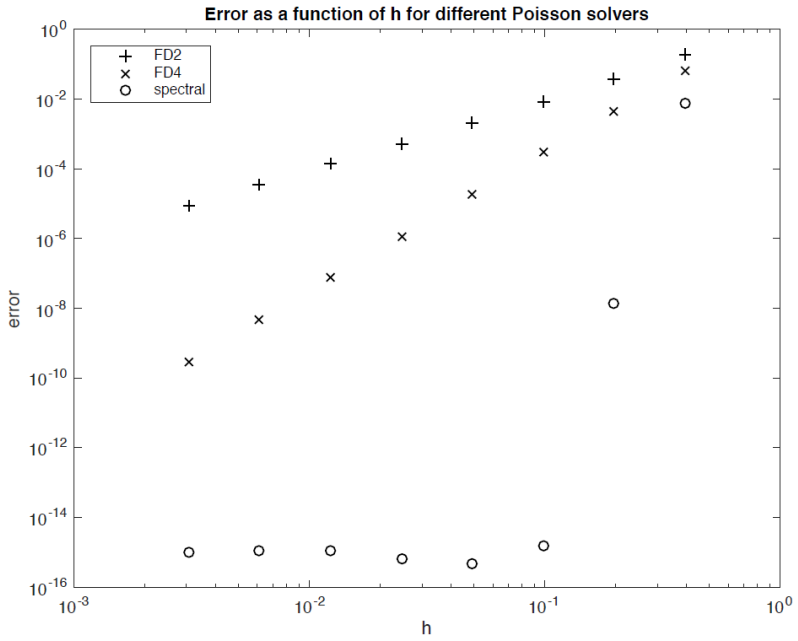

Figure 3.14 Error as a function of grid size periodic Poisson problem for second-order Finite Differences (FD2), fourth order Finite Differences (FD4) and pseudo spectral method[90].

3.5.4 Landau damping

3.5.4.1 Physic of Landau damping

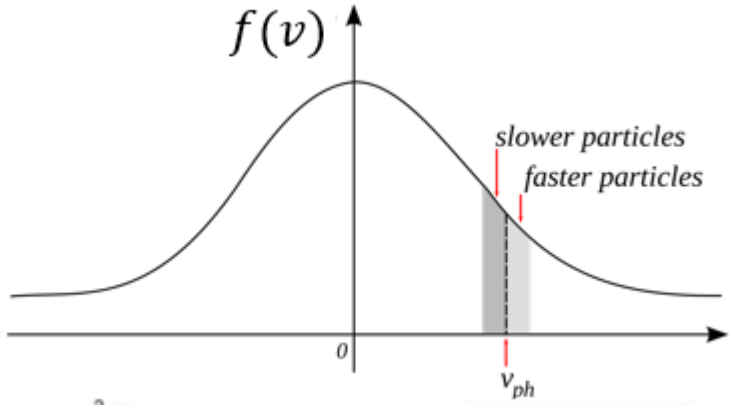

Figure 3.15 Schematic of distribution function for Landau damping.

Landau damping has been widely used for the verification of VP system. These Langmuir oscillations was first predicted by Landau[82]. It arises due to the interaction between the electromagnetic wave with phase velocity v_{ph} and particles in the plasma that hold a close speed with v_{ph}[83]. The slower particles will get the energy from the electric field and accelerate to the speed of v_{ph} and the faster particles will lose energy to the electromagnetic wave. Figure 3.15 gives the schematic of slower and faster particles following the distribution function $f(v)$.

The damping rate can be estimated through [84]:

$$\gamma = -\frac{\pi\omega_{\mathrm{p}}^3}{2k^2 n_{\mathrm{e}}}\left[\frac{\partial f_0}{\partial v}\right]_{v_{\mathrm{ph}}}, \tag{3.18}$$

where $k = 2\pi/\lambda_0$ is the wave number, λ_0 is the wave length, f_0 is the normalized velocity distribution function, n_e is the electron number density which $n_{\mathrm{e}} = \int f_0 dv$, ω_{p} is the plasma oscillation frequency and v_{ph} is the phase velocity. If the velocity distribution function employed the Maxwellian distribution, the damping rate becomes:

$$\gamma = -\sqrt{\frac{\pi}{8}}\frac{1}{(k\lambda_{\mathrm{D}})^3}\frac{\omega}{\omega_{\mathrm{p}}}\exp\left(\frac{1}{2}\left(\frac{\omega}{kv_{\mathrm{th}}}\right)^2\right), \tag{3.19}$$

where $\lambda_{\mathrm{D}} = v_{\mathrm{th}}/\omega_{\mathrm{p}}$ is the Debye length and v_{th} is the electron thermal velocity.

For Landau damping case, the L_2 norm of electric field is always investigated for the damping rate analyses.

3.5.4.2 Numerical test cases

All the Landau damping test cases employed the same calculation condition if not special specified:

$$N_x * N_v = 50 * 50, x \in \left[0, \frac{2\pi}{k}\right], y \in [-2\pi, 2\pi], CFL = 0.1, \tag{3.20}$$

where N_x and N_v are the grid number in space and velocity and k is the wave number. The initial condition reads:

$$f(x, v, 0) = \big(1 + Acos(kx)\big)f_{\mathrm{M}}(v), \tag{3.21}$$

where A is a small perturbation in density and $f_M(v)$ is the Maxwellian distribution:

$$f_M(v) = (2\pi)^{-\frac{1}{2}}\exp\left(-\frac{v^2}{2}\right), \tag{3.22}$$

Case 3.6 Weak linear Landau damping

For the weak linear Landau damping case, the small density perturbation $A = 0.01$. Figure 3.16 shows the time history results of electric field in L_2 norm with three different wave numbers, both schemes solve the electric field decay rate correctly. Since the L_2 norm is an integrated value over the whole calculation domain, it is not very sensitive to

the spatial resolution. The comparison of the spatial resolution will be demonstrated in the latter two stream instability problem. Even compared with the electric field's L_2 norm, the WENO scheme shows a highly resolution feature that it can simulate the tail of L_2 norm lower than 10^{-8} in each problem.

In Landau damping, the small density perturbation causes the fluctuation in velocity space. Because of the periodic boundary conditions, the phase is mixed in each period, leading to a frequency growth in time. When the grid in velocity space cannot capture the fluctuations, the unphysical recurrence phenomena occurred. For the case with wavenumber of $k = 0.5$, the recurrence phenomena[85][86] occurred at 48s, which shows an agreement with the theoretical one $T_{\text{the}} = 2\pi/(k\Delta v) = 50\ s$.

Figure 3.17 demonstrates the physical quantities of weak linear Landau damping in the case of $k = 0.5$. Since the density perturbation is small, there shows no significantly difference between each scheme, both schemes present the conservative features.

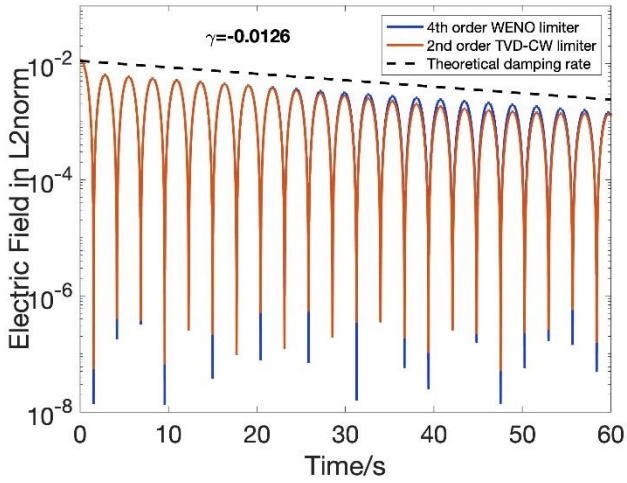

$k = 0.3$

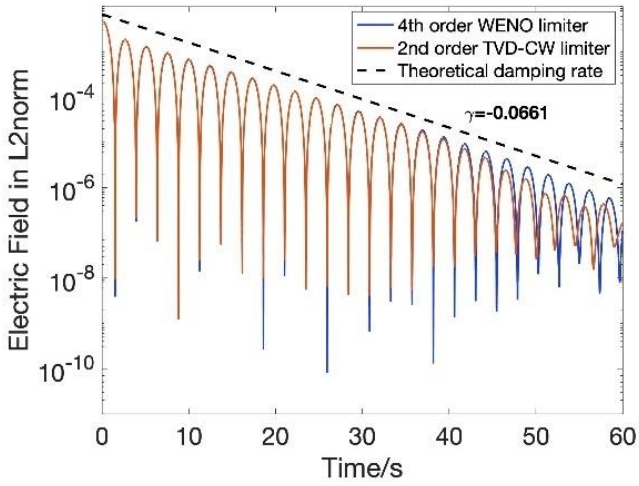

$k = 0.4$

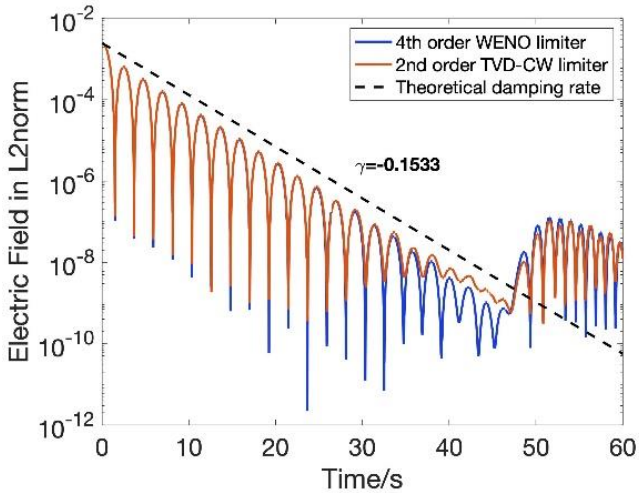

$k = 0.5$

Figure 3.16 Weak linear Landau damping. Time history of electric field in L_2 norm with different wave numbers, top: $k = 0.3$, middle: $k = 0.4$, bottom: $k = 0.5$, dash line shows the theoretical damping rate of each case.

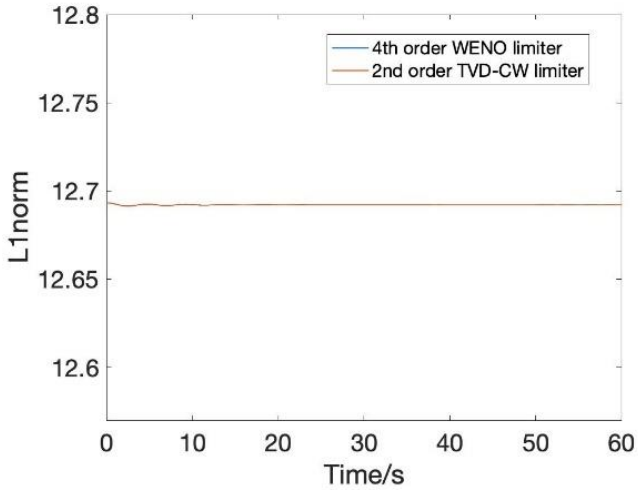

L_1 norm of distribution function f

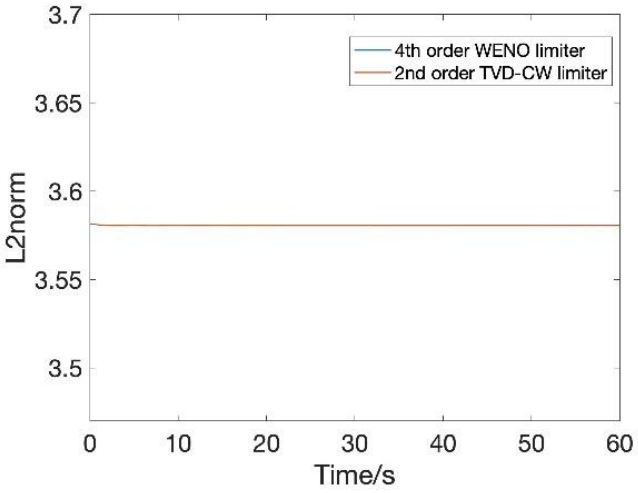

L_2 norm of distribution function f

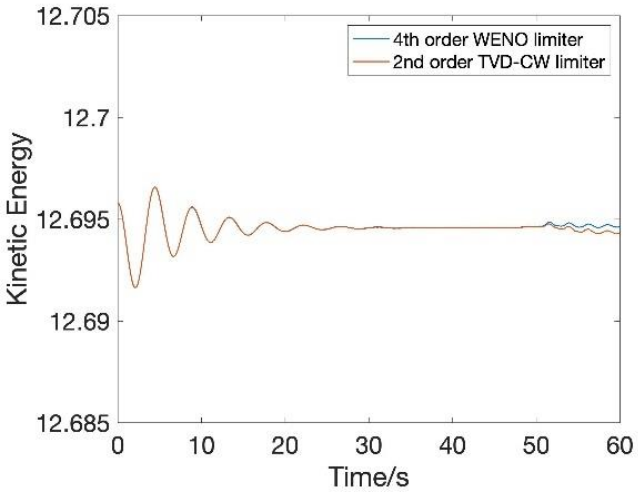

Kinetic energy

Figure 3.17 Weak linear landau damping, physical quantities of L_1 norms (top) and L_2 norms (middle) for the distribution functions and kinetic energy (bottom), $k = 0.5$.

Case 3.7 **Strong nonlinear Landau damping**

The strong nonlinear Landau damping employed the initial condition of Equation (3.21), with a big density perturbation $A = 0.5$ and wave number $k = 0.5$. Here the first linear decay rate generated by the WENO scheme is $\gamma_1^W = -0.2893$, almost the same with TVDCW scheme $\gamma_1^{CW} = -0.2891$. Compared with other literatures, it is a litter bigger than the value of $\gamma_1 = -0.281$, presented by Cheng and Knorr[50], $\gamma_1 = -0.281$ presented by Wei[77], identical to Rossmanith[57] with $\gamma_1 = -0.292$ and Heath[56] with $\gamma_1 = -0.288$. The WENO scheme also predicts the second growth rate, which is $\gamma_2^W = 0.0829$ on the other the TVDCW scheme fails to capture this growth rate, which may due to the numerical diffusion caused by the TVDCW scheme. The growth rate also compared with the same literatures, the sum-up results are shown in Table 3.3.

Table 3.3 Damping and growth rate of Strong nonlinear Landau damping, compare with other literatures.

	γ_1 damping rate	γ_2 growth rate
4th order WENO	-0.2893	0.0829
2nd order TVDCW	-0.2891	Failed
Cheng and Knorr[50]	-0.2812	0.084
Wei Guo[77]	-0.281	0.0813
Rossmanith[57]	-0.292	0.0815
Heath[56]	-0.288	0.0746

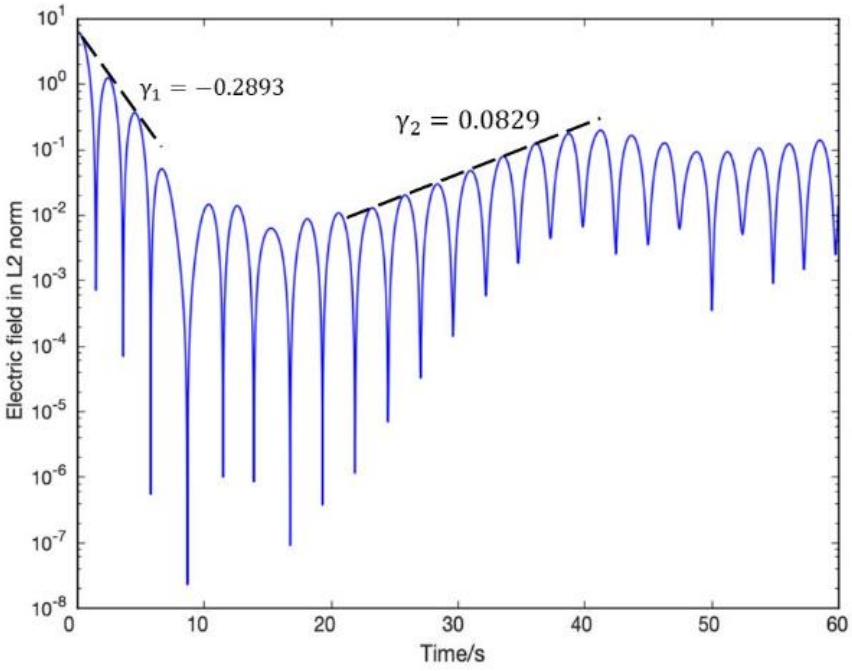

a) Fourth order WENO limiter

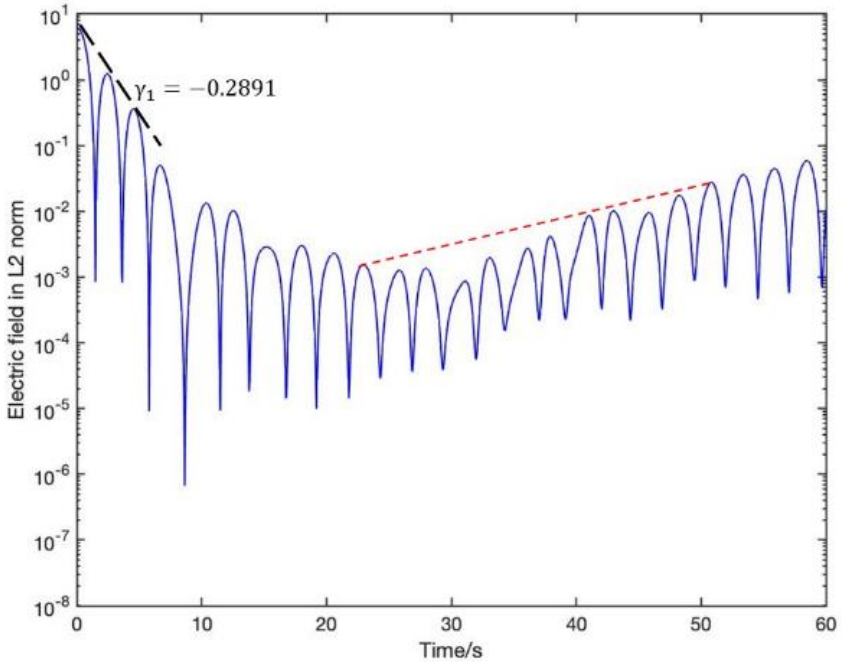

b) Second-order TVDCW limiter

Figure 3.18 Strong nonlinear Landau damping, Time history of electric field in L_2 norm.

Figure 3.19 shows the distribution function comparison of the two schemes at $t = 30$ s, the TVDCW scheme case was running with the grid number of $N_x * N_v = 200 * 200$. more beneficial resolution is observed with the high-order WENO scheme. By employing the grid number with four times finer that the WENO scheme, the second-order TVDCW scheme somehow achieved the same resolution as WENO did, but the calculation time will be increased by 16 times due to the increasing in grid number. The features that high-order scheme achieved a fast convergence speed in the smooth regime, and shows less dissipation near the sharp gradient or discontinuities are confirmed.

Figure 3.20 gives the physical quantities of *Case* 3.7, the fourth-order WENO scheme's L_1 norm of distribution function f shows an oscillate result than the second-order TVDCW scheme because although the CIPCSL3 method is mass conservative, the WENO limiter is not positivity preserving, it will generate very small under shooting in the region that the value of distribution function is near zero. The minimum value of distribution function at $t = 60s$ is: $\min(f(x, v, 60)) = -0.00053$.

Figure 3.21 demonstrates the time evolution of the distribution function, the results are analogous to what Qiu and Christlieb[53] shown in their paper, since Qiu employed the ninth-order WENO reconstruction for the same plot, some more details were shown in her results compared with this work.

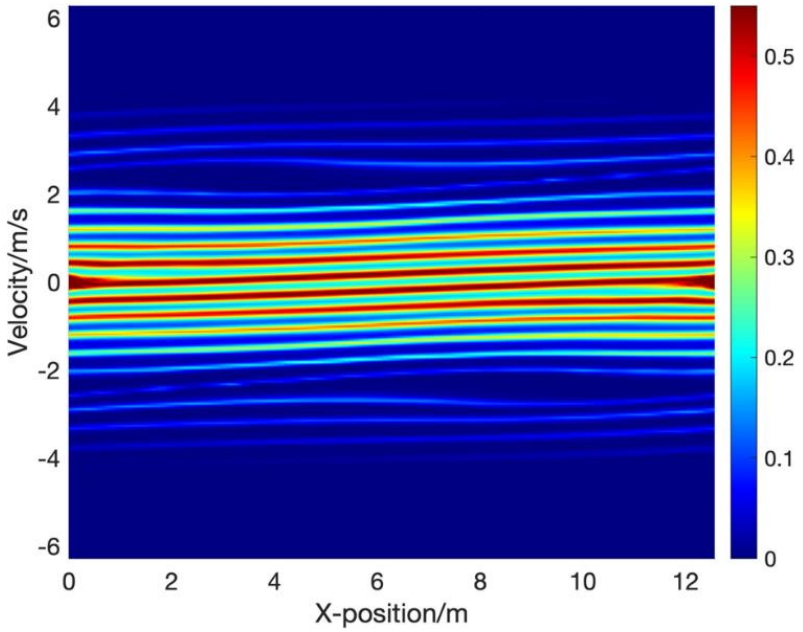

a) Fourth-order WENO limiter

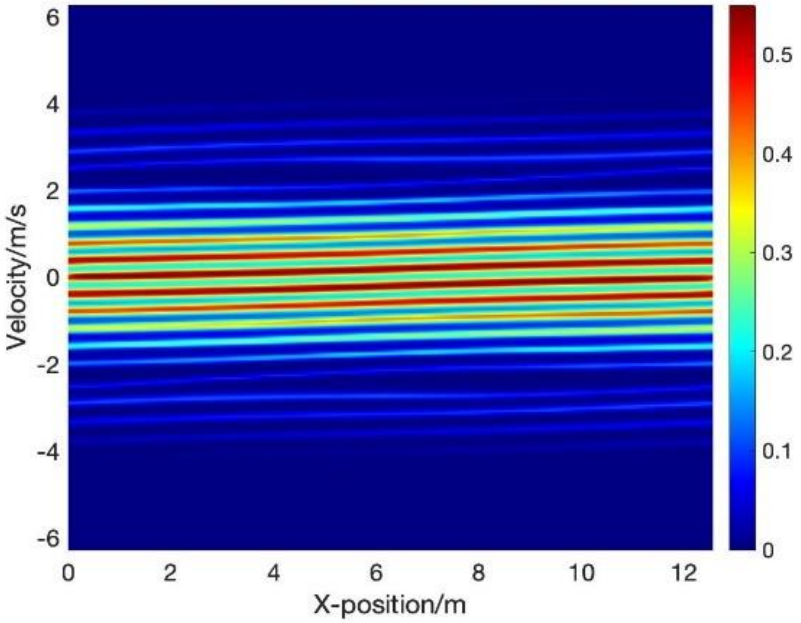

b) Second-order TVDCW limiter

Figure 3.19 Strong nonlinear Landau damping, contours of distribution function at $t = 30$ s, the lower figure b) running with grids number of $N_x * N_v = 200 * 200$.

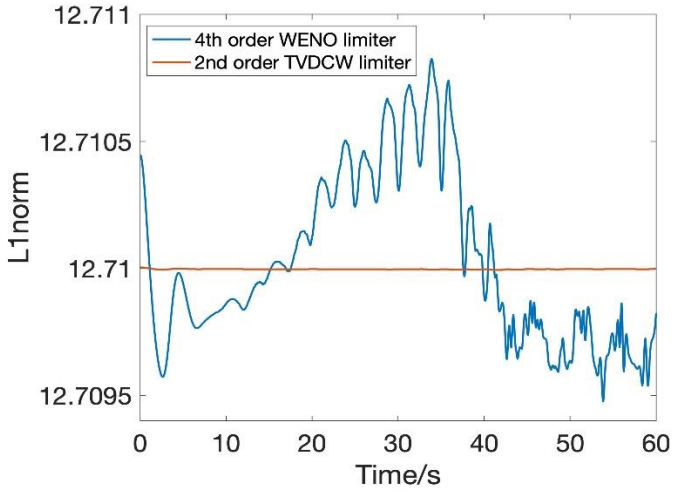

L_1 norm of distribution function f

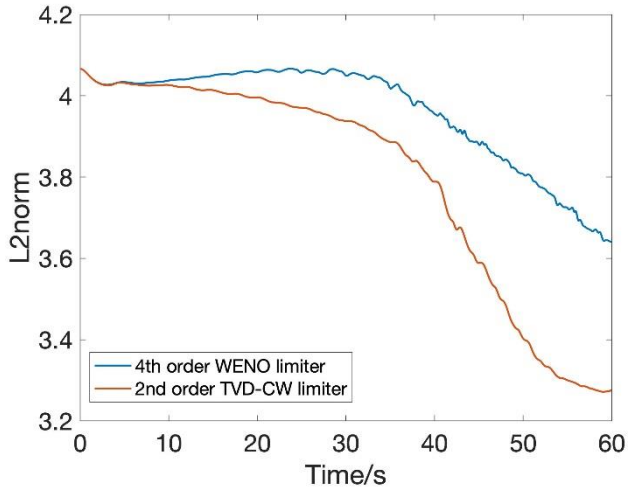

L_2 norm of distribution function f

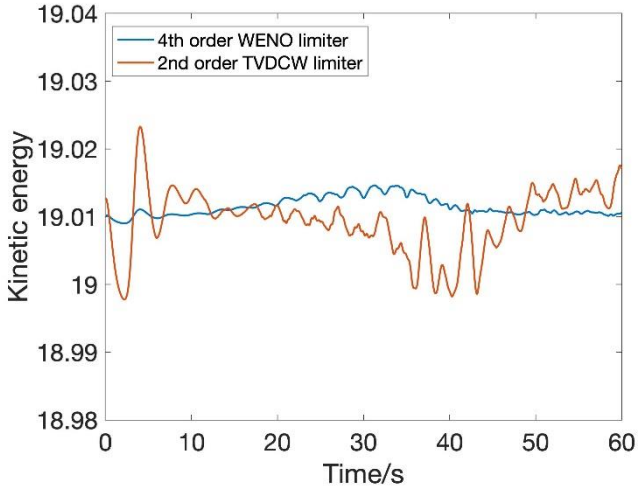

Kinetic energy

Figure 3.20 Strong nonlinear Landau damping, physical quantities of L_1 norms (top) and L_2 norms (middle) for the distribution functions and kinetic energy (bottom).

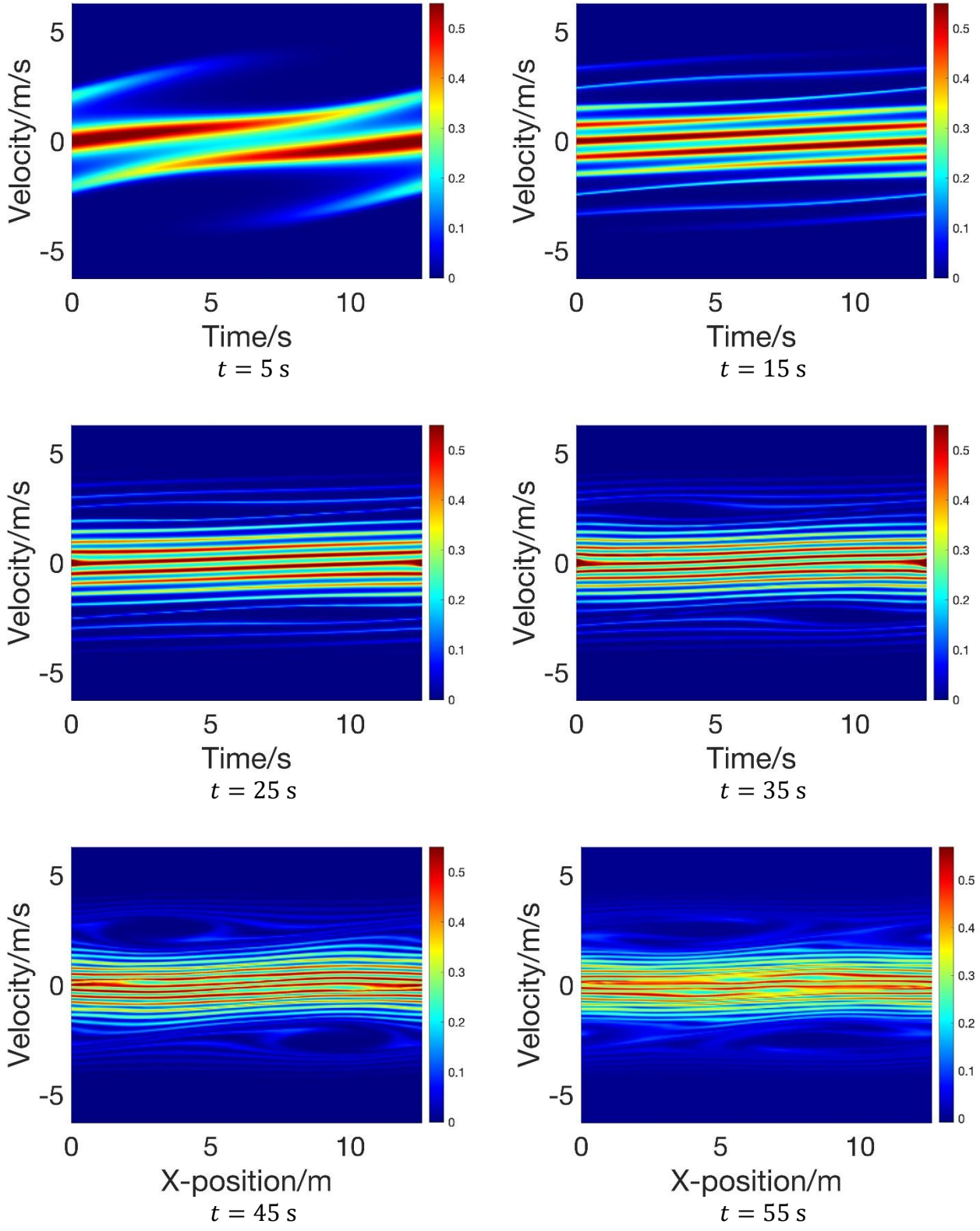

Figure 3.21 Strong nonlinear Landau damping, Time history of distribution function at different physical time level, fourth-order WENO scheme.

3.5.5 Two stream instability

In this subsection, the spatial accuracy and temporal accuracy have been checked. Since there was no analytical solution for the two stream instability case, the numerical solution with a very fine mesh was calculated as the reference. The L_2 error was calculated based on the fine mesh results. At the last part of this subsection, the same test was running with PIC method to compare the smoothness and resolution with fourth-order WENO scheme.

3.5.5.1 Physic of two stream instability

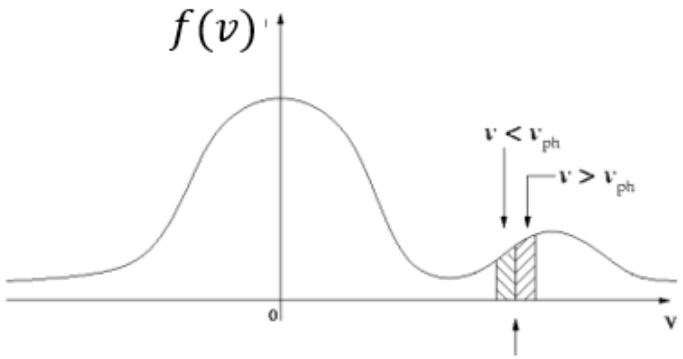

Figure 3.22 The bump on tail structure of distribution function.

The two stream instability behaviors as the inversed energy transportation of Landau damping. When an electron beam with high energy jet into a thermal equilibrium plasma, it will create a bump-on-tails structure which is shown in Figure 3.22. If the distribution function holds a positive gradient at the phase speed v_{th}, there would be more particles with the speed a bit greater than v_{th}. The energy will transfer from the faster particles to the wave, which may lead to an exponential increase rate of wave energy, this phenomenon stops when the particles with high energy are all trapped by the electric field. The trapping particles create a circular profile in the middle of the domain.

3.5.5.2 Numerical test cases

Case 3.8 Confirmation of spatial accuracy

Considering the initial condition of:

$$f(x,v,0) = \left(1 + Acos(kx)\right)v^2 f_M(v), \tag{3.23}$$

where $f_M(v)$ is the Maxwellian distribution which shown in Equation (3.22). Here assume $A = 0.05$ and $k = 0.5$, respectively. The calculation conditions are: $N_x * N_v = 100 * 100, CFL = 0.1$.

Figure 3.23 and Figure 3.24 demonstrate the numerical results of distribution functions and the cross-sections at $x = 2\pi$ at $t = 30s$ and $t = 45s$. The WENO scheme shows a better resolution to capture the filamentation structures than the TVDCW scheme. Figure 3.25 gives the physical quantities of *case3.8*, the same oscillations in L1 norm of distribution function are observed as in *case3.7* due to the non-positivity preserving feature. High-order WENO scheme provides a better conservative feature in L2 norm and kinetic energy than the TVDCW scheme.

Since the two stream instability case has no analytical solution, to check the spatial convergence speed quantitatively, a test case with gird number of $N_x * N_v = 800 * 800$, CFL= 0.1 is simulated as a reference result. The simulation stops at $t = 0.5\ s$. The L_2 errors are calculated through:

$$L_2 = \left(\frac{\sum \left(f(x,v,t_1) \quad - f_{ref}(x,v,t_1) \right)^2}{N_x * N_v} \right)^{1/2}. \tag{3.24}$$

Table 3.5 give the order of spatial accuracy in x direction and v direction, the

expected spatial accuracies of the schemes are confirmed. Fourth-order WENO scheme provides a better performance than the second-order TVDCW scheme. To get the same resolutions of the waveform, second-order scheme needs to employed four times finer grid number than the fourth-order one, and the computational time will be increased about sixteen times.

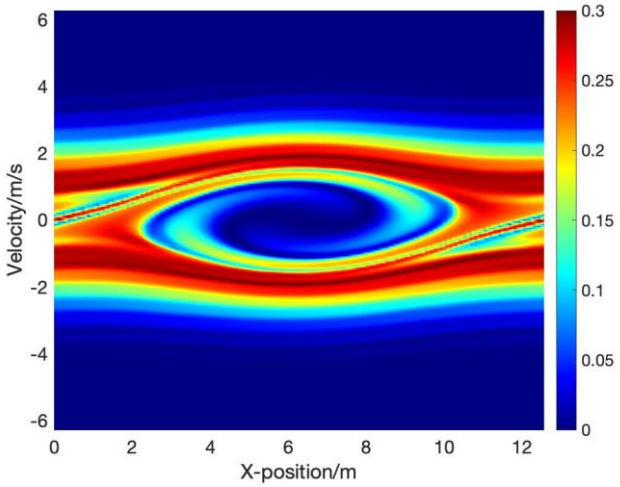

a) Fourth-order WENO limiter

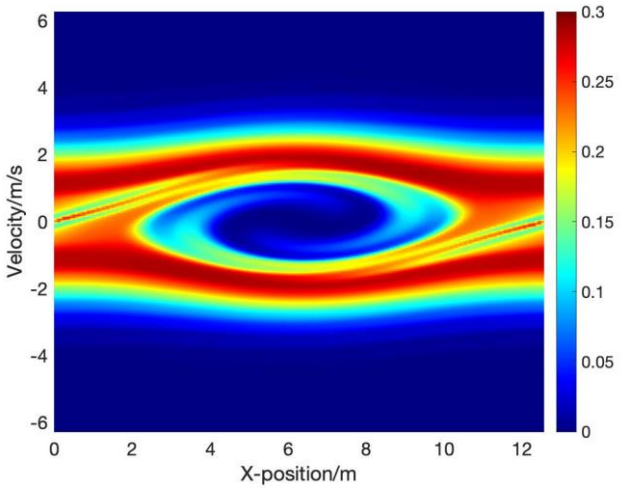

b) Second-order TVDCW limiter

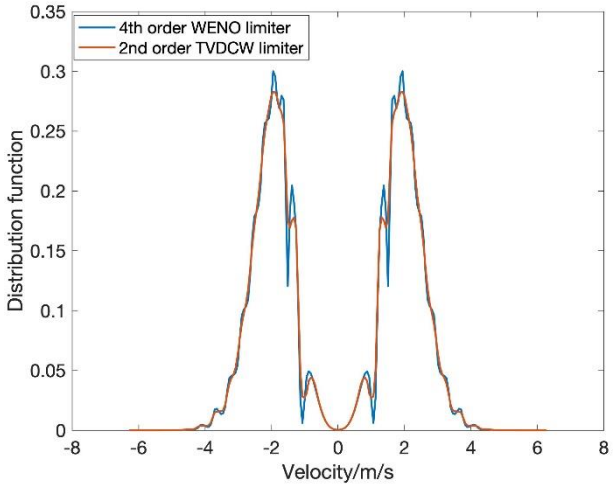

Cross-section at $x = 2\pi$

Figure 3.23 Two stream instability, the cross-section is at $x = 2\pi$. $N_x * N_v = 100 * 100, CFL = 0.1, t = 30$ s.

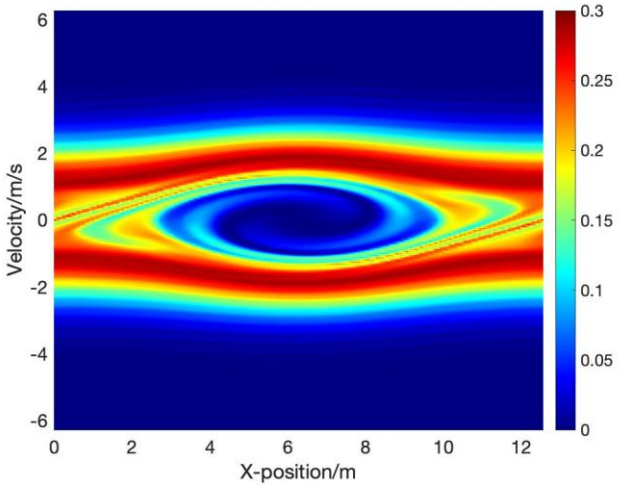

a) Fourth-order WENO limiter

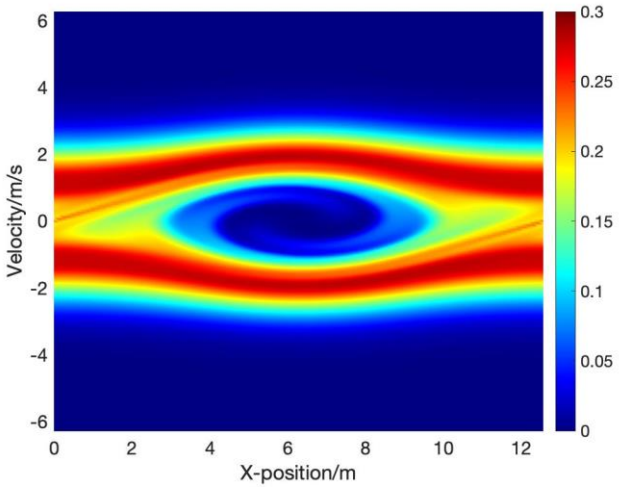

b) Second-order TVDCW limiter

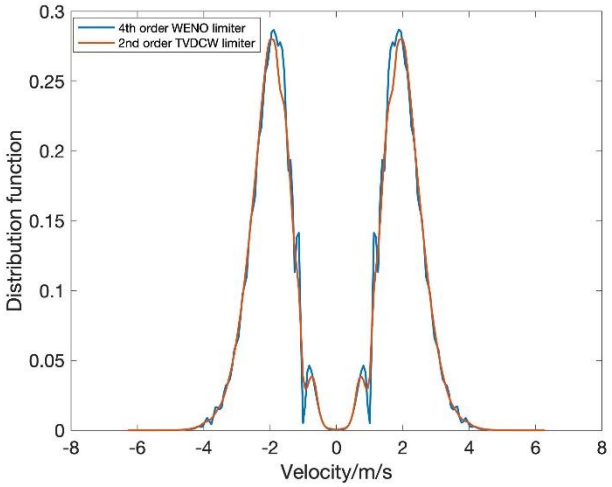

Cross-section at $x = 2\pi$

Figure 3.24 Two stream instability, the cross-section is at $x = 2\pi$. $N_x * N_v = 100 * 100, CFL = 0.1, t = 45$ s.

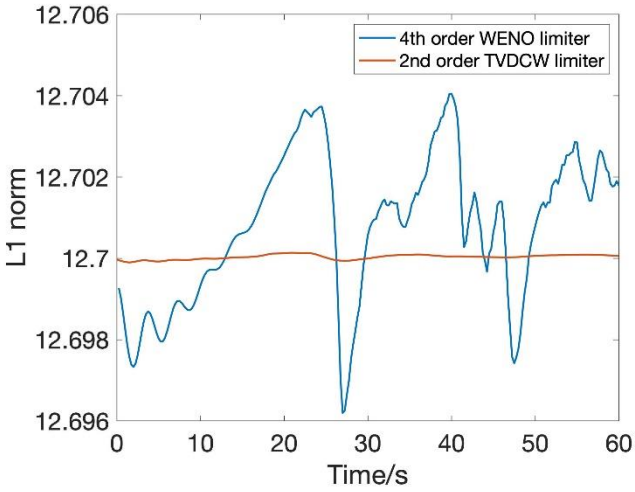

L_1 norm of distribution function f

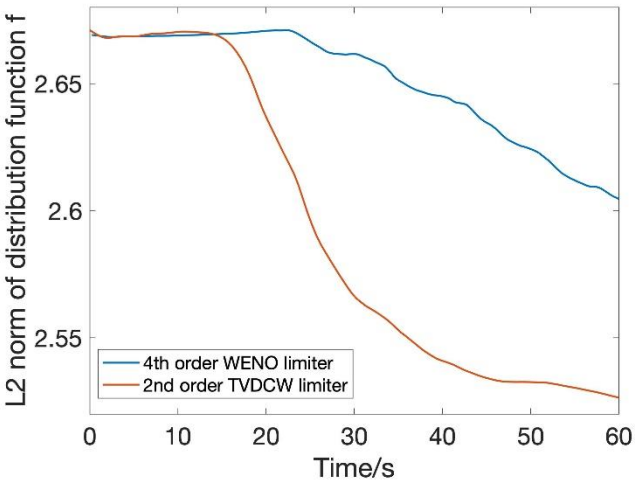

L_2 norm of distribution function f

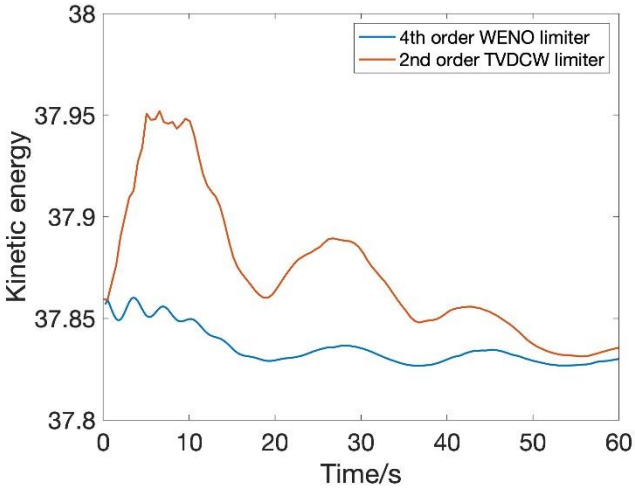

Kinetic energy

Figure 3.25 Two stream instability, physical quantities of L_1 norms (top) and L_2 norms (middle) for the distribution functions and kinetic energy (bottom).

Table 3.4 Order of spatial accuracy in x direction, reference results calculated by $N_x * N_v = 800 * 800$, CFL=0.1, $t = 0.5$ s.

$N_x * N_v$	4th order WENO		2nd order TVDCW	
	L_2 error	order	L_2 error	order
50*800	5.27E-04		2.05E-03	
100*800	3.50E-05	3.91E+00	4.91E-04	2.06E+00
200*800	2.09E-06	4.07E+00	1.07E-04	2.20E+00
400*800	1.28E-07	4.03E+00	2.52E-05	2.08E+00

Table 3.5 Order of spatial accuracy in v direction, reference results calculated by $N_x * N_v = 800 * 800$, CFL=0.1, $t = 0.5$ s.

$N_x * N_v$	4th order WENO		2nd order TVDCW	
	L_2 error	order	L_2 error	order
800*50	9.08E-04		9.11E-03	
800*100	7.72E-05	3.56E+00	2.97E-03	1.62E+00
800*200	5.31E-06	3.86E+00	7.54E-04	1.98E+00
800*400	3.37E-07	3.98E+00	1.75E-04	2.11E+00

Case 3.9 Comparison between fourth-order CIPCSL3 method and full PIC method[38]

In this case, the numerical results of fourth-order WENO scheme is compared with the full PIC method. Both simulations employ 100 grids in space. The PIC method calculates with 100 macroparticles per cell in corresponding to 100 grids in velocity space of Vlasov equation solver.

Recalling the same calculation condition in *Case 3.8,* Figure 3.26 shows the 3D contour plots of both solvers at $t = 30$s.The PIC solver shows lots of statistical noises due to the finite number of macroparticles, meanwhile the Vlasov equation solver generates a smooth result. Figure 3.27 shows the cross-section at $x = 2\pi$, the PIC solver generates overshooting at the peak of the waveform, and it lost the characteristic of symmetry near $v = 0$ m/s, where the number density is low.

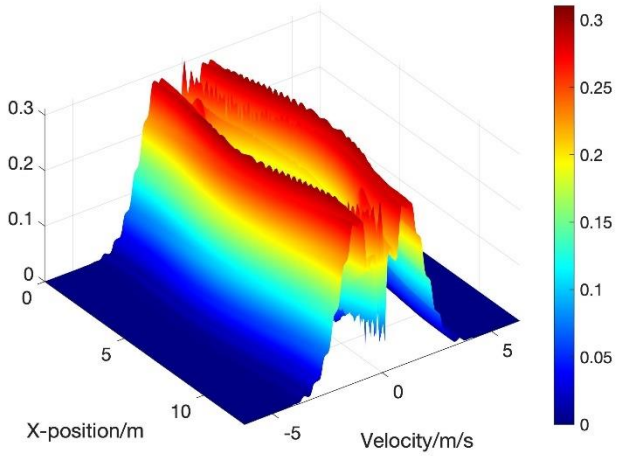

a) Fourth-order Vlasov equation solver

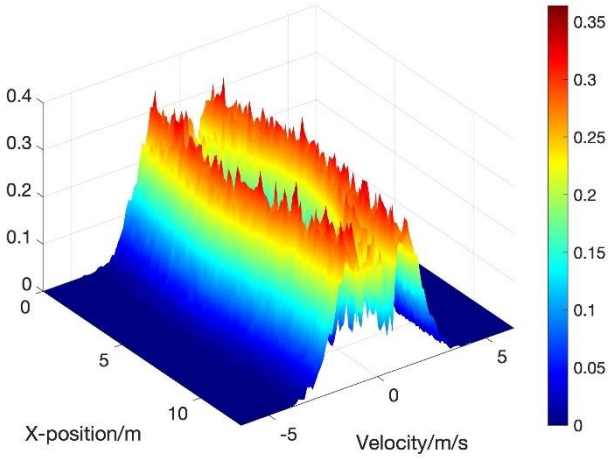

b) Fully PIC solver

Figure 3.26 3D contour plots of two stream instability at $t = 30\,\mathrm{s}$, Vlasov equation solver: $N_x * N_v = 100 * 100, CFL = 0.1$, PIC solver: $N_x = 100$, 100 macroparticles per cell.

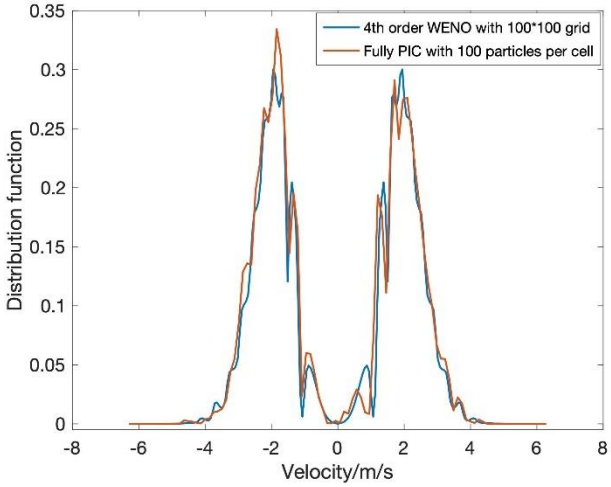

Figure 3.27 Cross-section at $x = 2\pi$.

3.6 Summary of this chapter

In this chapter, several cases have been tested for the code verification. The important findings are:

1. All schemes achieve the design order of accuracy for one-dimensional and two-dimensional test problems with analytical solution, and the fourth-order WENO scheme shows the fastest convergence speed among the schemes tested in this chapter.

2. Fourth-order WENO scheme shows high resolution in the region near sharp density gradient and discontinuities without generating unexpected numerical oscillations.

3. The Vlasov equation solver is successfully developed by using CIPCSL3 method with fourth-order WENO limiter, the last subsection shows the applicability of VP system by solving the Landau damping and two stream instability problems. In the weak linear Landau damping case, both of fourth order WENO limiter and second-order TVDCW limiter predict the damping rate correctly, and in the strong nonlinear Landau damping case, the fourth-order WENO scheme predicts the damping and growth mode correctly, the results are compared with other literatures. On the other hand, the low order scheme fails to capture the growth mode. In the two stream instability case, the design spatial accuracies of the schemes are confirmed.

4. The fourth-order CIPCSL3 Vlasov equation solver generates a noiseless result compares with the PIC solver, it also shows a high-resolution feature to capture the symmetric profile in low-density region, on the other hand, the PIC solver fails to solve the symmetric profile.

Chapter 4 The one-dimensional hybrid ion-Vlasov and electron-fluid model of Hall thruster simulation

In this chapter, the one-dimensional hybrid Vlasov-fluid solver is applied to the HTs discharge current oscillation simulation, and the results are compared with hybrid PIC solver.

4.1 Governing equations of heavy species

The ionization procedure exists during the operation of the HTs, this procedure can be described by adding the source term to the right-hand side of the Vlasov equation, here for ions, the governing equation reads:

$$\frac{\partial f_i}{\partial t} + v_{\mathrm{x,i}} \frac{\partial f_{\mathrm{i}}}{\partial x} + \frac{e}{m_{\mathrm{i}}} E(x,t) \frac{\partial f_{\mathrm{i}}}{\partial v_{\mathrm{x}}} = S_{\mathrm{ion}}, \tag{4.1}$$

and the Vlasov equation for neutral particles is written as:

$$\frac{\partial f_{\mathrm{n}}}{\partial t} + v_{\mathrm{x,n}} \frac{\partial f_{\mathrm{n}}}{\partial x} = -S_{\mathrm{ion}}, \tag{4.2}$$

where f_i, f_n are the distribution functions, $E(x,t)$ is the electric field, e is the elemental charge, m_{i} is the mass of ions and $v_{\mathrm{x,i}}, v_{\mathrm{x,n}}$ are the velocity in x direction. Subscripts i and n respectively signify the ions and neutral particles. S_{ion} is the ionization source term. The ion and neutral number densities $n_{\mathrm{i}}(x)$ and $n_{\mathrm{n}}(x)$ are computed by integrating the distribution functions in the velocity dimension. In this simulation, the velocity of neutral is set as a constant to guarantee that the anode mass flow rate is kept the same.

The relation of S_{ion} to the electron-neutral collisional ionization is expressed as:

$$\int_{-\infty}^{+\infty} S_{\mathrm{ion}} dv_x = n_{\mathrm{e}} n_{\mathrm{n}} k_{\mathrm{ion}}\,, \tag{4.3}$$

where n_{e} represents the number density of electron and k_{ion} stands for the reaction rate coefficient given as a function of the electron temperature[91]. The distribution of S_{ion} in the v_x direction is assumed to be similar to that of f_{n}. Therefore, Equation (4.3) is simplified as:

$$S_{\mathrm{ion}} = n_{\mathrm{e}} k_{\mathrm{ion}} f_{\mathrm{n}}. \tag{4.4}$$

Because of the finite size of the gird in velocity direction, the source term S_{ion} is simplify as a single value inside one cell without distribution. During the calculation, the first derivative of the source term is not calculated and the PV and VIA are directly added to the ion velocity distribution function.

4.2 Electron fluid model

4.2.1 Governing equations of electron fluid model

The quasi-neutrality of charge is assumed in the electron fluid model[37]. The Debye length of the bulk discharge plasma in HTs is typically 10 μm, which is much smaller than the 10 mm discharge channel length. Consequently, the effects of charge separation are neglected for simulating the bulk plasma. The relation $n_e = n_i$ is used.

The 1D electron fluid model consists of the conservation equations of mass, momentum, and energy. With the quasi-neutrality assumption, the mass conservation is written in the form of the equation of continuity as:

$$\frac{\partial}{\partial x}(n_{\mathrm{e}}u_{\mathrm{e}}) = S_{\mathrm{ion}}, \tag{4.5}$$

where u_{e} represents the electron flow velocity. In the conservation equation of electron momentum, the electron inertia is neglected due to the small mass of single electron. The drift–diffusion equation is derived as:

$$n_{\mathrm{e}}\mu_{\perp}\frac{\partial \phi}{\partial x} - D_{\perp}\frac{\partial}{\partial x}(n_{\mathrm{e}}) = n_{\mathrm{e}}u_{\mathrm{e}}, \tag{4.6}$$

where $\mu_{\perp}$ and $D_{\perp}$ represents the electron mobility and electron diffusion coefficient perpendicular to the magnetic lines. The model for the cross-field electron mobility is explained later in this section. By substituting Equation (4.6) into Equation (4.5), an elliptic equation (diffusion equation) is obtained as:

$$\frac{\partial}{\partial x}\left(n_{\mathrm{e}}\mu_{\perp}\frac{\partial \phi}{\partial x} - D_{\perp}\frac{\partial}{\partial x}(n_{\mathrm{e}})\right) = S_{\mathrm{ion}}. \tag{4.7}$$

Here, by employing the Einstein relation $D_{\perp} = \mu_{\perp}T_{\mathrm{e}}$, Equation (4.7) can be expressed as:

$$\frac{\partial}{\partial x}\left(n_{\mathrm{e}}\mu_{\perp}\frac{\partial \phi}{\partial x} - \mu_{\perp}\frac{\partial}{\partial x}(n_{\mathrm{e}}T_{\mathrm{e}})\right) = S_{\mathrm{ion}}. \tag{4.8}$$

In the energy conservation equation, the kinetic component is ignored. The equation is written in terms of the electron internal energy as:

$$\frac{\partial}{\partial t}\left(\frac{3}{2}n_{\mathrm{e}}T_{\mathrm{e}}\right) + \frac{\partial}{\partial x}\left(\frac{5}{2}n_{\mathrm{e}}T_{\mathrm{e}}u_{\mathrm{e}} - \kappa\frac{\partial T_{\mathrm{e}}}{\partial x}\right) = n_{\mathrm{e}}u_{\mathrm{e}}\frac{\partial \phi}{\partial x} - \alpha_{\mathrm{E}}\varepsilon_{\mathrm{ion}}S_{\mathrm{ion}}, \tag{4.9}$$

the second and third terms on the left-hand side respectively denote the enthalpy convection and heat conduction. The first and second terms of the right-hand side are the Joule heating and energy losses by inelastic collisions. The coefficient α_{E} is a function of electron temperature determined for xenon, which is used conveniently to include energy losses by ionization, excitation, and radiation [91]. Also, $\varepsilon_{\mathrm{ion}}$ represents the ionization potential of xenon.

The thermal conductivity and thermal diffusivity hold a relation as:

$$\kappa = \frac{5}{2} n_{\mathrm{e}} D_{\mathrm{t}}, \tag{4.10}$$

where D_{t} is the thermal diffusivity, and in the electron energy conservation, the thermal diffusivity can be treated as:

$$D_{\mathrm{t}} \approx D_{\mathrm{e}}, \tag{4.11}$$

where D_{e} is the electron diffusion coefficient. By applying the Einstein relation $D_{\mathrm{e}} = T_{\mathrm{e}}\mu$, the thermal conductivity can be expressed as:

$$\kappa = \frac{5}{2} n_{\mathrm{e}} D_{\mathrm{t}} = \frac{5}{2} n_{\mathrm{e}} T_{\mathrm{e}} \mu, \tag{4.12}$$

in axial one-dimensional case, $\kappa = \frac{5}{2} n_{\mathrm{e}} T_{\mathrm{e}} \mu_{\perp}$.

The cross-field electron mobility is modelled using a combination of classical diffusion and anomalous components as:

$$\mu_{\perp} = \mu_{\perp,\mathrm{cla}} + \mu_{\perp,\mathrm{ano}}, \tag{4.13}$$

where $\mu_{\perp,\mathrm{cla}}$ and $\mu_{\perp,\mathrm{ano}}$ respectively denote the classical and anomalous electron mobilities. The classical electron mobility is written as:

$$\mu_{\perp,\mathrm{cla}} = \frac{\mu_{\mathrm{e}}}{1 + (\mu_{\mathrm{e}} B)^2}, \tag{4.14}$$

where μ_{e} stands for the mobility of non-magnetized electrons as $\mu_{\mathrm{e}} = e/m_{\mathrm{e}} \nu_{\mathrm{ela}}$ and B is the magnetic flux density. The anomalous electron mobility is modelled by a Bohm-type diffusion model as:

$$\mu_{\perp,\mathrm{ano}} = \frac{\alpha_{\mathrm{B}}}{16B}, \tag{4.15}$$

where α_{B} is designated as the Bohm diffusion coefficient.

The Bohm diffusion coefficient α_{B} is given empirically as a function of the axial

position. Several models have been proposed for the distribution of α_B [92][93]. For this study, the three-region model[94] is adopted, where α_B= 0.14 near the anode, α_B= 0.02 around the channel exit, and α_B= 0.7 in the plume region. These values are interpolated using the Gaussian functions[38] to obtain a smooth axial distribution of α_B.

4.2.2 Numerical method for electron fluid model[37]

The space potential ϕ and electron temperature T_e are obtained through the electron fluid model. The diffusion equation in Equation (4.8) is solved for ϕ. The diffusion terms for ϕ and pressure are discretized using central differencing. A direct matrix-inversion method is used to obtain the ϕ distribution from the discretized equation set. The energy conservation equation in Equation (4.9) is used to derive T_e. The convection term of enthalpy flow is discretized using a second-order upwind method. A minmod-type flux limiter is used to gain the stability of the calculation. The diffusion term of heat conduction is discretized by second-order central differencing. The second-order differencing methods are used in the electron fluid model because the distributions of the plasma parameters such as n_e, T_e, and ϕ, are smooth in the x- (axial-) direction in HTs. Equation (4.9) is treated as a time-dependent equation. Time integration is implemented using a fully implicit method.

Equations (4.8, 4.9) are calculated iteratively to obtain ϕ and T_e. The time step for the electron fluid is set to one-tenth of the time step for ions and neutral particles, *i.e.* ten electron sub-loops are used in a single time step for heavy particles. The electron mobility is calculated only in the first electron sub-loop. The computational grid in the 1D space for the electron fluid is the same as that for the Vlasov equation solver for ions and neutral particles.

4.3 Flowchart of hybrid Vlasov-fluid solver

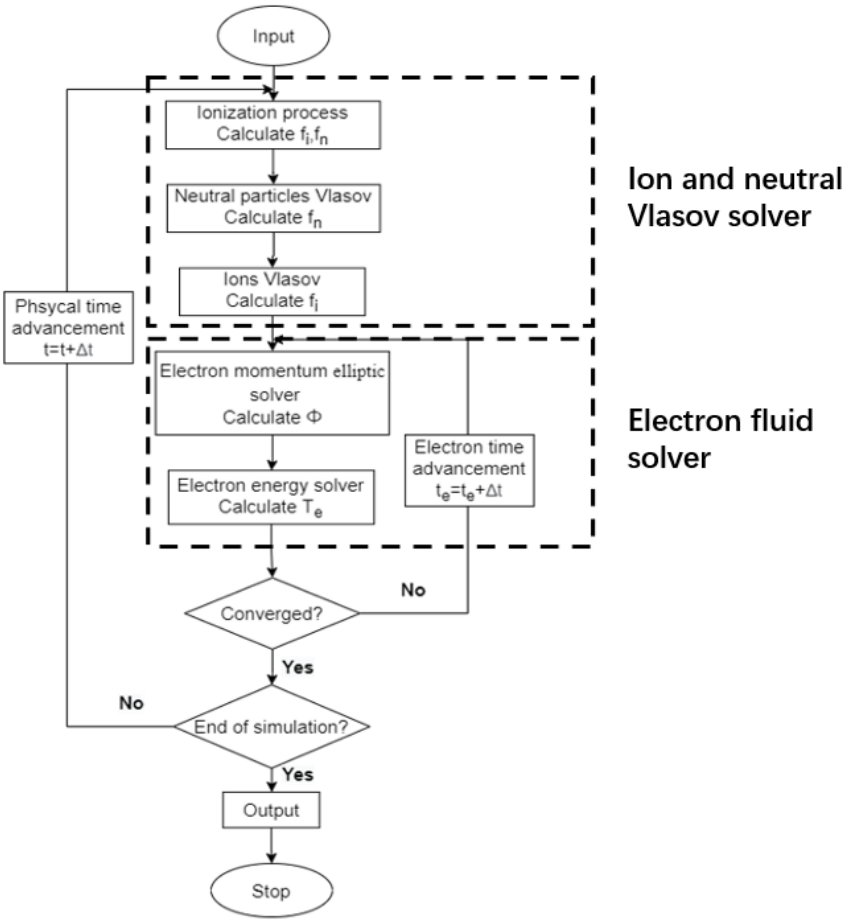

Figure 4.1 Flowchart of the hybrid Vlasov-fluid solver for HTs simulation.

The calculation process of the hybrid Vlasov-fluid solver is demonstrated in Figure 4.1, the calculation domain and initial distribution function are assumed as the input process.

In the beginning, new ions are generated through the ionization process and added to the ion distribution function. The same number of particles are eliminated in the neutral distribution function. Then, ions and neutrals are advected by the Vlasov equation solver for half physical time step in space. Notice that neutral particles only have a single velocity, it doesn't propagate in the velocity space.

Then the ion and neutral number densities are generated by integrating ion and

neutral's distribution function. These parameters are transferred into the electron fluid solver to calculate space potential ϕ and electron temperature T_e iteratively. Once ϕ is updated, the electric field is updated.

Finally, the ions and neutrals are propagated for a fully physical time step in v direction and another half physical time step in x direction.

4.4 1D1V simulation of ionization oscillation in Hall thruster

4.4.1 Calculation conditions

The fourth-order Vlasov equation solver is coupled with the magnetized electron fluid model for HTs simulation. The simulation target is the TAL type HTs developed at The University of Tokyo[95]. An axial 1D1V simulation is performed. The thruster operation parameters assumed for the simulation are presented in Table 4.1. An axial distribution of magnetic flux density is assumed based on the measured data. The schematic of the Hall thruster calculation domain and the magnetic field distribution are portrayed in Figure 4.2. The calculation domain contains the anode, discharge channel, and plume regions. The left-hand and right-hand side boundaries respectively correspond to the anode and cathode. After the propellant gas of xenon is injected into the domain from the left-hand side, it is ionized in the domain, and ejected from the right-hand side boundary.

In the grid-based Vlasov equation solver, the minimum and maximum velocities are set respectively to -5 km/s and 18 km/s. To resolve the distribution function correctly, the velocity space must be discretized finely enough where $\Delta v < 250$ m/s [41]. In this simulation, 192 grids are used in the velocity domain; 48 grids are used in the space

domain, which are corresponding to $\Delta x = 0.2$ mm and $\Delta v = 120$ m/s. The time step is set to 1 ns to satisfy the CFL condition for the Vlasov equation solver. With this time step, the CFL numbers are calculated as $\frac{v_{\mathrm{xmax}}\Delta t}{\Delta x} = 0.04$ and $\frac{eE_{\mathrm{xmax}}}{m_{\mathrm{i}}}\frac{\Delta t}{\Delta v_{\mathrm{x}}} = 0.06$ .The simulation results are output every 1000 time steps, which is equal to 1000 ns. The simulation stops at 1ms, and the total time steps are 10^6.

Table 4.1 Simulation parameters for thruster operation assumed in the simulation.

Operation parameters	Values
Mass flow rate	3.35 mg/s
Propellant gas	xenon
Discharge voltage	250 V
Channel cross-sectional area	2035 mm^2
Channel length	12 mm
Inlet gas temperature	650 K

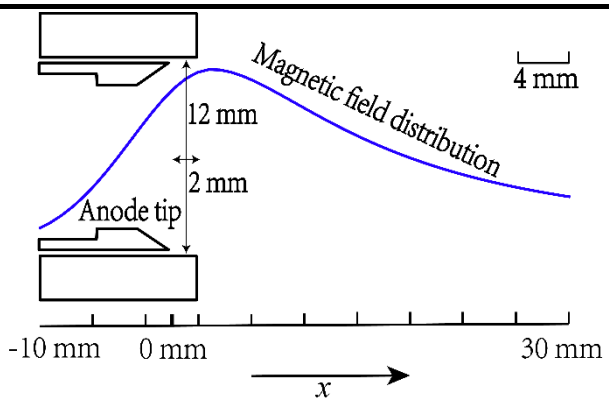

Figure 4.2 Schematic of Hall thruster calculation domain and magnetic field distribution.

4.4.2 Comparison of computed results by hybrid Vlasov-fluid solver and hybrid PIC solver

4.4.2.1 Computational time comparison

The simulations are running on a 2.9 GHz CPU with 32 GB memory, the hybrid Vlasov-fluid solver spends 1.92 hours to finish the 1 ms simulation, meanwhile the hybrid PIC solver which employs 6000 macroparticles per cell takes 4.20 hours. For the Vlasov equation solver, following procedures are required:

1. Calculate ion distribution function with three steps (two steps in space and one step in velocity), since each direction's propagation contains two CIPCSL3 procedures, and third-order Runge-Kutta method is employed, the whole process needs eighteen steps.
2. Calculate neutral distribution function with one step. (two CIPCSL3 procedures)
3. Update new physical valuables.

it represents that the total calculation time for one velocity bin in the Vlasov equation solver is about eleven times more than one macroparticle in the PIC solver. The rate of computational steps can be calculated as:

$$\frac{6000\ \text{macroparticles per cell}\ *\ 2\ \text{steps(hybrid PIC solver)}}{192\ \text{velocity bins per cell}*\ 22\text{steps(hybrid Vlasov}-\text{fluid solver)}} = 2.8409, \tag{4.16}$$

this value shows a good agreement with the total calculation time rate: $4.2/1.92 = 2.1875$.

4.4.2.2 Convergence speed of discharge amplitude

The oscillation amplitude Δ of discharge current is used as a criterion for the ionization oscillation analyses. It can be estimated as:

$$\Delta = \frac{1}{\overline{I_{\mathrm{d}}}}\left[\frac{1}{N}\sum_{i=1}^{N}(I_{\mathrm{d,i}} - \overline{I_{\mathrm{d}}})^2\right]^{0.5}, \quad (4.17)$$

where $\overline{I_d}$ represents the time-averaged discharge current, $I_{\mathrm{d,i}}$ stands for the time varying discharge current, and *N* denotes the number of samples.

Figure 4.3 and Figure 4.4 present the discharge current oscillations and oscillation amplitude over time for the case with classical diffusion coefficient in which $B_{\mathrm{r,max}} = 16$ mT. Here, anomalous electron diffusion coefficient is not used. The calculation grids for the hybrid Vlasov-fluid solver are 48 grids in space and 192 grids in velocity. The hybrid PIC solver is calculated on the domain of 48 grids, and the number of macroparticles in each cell is about 6000, which is the minimum macroparticle number for a converged calculation.

The Vlasov solver achieved a quasi-steady state oscillation mode with constant oscillation amplitude in a very short time. However, in results obtained from a hybrid PIC simulation, the oscillation amplitude is not stable because of the static noise. It is difficult to judge if the simulation reaches a quasi-steady state of coherent waveforms. This unstable oscillation amplitude continues for a long time even if the simulation is performed as exceeding 1 ms. The Vlasov solver generated a steady oscillation waveform within the 1 ms simulation.

The convergence speed of the steady oscillation amplitude is presented in Table 4.2. In addition to the slow convergence speed, the computational cost (CPU seconds) for a given period of simulation is large when using the hybrid PIC method. This high cost is attributable to the large macroparticle number being employed for the simulation. In fact,

the number of macroparticles in the simulation domain is less than 100 during low I_d, although the average macroparticle number is approximately 6000. During low I_d, most of the ions are exhausted. Neutral particles are depleted. Consequently, the number of particles in the hybrid PIC method cannot be decreased. The computational cost becomes large.

Table 4.2 Vlasov solver and hybrid PIC solver convergence speeds.

Solvers	Grids and particles	CPUs for 1 μs calculation	Convergence time
Hybrid Vlasov	48 × 192 grids	6.92 s	0.25 ms
Hybrid PIC	48 grids in space and 6000 particles in 1 cell	15.1 s	More than 1 ms

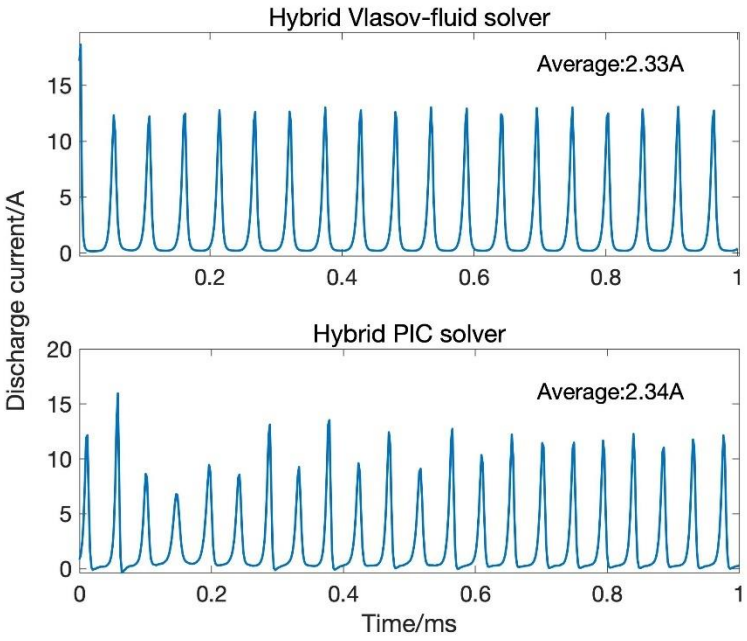

Figure 4.3 Time history of discharge current oscillations with classical diffusion coefficient, the maximum magnetic flux density $B_{\mathrm{r,max}} = 16$ mT.

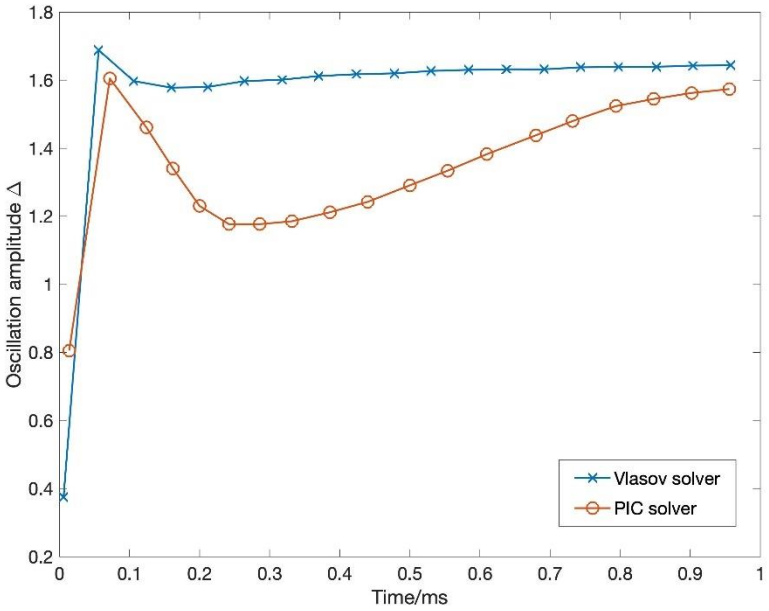

Figure 4.4 Time history of oscillation amplitude with classical diffusion coefficient, the maximum magnetic flux density $B_{\mathrm{r,max}} = 16$ mT.

4.4.2.3 Thruster performance

The specific impulse I_{sp} and thruster efficiency η_t can be estimated through:

$$I_{sp} = \frac{T}{\dot{m}g} \tag{4.18}$$

$$\eta_t = \frac{T^2}{2\dot{m}V_d\bar{I}_d} \tag{4.19}$$

where T represents the thrust, $\dot{m}$ is the anode mass flow rate, V_d stands for the discharge voltage, $\bar{I}_d$ demonstrates the mean discharge current and g is the acceleration of gravity.

Table 4.3 shows the numerical results of thruster performance. The hybrid Vlasov-fluid solver provides an acceptable result compared with hybrid PIC solver. The differences in thrust is due to the numerical diffusion generates during the simulation. Some ions are diffused to the low velocity bins at the exit of the domain.

Table 4.3 Numerical results of thruster performance.

	Hybrid Vlasov-fluid solver	Hybrid PIC solver
Thrust, T	48.1 mN	51.7 mN
Specific impulse, I_{sp}	1465 s	1574 s
Efficiency, η_t	59.28%	63.41%

4.4.2.4 Time-averaged plasma properties

Figure 4.5 presents the time-averaged plasma properties of both solvers, the calculation conditions are the same as above. The plasma properties generated by the hybrid Vlasov-fluid solver (circle marker) show a similar trend as the hybrid PIC solver (star marker).

The space potential distribution shows a good agreement between the two solvers, which guaranteed the similar mean velocities in each cell, these parameters may affect the total performance of HTs. The hybrid Vlasov-fluid solver also calculates the

accelerate region correctly in comparison with the hybrid PIC solver.

For the ion and neutral density distribution, both solvers successfully predict the peak of density near the channel exit, the hybrid Vlasov-fluid solver shows a slightly shift (in the scale of one cell) which may due to the ionization process in Vlasov equation solver. During the simulation, the newly generated ions are accelerated at the beginning of each time loop, lead to the increase of the fast particles, and decrease of the slow particles, this process leads to the shift of maximum value in the ion number distribution.

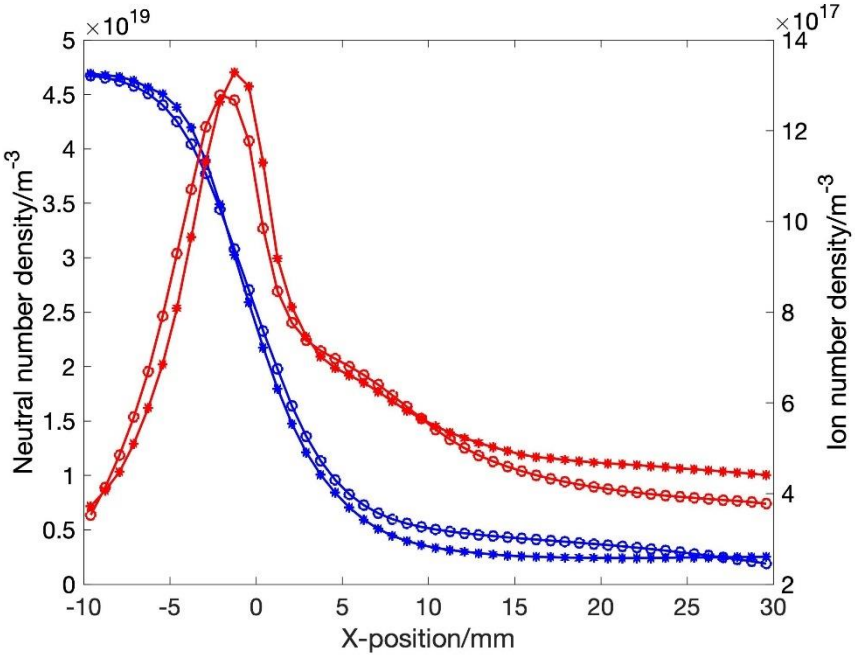

Distributions of neutral (left axis, blue lines) and ion (right axis, red lines) number densities, circle: hybrid Vlasov-fluid solver, star: hybrid PIC solver.

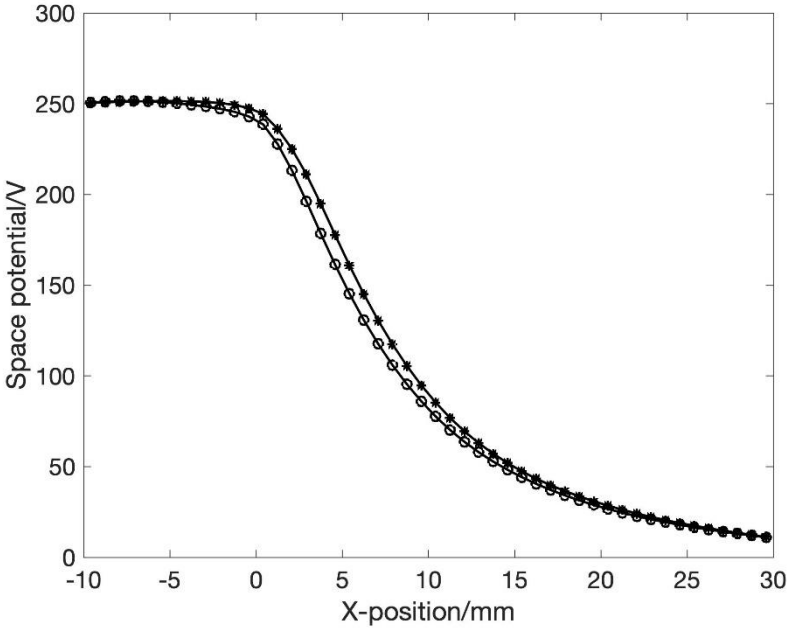

Potential distribution, circle: hybrid Vlasov-fluid solver, star: hybrid PIC solver.

Figure 4.5 Time-averaged distributions of ion and neutral densities (top) and space potential (bottom), calculated with classical diffusion coefficient, $B_{\mathrm{r,max}} = 16\ \mathrm{mT}$. Circle: hybrid Vlasov-fluid solver, Star: hybrid PIC solver.

4.4.2.5 Ion number distribution in single oscillation cycle

Figure 4.6 demonstrates the axial ion number density distribution along with time over the course of a single wave. The hybrid PIC solver generates temporal non-smoothness due to the statistical noise, on the other hand the hybrid Vlasov-fluid solver achieves a noiseless result.

However, the hybrid Vlasov-fluid solver shows a duller spatial distribution than the hybrid PIC solver due to the numerical diffusion caused by the grid value interpolation. In conclusion, from the numerical diffusion view point, the hybrid Vlasov-fluid solver shows more diffusion than the hybrid PIC method.

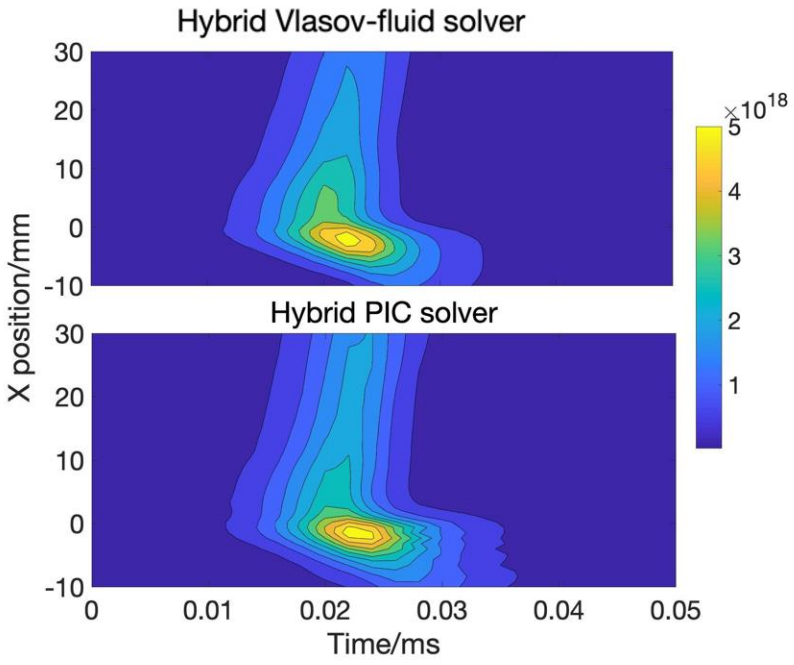

Figure 4.6 Axial ion number density distribution along with time, over the course of a single wave. Top: hybrid Vlasov-fluid solver, bottom: hybrid PIC solver.

4.4.2.6 Oscillation amplitude analyses

Figure 4.7 presents discharge oscillation amplitude changes with different peak magnetic flux densities. Both the hybrid Vlasov-fluid solver and hybrid PIC solver show a trend that is similar to that observed in the experiment [96], although the PIC solver simulation collapsed when the maximum magnetic flux density was less than 15 mT in the classical diffusion case and 12 mT in the Bohm diffusion case which is because, when hybrid PIC solver runs in the low magnetic flux density region, the neutral number density becomes extremely small at the peak discharge current timing in the very first calculation timesteps, resulting in a divergence of the electron fluid solver. In this case, the hybrid PIC solver is unable to generate reasonable results with this number of macroparticles. By contrast, the hybrid Vlasov-fluid solver shows stable reproducibility in a wide magnetic flux density range, even with a less computational cost. Figure 4.8 gives the time history of ion number density near the channel exit at $x = 0.2\ mm$ with classical diffusion coefficient, the dash line demonstrates the ion number density oscillation range, the hybrid Vlasov-fluid solver successfully reproduce the plasma properties in a widely range and the applicability of hybrid Vlasov-fluid solver to solve the high dynamic density variation case (in the order of $O(10^3)$ for ions) is confirmed.

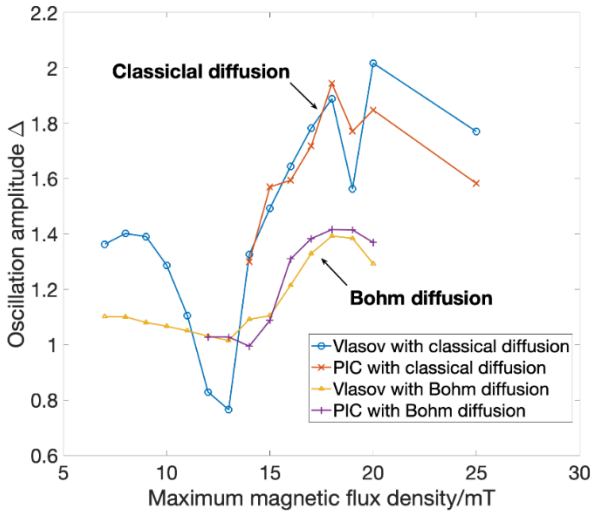

Figure 4.7 Simulation results of discharge oscillation amplitude.

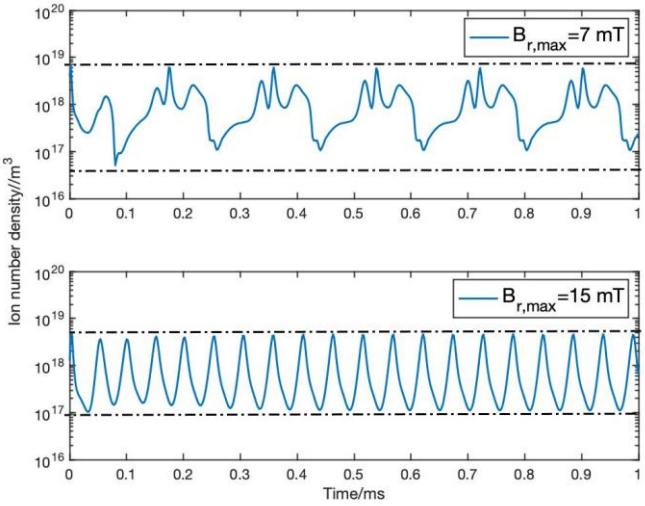

Figure 4.8 Time history of and ion number density with different maximum magnetic flux density with classical diffusion coefficient at $x = 0.2\,mm$, generated by the hybrid Vlasov fluid solver.

4.5 Summary of this chapter

This chapter demonstrates the development of 1D1V hybrid high-order Vlasov-fluid solver which is applied to HTs discharge current oscillation simulation. The simulation results are compared with a hybrid PIC solver, the merits and demerits are as follows:

1. For a single velocity bin calculation in one cell, the hybrid Vlasov-fluid solver shows the computational cost about eleven times higher than a single macroparticle calculation in one cell of the hybrid PIC solver. But owing to the feature of high resolution, the hybrid Vlasov-fluid solver generates the convergence result by employing 192 grids in velocity space per cell, on the other hand, the hybrid PIC solver needs 6000 macroparticles per cell to achieve a reasonable convergence result.

2. For the convergence speed of discharge current amplitude, the hybrid Vlasov-fluid solver shows at least four times faster than the hybrid PIC solver in physical time scale.

3. The thruster performance and time-averaged plasma properties generated by the hybrid Vlasov-fluid solver show a good agreement with hybrid PIC solver's result, the single oscillation cycle analyses demonstrate that hybrid Vlasov-fluid solver eliminates the statistical noise successfully, but numerical diffusion occurs during the calculation.

4. In the single oscillation cycle analyses, the hybrid Vlasov-fluid solver generates the noiseless simulation result. But from the numerical diffusion view point, the hybrid Vlasov-fluid solver shows more diffusion than the hybrid PIC method.

5. In the discharge current amplitude analyses, the hybrid Vlasov-fluid solver shows a widely calculation range along with different maximum magnetic flux density. The results predict the minimum oscillation amplitude occurs with classical diffusion coefficient near B_(r,max)=13 mT, and the trends of oscillation amplitude are the same as hybrid PIC solver obtained.

Chapter 5 Conclusions

5.1 Summary of the work

The originality of this dissertation is to develop a high-resolution noiseless Vlasov equation solver which is free of statistical noise and has the applicability to high dynamic density variation, which may replace the PIC solver of ions and neutrals in hybrid simulation. The CIPCSL3 method with a fourth-order WENO limiter is employed for the development of the Vlasov equation solver.

The fourth-order CIPCSL3 method shows the fast convergence feature compared with the second-order method, and it captures the sharp density gradient and discontinuities correctly without generating unexpected numerical oscillation. In the test case of weak linear Landau damping, both fourth-order and second-order Vlasov equation solver reproduces the damping rate. In the strong nonlinear Landau damping, only fourth-order Vlasov equation solver successfully generates the damping rate and growth rate, and the second-order Vlasov equation solver fails to capture the growth rate. The fourth-order solver's fast convergence and high-resolution feature are confirmed in the two stream instability case compared with the second-order one. In comparison with the PIC solver, the fourth-order Vlasov equation solver achieves a noiseless and high-resolution result.

Finally, the fourth-order Vlasov equation solver is successfully combined with the electron fluid model to reproduce the discharge current oscillations in HTs. The main findings can be summarized as:

1. the hybrid Vlasov-fluid solver generates the convergence result by employing 192 grids in velocity space per cell, on the other hand, the hybrid PIC solver needs 6000 macroparticles per cell to achieve a reasonable convergence result.

2. The hybrid Vlasov-fluid solver shows at least four times faster convergence speed than the hybrid PIC solver in physical time scale.

3. The thruster performance and time-averaged plasma properties generated by the hybrid Vlasov-fluid solver show a good agreement with hybrid PIC solver's result, the single oscillation cycle analyses demonstrate that hybrid Vlasov-fluid solver eliminates the statistical noise successfully, but numerical diffusion occurs during the calculation.

4. In the single oscillation cycle analyses, the hybrid Vlasov-fluid solver generates the noiseless simulation result. But from the numerical diffusion view point, the hybrid Vlasov-fluid solver shows more diffusion than the hybrid PIC method.

5. In the discharge current amplitude analyses, the hybrid Vlasov-fluid solver shows a widely calculation range along with different maximum magnetic flux density. The results predict the minimum oscillation amplitude occurs with classical diffusion coefficient near $B_{\mathrm{r,max}} = 13\ \mathrm{mT}$, and the trends of oscillation amplitude are the same as hybrid PIC solver obtained.

In conclusion, the fourth-order CIPCSL3 method is successfully applied to the hybrid Vlasov-fluid solver to solve the HTs discharge current oscillation in 1D1V. The hybrid high-order Vlasov-fluid solver shows a faster convergence speed in physical time scale and wider calculation range in discharge current amplitude analyses compared with hybrid PIC solver.

5.2 Future work of this study

5.2.1 Extend to multi-dimension

Since the CIPCSL3 method needs to propagate all the integral valuables together with the point value, the computational cost for multi-dimension simulation will become extremely large. Xiao[97] presented an alternative way to calculate the high-dimensional averaged integral valuable by employing a time-evolution converting (TEC) formula. The same assumption can be applied to the Vlasov solver, it will decrease the degree of freedom in CIPCSL3 method significantly.

5.2.2 Positive preserving

The numerical method being used in this dissertation is not positive preserving, a small undershooting will be generated where the physical valuables are near zero. Several works have been down by Zhang and Shu[98][99] for the typical WENO scheme. The idea is to add a linear scaling limiter to the origin scheme. Since the CIPCSL3 method is a compact scheme, it needs to investigate whether the limiter needs to be applied to the conservative relation only or both the first derivative and conservative relation.

Appendix

Cost estimation in higher dimension computation

With the same spatial grid number, the ratio of grid elements propagation per time step of the Vlasov equation solver over the number of PIC solver can be estimate through[100]:

$$\frac{Vlasov}{PIC} = \frac{N_v^{D_v}}{n_m \lambda_D^D}, \tag{A.1}$$

where $N_v^{D_v}$ is the total number of girds in velocity space, $D_v = 1, 2, 3$ is the dimension in velocity space, n_m is the density of macroparticles and λ_D^D is the Debye length, here $n_m \lambda_D^D$ stands for the number of macroparticles per cell. With the increase of the dimension in velocity space, the computational cost of Vlasov equation solver growth exponentially and the cost of PIC solver shows a linear growth rate. Because of this feature, the Vlasov equation solver claims a large storage and computational cost in the high dimension calculation case.

The CIPCSL3 method employs the integral value to keep the mass conservative during the simulation, the degree of freedom is highly depending on the dimensions. For the 1D1V simulation, the point values (PV), surface integrated averaged (SIA) values and volume integrated averaged (VIA) values are claimed to keep the conservation. The values need to update through the CIPCSL1D procedure in one direction:

$$\begin{matrix} \mathrm{CIPCSL1D(PV, SIA)} \\ \mathrm{CIPCSL1D(SIA, VIA)'} \end{matrix} \tag{A.2}$$

which stand for four CIPCSL1D calculation procedures within one time loop in 1D1V calculation. If the simulation extends to 2D2V, the body integrated averaged (BIA) values and quadruple integrated averaged (QIA) values also need to be updated, it will claim four CICPSL1D procedures in one direction, and the total number of calculation procedures in 2D2V is sixteen and in 3D3V is thirty-six respectively. As shown in equation (A.1), for a fair comparison in 2D2V case of Vlasov equation solver and PIC

solver, if $\frac{Vlasov}{PIC} = 1$, following the computational time comparison in 4.4.2.1, the computational time of fourth-order Vlasov equation solver will be approximate 76 times higher than the PIC solver.

The high-order Vlasov equation solver is suitable for the simulation in low dimension (1D1V or 1D2V), with the dimension increased, the degree of freedom and number of grids in velocity space will be increased significantly, which claims a large computational cost than the PIC solver. The high order time-evolution converting (TEC) formula[97] needs to be applied to the CIPCSL3 method to reduce the degree of freedom.

Bibliography

[1] Karniadakis, G., Beskok, A., & Aluru, N. (2006). Microflows and nanoflows: fundamentals and simulation (Vol. 29). Springer Science & Business Media.

[2] Morozov, A. I., & Savelyev, V. V. (2000). Fundamentals of stationary plasma thruster theory. Reviews of plasma physics, 203-391.

[3] Raitses, Y., Smirnov, A., Staack, D., & Fisch, N. J. (2006). Measurements of secondary electron emission effects in the Hall thruster discharge. *Physics of Plasmas*, *13*(1), 014502.

[4] Morozov, A. I., & Savelyev, V. V. (2000). Fundamentals of stationary plasma thruster theory. Reviews of plasma physics, 203-391.

[5] Hamada, Y., Kawashima, R., Komurasaki, K., Yamamoto, N., Tahara, H., & Miyasaka, T. (2017, October). Development Status of 5 kW Class Anode-Layer Type Hall thruster: RAIJIN94. In *the 35th International Electric Propulsion Conference*.

[6] Dwivedi, M., & Malik, H. K. Propagation of Cosh-Gaussian Beam and Its Self-focusing in Plasma under Relativistic Effects. *Smart Energy Resources and*.

[7] Choueiri, E. Y. (2001). Fundamental difference between the two Hall thruster variants. Physics of Plasmas, 8(11), 5025-5033.

[8] Choueiri, E. Y. (2001). Plasma oscillations in Hall thrusters. *Physics of Plasmas*, *8*(4), 1411-1426.

[9] Kusamoto, D., & Komurasaki, K. (1997). Optical diagnosis of plasma in a channel of Hall thrusters. In *International Electric Propulsion Conference* (pp. 405-410).

[10] Yamamoto, N., Yokota, S., Watanabe, K., Sasoh, A., Komurasaki, K., & Arakawa, Y. (2005). Suppression of discharge current oscillations in a Hall thruster. *Transactions of the Japan Society for Aeronautical and Space Sciences*, *48*(161), 169-174.

[11] Ellison, C. L., Raitses, Y., & Fisch, N. J. (2012). Cross-field electron transport induced by a rotating spoke in a cylindrical Hall thruster. *Physics of Plasmas*, *19*(1), 013503.

[12] Bak, J., Kawashima, R., Komurasaki, K., & Koizumi, H. (2019). Plasma formation and cross-field electron transport induced by azimuthal neutral

inhomogeneity in an anode layer Hall thruster. Physics of Plasmas, 26(7), 073505.

[13] Esipchuk, Y. B., Morozov, A. I., Tilinin, G. N., & Trofimov, A. V. (1974). Plasma oscillations in closed-drift accelerators with an extended acceleration zone. *Soviet Physics Technical Physics*, *18*, 928.

[14] Tilinin, G. N. (1977). High-frequency plasma waves in a Hall accelerator with an extended acceleration zone. *Soviet Physics Technical Physics*, *22*, 974-978.

[15] Esipchuk, Y. V., & Tilinin, G. N. (1976). Drift instability in a Hall-current plasma accelerator. *Sov. Phys.-Tech. Phys.(Engl. Transl.);(United States)*, *21*(4).

[16] Spektor, R., Diamant, K. D., Beiting, E. J., Raitses, Y., & Fisch, N. J. (2010). Laser induced fluorescence measurements of the cylindrical Hall thruster plume. *Physics of Plasmas*, *17*(9), 093502.

[17] Mazouffre, S. (2012). Laser-induced fluorescence diagnostics of the cross-field discharge of Hall thrusters. *Plasma Sources Science and Technology*, *22*(1), 013001.

[18] Barral, S., Makowski, K., Peradzyński, Z., Gascon, N., & Dudeck, M. (2003). Wall material effects in stationary plasma thrusters. II. Near-wall and in-wall conductivity. Physics of Plasmas, 10(10), 4137-4152.

[19] Fife, J. M. (1998). *Hybrid-PIC modeling and electrostatic probe survey of Hall thrusters* (Doctoral dissertation, Massachusetts Institute of Technology).

[20] Scharfe, M. K., Thomas, C. A., Scharfe, D. B., Gascon, N., Cappelli, M. A., & Fernandez, E. (2008). Shear-based model for electron transport in hybrid Hall thruster simulations. *IEEE Transactions on Plasma Science*, *36*(5), 2058-2068.

[21] Cappelli, M. A., Young, C. V., Cha, E., & Fernandez, E. (2015). A zero-equation turbulence model for two-dimensional hybrid Hall thruster simulations. *Physics of Plasmas*, *22*(11), 114505.

[22] Lafleur, T., Baalrud, S. D., & Chabert, P. (2016). Theory for the anomalous electron transport in Hall effect thrusters. I. Insights from particle-in-cell simulations. *Physics of Plasmas*, *23*(5), 053502.

[23] Lafleur, T., Baalrud, S. D., & Chabert, P. (2016). Theory for the anomalous electron transport in Hall effect thrusters. II. Kinetic model. *Physics of Plasmas*, *23*(5), 053503.

[24] Lafleur, T., Baalrud, S. D., & Chabert, P. (2017). Characteristics and transport effects of the electron drift instability in Hall-effect thrusters. *Plasma Sources Science and Technology*, *26*(2), 024008.

[25] Boyd, I. D. (2011). Simulation of electric propulsion thrusters. MICHIGAN UNIV ANN ARBOR.

[26] Lee, W., Ethier, S., Jenkins, T. G., Wang, W. X., Lewandowski, J. L. V., Rewoldt, G., ... & Lin, Z. (2006, July). Long time simulations of microturbulence in fusion plasmas. Paper IAEA-CN-138/TH/2-6Rb, Presented at Fusion Energy 2006, Proceedings of the 21st IAEA Conference, Chengdu China.

[27] Holod, I., & Lin, Z. (2007). Statistical analysis of fluctuations and noise-driven transport in particle-in-cell simulations of plasma turbulence. *Physics of plasmas*, *14*(3), 032306.

[28] Lapenta, G. (2002). Particle rezoning for multidimensional kinetic particle-in-cell simulations. *Journal of computational physics*, *181*(1), 317-337.

[29] Teunissen, J., & Ebert, U. (2014). Controlling the weights of simulation particles: adaptive particle management using kd trees. *Journal of Computational Physics*, *259*, 318-330.

[30] Tofighian, H., Amani, E., & Saffar-Avval, M. (2019). Parcel-number-density control algorithms for the efficient simulation of particle-laden two-phase flows. *Journal of Computational Physics*, *387*, 569-588.

[31] Szabo, J. J. (2001). Fully kinetic numerical modeling of a plasma thruster (Doctoral dissertation, Massachusetts Institute of Technology).

[32] Blateau, V., Martinez-Sanchez, M., & Batishchev, O. (2002). A computational study of internal physical effects in a Hall thruster. In *38th AIAA/ASME/SAE/ASEE Joint Propulsion Conference & Exhibit* (p. 4105).

[33] Irishkov, S. V., Gorshkov, O. A., & Shagayda, A. A. (2005). Fully kinetic modeling of low-power hall thrusters. *IEPC paper*, *35*, 2005.

[34] Cho, S., Komurasaki, K., & Arakawa, Y. (2013). Kinetic particle simulation of discharge and wall erosion of a Hall thruster. *Physics of Plasmas*, *20*(6), 063501.

[35] Garrigues, L., Boyd, I. D., & Boeuf, J. P. (2001). Computation of Hall thruster performance. *Journal of Propulsion and Power*, *17*(4), 772-779.

[36] Komurasaki, K., & Arakawa, Y. (1995). Two-dimensional numerical model of plasma flow in a Hall thruster. *Journal of Propulsion and Power*, *11*(6), 1317-1323.

[37] Kawashima, R., Komurasaki, K., & Schönherr, T. (2015). A hyperbolic-equation system approach for magnetized electron fluids in quasi-neutral plasmas. *Journal of Computational Physics*, *284*, 59-69.

[38] Kawashima, R., Hara, K., & Komurasaki, K. (2018). Numerical analysis of azimuthal rotating spokes in a crossed-field discharge plasma. *Plasma Sources Science and Technology*, *27*(3), 035010.

[39] Boeuf, J. P., & Garrigues, L. (1998). Low frequency oscillations in a stationary

plasma thruster. *Journal of Applied Physics*, *84*(7), 3541-3554.

[40] Morozov, A. I., & Savel'ev, V. V. (2000). One-dimensional hybrid model of a stationary plasma thruster. *Plasma Physics Reports*, *26*(10), 875-880.

[41] Hara, K. (2015). Development of Grid-Based Direct Kinetic Method and Hybrid Kinetic-Continuum Modeling of Hall Thruster Discharge Plasmas (Doctoral dissertation).

[42] Van Leer, B. (1977). Towards the ultimate conservative difference scheme. IV. A new approach to numerical convection. *Journal of computational physics*, *23*(3), 276-299.

[43] Mikellides, I. G., Katz, I., Hofer, R. H., & Goebel, D. M. (2009). Hall-effect thruster simulations with 2-D electron transport and hydrodynamic ions.

[44] Mikellides, I., Katz, I., Hofer, R., Goebel, D., de Grys, K., & Mathers, A. (2010, July). Magnetic shielding of the acceleration channel walls in a long-life Hall thruster. In *46th AIAA/ASME/SAE/ASEE Joint Propulsion Conference & Exhibit* (p. 6942).

[45] Giraldo, F. X., & Neta, B. (1999). Stability analysis for Eulerian and semi-Lagrangian finite-element formulation of the advection-diffusion equation. Computers & Mathematics with Applications, 38(2), 97-112.

[46] Courant, R., Isaacson, E., & Rees, M. (1952). On the solution of nonlinear hyperbolic differential equations by finite differences. *Communications on pure and applied mathematics*, *5*(3), 243-255.

[47] Godunov, S. K. (1959). A difference method for numerical calculation of discontinuous solutions of the equations of hydrodynamics. *Matematicheskii Sbornik*, *89*(3), 271-306.

[48] Van Leer, B. (1979). Towards the ultimate conservative difference scheme. V. A second-order sequel to Godunov's method. *Journal of computational Physics*, *32*(1), 101-136.

[49] Wiin-Nielsen, A. (1959). On the application of trajectory methods in numerical forecasting. *Tellus*, *11*(2), 180-196.

[50] Cheng, C. Z., & Knorr, G. (1976). The integration of the Vlasov equation in configuration space. *Journal of Computational Physics*, *22*(3), 330-351.

[51] Sonnendrücker, E., Roche, J., Bertrand, P., & Ghizzo, A. (1999). The semi-Lagrangian method for the numerical resolution of the Vlasov equation. *Journal of computational physics*, *149*(2), 201-220.

[52] Nakamura, T., Yabe, T. (1999). Cubic interpolated propagation scheme for

solving the hyper-dimensional Vlasov-Poisson equation in phase space. *Computer Physics Communications*, *120*(2-3), 122-154.

[53] Qiu, J. M., Christlieb, A. (2010). A conservative high order semi-Lagrangian WENO method for the Vlasov equation. *Journal of Computational Physics*, *229*(4), 1130-1149.

[54] Xiao, F., & Yabe, T. (2001). Completely conservative and oscillationless semi-Lagrangian schemes for advection transportation. *Journal of computational physics*, *170*(2), 498-522.

[55] Qiu, J. M., & Shu, C. W. (2011). Conservative high order semi-Lagrangian finite difference WENO methods for advection in incompressible flow. *Journal of Computational Physics*, *230*(4), 863-889.

[56] Heath, R. E., Gamba, I. M., Morrison, P. J., & Michler, C. (2012). A discontinuous Galerkin method for the Vlasov–Poisson system. *Journal of Computational Physics*, *231*(4), 1140-1174.

[57] Rossmanith, J. A., & Seal, D. C. (2011). A positivity-preserving high-order semi-Lagrangian discontinuous Galerkin scheme for the Vlasov–Poisson equations. *Journal of Computational Physics*, *230*(16), 6203-6232.

[58] Carrillo, J. A., Majorana, A., & Vecil, F. (2007). A semi-Lagrangian deterministic solver for the semiconductor Boltzmann-Poisson system. *Communications in Computational Physics*, *2*(5), 1027-1054.

[59] Bonaventura, L., & Ferretti, R. (2015). Flux form Semi-Lagrangian methods for parabolic problems. *arXiv preprint arXiv:1505.00940*.

[60] Yabe, T., Ishikawa, T., Kadota, Y., & Ikeda, F. (1990). A multidimensional cubic-interpolated pseudoparticle (CIP) method without time splitting technique for hyperbolic equations. *Journal of the Physical Society of Japan*, *59*(7), 2301-2304.

[61] Yabe, T., Aoki, T., Sakaguchi, G., Wang, P. Y., & Ishikawa, T. (1991). The compact CIP (Cubic-Interpolated Pseudo-particle) method as a general hyperbolic solver. *Computers & Fluids*, *19*(3-4), 421-431.

[62] Yabe, T., Xiao, F., & Utsumi, T. (2001). The constrained interpolation profile method for multiphase analysis. *Journal of Computational physics*, *169*(2), 556-593.

[63] Nakamura, T., Tanaka, R., Yabe, T., & Takizawa, K. (2001). Exactly conservative semi-Lagrangian scheme for multi-dimensional hyperbolic equations with directional splitting technique. *Journal of computational physics*, *174*(1), 171-207.

[64] Tanaka, R., Nakamura, T., & Yabe, T. (2000). Constructing exactly conservative scheme in a non-conservative form. *Computer physics communications*, *126*(3),

232-243.

[65] Yabe, T., Tanaka, R., Nakamura, T., & Xiao, F. (2001). An exactly conservative semi-Lagrangian scheme (CIP–CSL) in one dimension. *Monthly Weather Review*, *129*(2), 332-344.

[66] Xiao, F., Ikebata, A., & Hasegawa, T. (2005). Numerical simulations of free-interface fluids by a multi-integrated moment method. *Computers & structures*, *83*(6-7), 409-423.

[67] Ii, S., & Xiao, F. (2010). A global shallow water model using high order multi-moment constrained finite volume method and icosahedral grid. *Journal of Computational physics*, *229*(5), 1774-1796.

[68] Sun, Z., & Xiao, F. (2017). A semi‐Lagrangian multi‐moment finite volume method with fourth‐order WENO projection. *International Journal for Numerical Methods in Fluids*, *83*(4), 351-375.

[69] Lewy, H., Friedrichs, K., & Courant, R. (1928). Über die partiellen Differenzengleichungen der mathematischen Physik. *Mathematische Annalen*, *100*, 32-74.

[70] Jiang, G. S., & Shu, C. W. (1996). Efficient implementation of weighted ENO schemes. *Journal of computational physics*, *126*(1), 202-228.

[71] Borges, R., Carmona, M., Costa, B., & Don, W. S. (2008). An improved weighted essentially non-oscillatory scheme for hyperbolic conservation laws. *Journal of Computational Physics*, *227*(6), 3191-3211.

[72] Henrick, A. K., Aslam, T. D., & Powers, J. M. (2005). Mapped weighted essentially non-oscillatory schemes: achieving optimal order near critical points. *Journal of Computational Physics*, *207*(2), 542-567.

[73] Shen, Y., & Zha, G. (2014). Improvement of weighted essentially non-oscillatory schemes near discontinuities. *Computers & Fluids*, *96*, 1-9.

[74] Colella, P., & Woodward, P. R. (1984). The piecewise parabolic method (PPM) for gas-dynamical simulations. *Journal of computational physics*, *54*(1), 174-201.

[75] Strang, G. (1968). On the construction and comparison of difference schemes. *SIAM journal on numerical analysis*, *5*(3), 506-517.

[76] Leveque, R. J. (1996). High-resolution conservative algorithms for advection in incompressible flow. *SIAM Journal on Numerical Analysis*, *33*(2), 627-665.

[77] Guo, W., & Qiu, J. M. (2013). Hybrid semi-Lagrangian finite element-finite difference methods for the Vlasov equation. Journal of Computational Physics, 234, 108-132.

[78] Van Loan, C. (1992). *Computational frameworks for the fast Fourier transform*. Society for Industrial and Applied Mathematics.

[79] Tan, S., & Shu, C. W. (2010). Inverse Lax-Wendroff procedure for numerical boundary conditions of conservation laws. *Journal of Computational Physics*, *229*(21), 8144-8166.

[80] Morinishi, Y., Lund, T. S., Vasilyev, O. V., & Moin, P. (1998). Fully conservative higher order finite difference schemes for incompressible flow. *Journal of computational physics*, *143*(1), 90-124.

[81] Tan, S., & Shu, C. W. (2011). A high order moving boundary treatment for compressible inviscid flows. *Journal of Computational Physics*, *230*(15), 6023-6036.

[82] Landau, L. D. (1946). On the vibrations of the electronic plasma. *Zh. Eksp. Teor. Fiz.*, *10*, 25.

[83] Tsurutani, B. T., & Lakhina, G. S. (1997). Some basic concepts of wave‐particle interactions in collisionless plasmas. *Reviews of Geophysics*, *35*(4), 491-501.

[84] Fried, B. D., & Conte, S. D. (2015). The plasma dispersion function: the Hilbert transform of the Gaussian. Academic Press.

[85] Mehrenberger, M., Navoret, L., & Pham, N. (2018). Recurrence phenomenon for Vlasov-Poisson simulations on regular finite element mesh.

[86] Abbasi, H., Jenab, M. H., & Pajouh, H. H. (2011). Preventing the recurrence effect in the Vlasov simulation by randomizing phase-point velocities in phase space. *Physical Review E*, *84*(3), 036702.

[87] Nishikawa, H. (2020). A hyperbolic Poisson solver for tetrahedral grids. *Journal of Computational Physics*, *409*, 109358.

[88] Boyd, J. P. (2001). *Chebyshev and Fourier spectral methods*. Courier Corporation.

[89] Fuka, V. (2015). PoisFFT–A free parallel fast Poisson solver. Applied Mathematics and Computation, 267, 356-364.

[90] Sonnendrücker, E. (2015, July). Computational plasma physics. In *Vorlesung/Übung (SS 2015)*.

[91] Goebel D M and Katz I (2008) Fundamentals of electric propulsion: ion and Hall thrusters vol 1 (John Wiley & Sons)

[92] Dugan, J. V., & Sovie, R. J. (1967). Volume ion production costs in tenuous plasmas: a general atom theory and detailed results for helium, argon, and

cesium (Vol. 4150). National Aeronautics and Space Administration.

[93] Hagelaar, G. J. M., Bareilles, J., Garrigues, L., & Boeuf, J. P. (2003). Role of anomalous electron transport in a stationary plasma thruster simulation. Journal of Applied Physics, 93(1), 67-75.

[94] Koo, J. W., & Boyd, I. D. (2006). Modeling of anomalous electron mobility in Hall thrusters. Physics of Plasmas, 13(3), 033501.

[95] Hamada, Y., Bak, J., Kawashima, R., Koizumi, H., Komurasaki, K., Yamamoto, N., ... & Tahara, H. (2017). Hall thruster development for Japanese space propulsion programs. *Transactions of the Japan Society for Aeronautical and Space Sciences*, *60*(5), 320-326.

[96] Yamamoto, N., Komurasaki, K., & Arakawa, Y. (2005). Discharge current oscillation in Hall thrusters. *Journal of propulsion and power*, *21*(5), 870-876.

[97] Xiao, F., Akoh, R., & Ii, S. (2006). Unified formulation for compressible and incompressible flows by using multi-integrated moments II: Multi-dimensional version for compressible and incompressible flows. *Journal of Computational Physics*, *213*(1), 31-56.

[98] Zhang, X., & Shu, C. W. (2010). On maximum-principle-satisfying high order schemes for scalar conservation laws. *Journal of Computational Physics*, *229*(9), 3091-3120.

[99] Zhang, X., & Shu, C. W. (2011). Maximum-principle-satisfying and positivity-preserving high-order schemes for conservation laws: survey and new developments. *Proceedings of the Royal Society A: Mathematical, Physical and Engineering Sciences*, *467*(2134), 2752-2776.

[100] Büchner, J. (2005, March). Vlasov-code simulation. In Proceedings of ISSS (Vol. 7, pp. 26-31).

List of achievements

Journal Publications

1. Zhexu Wang, Rei Kawashima, Kimiya Komurasaki.“A Fast convergence fourth-order Vlasov model for Hall thruster ionization oscillation analyses. ”, *Plasma Science and Technology*, **Under review**

2. Mingxuan, Yang, Zheng Hao, Qi Bojin, Zhexu Wang, and Liu Rainy. “Pulsed arc light monitoring and temperature reconstruction with arc welding.” *Science and Technology of Welding and Joining* (2020): 1-8.

Conference

1. Zhexu Wang, Amareshwara Sainadh Ch., Rei Kawashima, Kimiya Komurasaki, Hiroyuki Koizumi, “A One-dimensional Hybrid Particle-Fluid Simulation with Electron Inertia in a Hall Effect Thruster.” In *9th Asian Joint Conference on Propulsion and Power*, Xiamen, China, 2018.
2. Zhexu Wang, Rei Kawashima, Kimiya Komurasaki, Hiroyuki Koizumi, “Development of noiseless Vlasov solver for ion flow in Hall thruster.” In *The 2nd International Conference on Mechanics 2018(ICM2018)*, Taiwan, China. ICM-113.
3. Zhexu Wang, Rei Kawashima, Kimiya Komurasaki, “The oscillationless semi-Lagrangian type Vlasov solver for ion flow simulation.” In *37th ANSS, Tokyo*, Japan. SBM000101
4. Zhexu Wang, Rei Kawashima, Ito Gen, Yushi Hamada, Kimiya Komurasaki, “The development of Hall thruster in the University of Tokyo (In Chinese).” *In Chinese Electric Propulsion Conference*, Vol2, p 131 138
5. Zhexu Wang, Rei Kawashima, Kimiya Komurasaki, “A hybrid Vlasov-fluid model for the analyses of discharge oscillation in a thruster with anode layer.” In IAPS2020
6. Rei Kawashima, Zhexu Wang, Kimiya Komurasaki, Hiroyuki Koizumi, “ブラソフ–流体ハイブリッドモデルによるホールスラスタのプラズマ振動解析.” In *51st JSASS*, 2B04
7. Chamarthi, Amareshwara Sainadh, Zhexu Wang, Rei Kawashima, and Kimiya Komurasaki. "Weighted nonlinear schemes for magnetized electron fluid in quasi-neutral plasma." In *2018 AIAA Aerospace Sciences Meeting*, p. 2194. 2018.
8. Rei Kawashima, Zhexu Wang, Amareshwara Sainadh Chamarthi, Hiroyuki Koizumi, and Kimiya Komurasaki. "Hyperbolic System Approach for Magnetized Electron Fluids in ExB Discharge Plasmas." In *2018 AIAA Aerospace Sciences Meeting*, p. 0175. 2018.
9. Rei Kawashima, Zhexu Wang, and Kimiya Komurasaki. "Hybrid Vlasov-Fluid

Model with High-Order Schemes for Partially Ionized Plasma Flows." In *AIAA Scitech 2021 Forum*, p. 0553. 2021.